OCS Study
BOEM 2017-055

Final Report

Expansion of West Coast Oceanographic Modeling Capability

US Department of the Interior
Bureau of Ocean Energy Management
Pacific OCS Region

OCS Study
BOEM 2017-055

Expansion of West Coast Oceanographic Modeling Capability

August 2017

Authors:

Changming “Charles” Dong
Lionel Renault
Yongchui Zhang
Jing Ma
Yuhan Cao

Prepared under BOEM Cooperative Agreement
M14AC00021
by
University of California, Los Angeles
405 Hilgard Ave., Los Angeles, CA 90095

US Department of the Interior
Bureau of Ocean Energy Management
Pacific OCS Region

DISCLAIMER

This report was prepared under cooperative agreement between the Bureau of Ocean Energy Management (BOEM) and University of California, Los Angeles. Study concept, oversight, and funding were provided by the U.S. Department of the Interior, Bureau of Ocean Energy Management, Environmental Studies Program, Washington, DC, under Cooperative Agreement Number M14AC00021. This report has been technically reviewed by BOEM and it has been approved for publication. The views and conclusions contained in this document are those of the authors and should not be interpreted as representing the opinions or policies of the U.S. Government, nor does mention of trade names or commercial products constitute endorsement or recommendation for use.

REPORT AVAILABILITY

CITATION

Dong, C., L. Renault, Y. Zhang, J, Ma, and Y. Cao, 2017: Expansion of West Coast Oceanographic Modeling Capability. US Department of the Interior, Bureau of Ocean Energy Management, Pacific. OCS Study BOEM 2017-055. 83 pp.

ACKNOWLEDGMENTS

All authors appreciate Ms. Susan F. Zaleski, the Project Officer, for her great support, hard work, and professional management during the course of the project.

Contents

List of Figures

List of Tables

Abbreviations and Acronyms

ADCP	acoustic Doppler current profiler
AFWA	Air Force Weather Agency
ARW	Advanced Research WRF
BOEM	Bureau of Ocean Energy Management
CalCOFI	California Cooperative Oceanic Fisheries Investigations
CCMP	Cross-Calibrated Multi-Platform
CO-OPS	Center for Operational Oceanographic Products and Services
CORE	Common Ocean Reference Experiment
CU	California Undercurrent
DPD	dominant period
ECMWF	European Centre for Medium-Range Weather Forecasts
EnKF	Ensemble Kalman Filter
EnOI	Ensemble Optimum Interpolation
ESCB	extended Southern California Bight
ESP	Environmental Studies Program
FAA	Federal Aviation Administration
FSL	Forecast Systems Laboratory
GNOME	General National Oceanic and Atmospheric Administration Office of Response and Restoration Oil Modeling Environment
GPCP	Global Precipitation Climatology Project
HF	High frequency
HYCOM	HYbrid Coordinate Ocean Model
IFS	Integrated Forecasting System
IOOS	Integrated Ocean Observing Systems
JPL	Jet Propulsion Laboratory
MWD	Mean wave
NASA	National Aeronautics and Space Administration
NCAR	National Center for Atmospheric Research
NCEP	National Centers for Environmental Prediction
NDBC	National Data Buoy Center
NMM	Nonhydrostatic Mesoscale Model
NOAA	National Oceanic and Atmospheric Administration
OCS	Outer Continental Shelf
PI	Principle investigator
PBL	planetary boundary layer
PSU	practical salinity unit
ROMS	Regional Ocean Modeling System
RRTM	rapid radiative transfer model
SBC	Santa Barbara Channel
SCB	Southern California Bight
SCC	Southern California Countercurrent

SCCOOS	Southern California Coastal Ocean Observing System
SODA	Simple Oceanic Data Assimilation
SSH	sea surface height
SST	sea surface temperature
SWH	Significant wave height
SWAN	Simulating WAves Nearshore
WPS	WRF Preprocessing System
VAM	Variational Analysis Method
WRF	Weather Research and Forecasting

1. Introduction

1.1 Background

Offshore oil and gas in southern California necessitate a significant quantity of petroleum production. Oil spills and the resulting effects on human and marine environments continue to be a major environmental concern with offshore oil and gas activities. The largest oil spill in the Pacific Outer Continental Shelf (OCS) region occurred in 1969 off the coast of Santa Barbara, when a loss of well control occurred on Platform A, which spilled an estimated 80,000 barrels (bbls) into the Channel. The second largest oil spill in the Pacific OCS was the 164 bbl Platform Irene pipeline spill in September 1997. With the development of oil and gas resources, oil spill risk analysis is essential for oil spill planning. The BOEM Pacific OCS Region currently uses two oil spill models to conduct oil spill risk analysis over southern California: the BOEM Oil Spill Risk Analysis (OSRA) and the General National Oceanic and Atmospheric Administration (NOAA) Operational Modeling Environment (GNOME). The hindcast input to the models needs to be updated and expanded to provide more accurate information to conduct offshore oil and gas risk analyses over a wider geographic area. The Integrated Ocean Observing Systems (IOOS), along the West Coast of the U.S., maintain real-time observational data of wind, waves, and currents offshore coastal California. Reanalysis or hindcast of these observational data enables analysts and decision makers to understand the seasonal and annual variation of wind, waves, and currents. Broadening the geographic range of available data and acquiring, compiling, and converting real-time data through numerical modeling into a format to run oil spill models will improve BOEM Pacific OCS Region’s ability to conduct oil spill risk analysis for southern California.

The extended Southern California Bight (ESCB) is influenced by the large-scale California Current offshore, tropical remote forcing through the coastal wave guide alongshore, and local atmospheric forcing. The region is characterized by local complexity in the topography and coastline. All these factors engender variability in the circulation on interannual, seasonal, and intraseasonal time scales. At the sea surface, the broad and slow equatorward California Current carries fresh and cold northern Pacific water toward the Southern California Bight (SCB), turning eastward into the Bight near its southern end. The California Current is accompanied by a poleward Southern California Countercurrent (SCC) near the coast with warmer and saltier water advected from the tropics (Hickey et al., 1979). Beneath the surface (at depths of 100–300 m), the coastal flow is dominated by a poleward California Undercurrent (CU, Hill et al., 1998). Each of the above three components exhibits its own seasonality. In the SCC, poleward flow is found along the coast during all seasons except spring, when the wind near the coast increases and the wind-driven surface current flows equatorward. Both observation data (Strub and James, 2000) and model results (Di Lorenzo, 2003; Marchesiello et al., 2003; Dong et al., 2009, hereafter D09) confirm this phenomenon.

D09 published a 1996–2003 high-resolution oceanic current hindcast product covering the whole SCB, in which sea surface wind variation was also presented. Later the product was further extended to 2007, totaling 12 years of high-resolution hindcast product. The decade-long product is generated using the Regional Ocean Modeling System (ROMS) with a 1 km horizontal resolution and 40 vertical levels.

The model was forced by MM5 (Pennsylvania State University/National Center for Atmospheric Research [NCAR] 5th Generation Mesoscale Model) meteorological fluxes at the sea surface and Simple Oceanic Data Assimilation (SODA) fluxes along the open lateral boundaries. The model product has been intensively validated against all historical observation data, including surface drifter data, acoustic Doppler current profiler (ADCP) velocity vertical profiles, buoy data, the California Cooperative Oceanic Fisheries Investigations (CalCOFI) ship data, High-frequency (HF) radar surface currents, and satellite remote sensing data [sea surface height (SSH) and sea surface temperature (SST)] (Dong et al., 2009; Ohlmann and Mitarai, 2010; Dong et al., 2011). The validation is conducted at different time scales: interannual, seasonal, and intraseasonal scales. The MM5 wind product was also validated against Quick Scatterometer (QuikSCAT) wind, near-shore weather stations, and buoy winds. The product has been extensively applied to studies such as coastal upwelling, oceanic mesoscale and submesoscale eddy dynamics, larval dispersion, drifter Lagrangian trajectory variation.

The purpose of this study is to extend and update the modeling effort in the SCB to a wider geographic region with inclusion of the model developments and modern observational data. The model is further extended to north of Point Conception including Morro Bay. As noted above, the existing high-resolution product was generated for the period of 1996–2007 by the Principal Investigator (PI) and his colleagues at University of California, Los Angeles. The group with which the PI is working keeps improving the accuracy and efficiency of the numerical models. The meteorological model MM5 used has been upgraded to the Weather Research and Forecasting (WRF) model since 2000. More observational data has become available since then. Therefore, with the advance in numerical technology and more observational data, more accurate numerical hindcast products from the existing product can be generated, which will improve the BOEM Pacific OCS Region's ability to conduct oil spill risk analysis in southern California.

1.2 Study objectives

The overall objective of this study is to improve the understanding of multiscale (interannual, seasonal, and intra-seasonal scales) variations of physical processes (wind, current, and wave) in an extended southern California coast.

Specific objectives are as follows:

(1) Extend the existing 12-year (1996–2007) hindcast product in the SCB to a broader geographic region including Morro Bay and north of Point Conception, and to modern 10 years (2004–2013).
(2) Include new developments in numerical models: WRF, ROMS, and Simulating WAves Nearshore (SWAN).
(3) Deliver a 10-year high-resolution hindcast product for OSRA and GNOME to conduct oil spill analysis, including hourly sea surface wind and sea surface currents.

(4) Deliver a 10-year high-resolution hindcast product for 3D particle transport model to conduct other relevant BOEM supported projects.
(5) Deliver a 10-year product to BOEM as archives.
(6) Publish the results of the study as a BOEM OCS Study Report and in peer-reviewed scientific journals.

1.3 Overview of study

Chapter 2 introduces the three new hindcasts of WRF, ROMS, and SWAN.
Chapter 3 summarizes the data management.
Chapter 4 presents the validation of the WRF simulated surface winds and precipitation against observations.
Chapter 5 shows the validation of the ROMS simulated tides, SSH, water temperature, salinity, and currents against observations.
Chapter 6 gives the validation of the SWAN simulated wave data against observations.
Chapter 7 provides a summary of the study.

2. Model Hindcasts

2.1 The WRF hindcast

The WRF Model is a next-generation mesoscale numerical weather prediction system designed for both atmospheric research and operational forecasting needs. It features two dynamical cores, a data assimilation system, and a software architecture facilitating parallel computation and system extensibility. The model serves a wide range of meteorological applications across scales from tens of meters to thousands of kilometers. The effort to develop WRF began in late 1990s and was a collaborative partnership principally among NCAR, NOAA (represented by the National Centers for Environmental Prediction [NCEP] and the (then) Forecast Systems Laboratory [FSL]), the U.S. Air Force Weather Agency (AFWA), the Naval Research Laboratory, the University of Oklahoma, and the Federal Aviation Administration (FAA).

WRF can generate atmospheric simulations using real data (observations, analyses) or idealized conditions. WRF is currently in operational use at NCEP, AFWA, and other centers. The WRF system contains two dynamical solvers, referred to as the ARW (Advanced Research WRF) core and the NMM (Nonhydrostatic Mesoscale Model) core.

Figure 1 shows the flowchart for the WRF Modeling System Version 3. As shown in the diagram, the WRF Modeling System consists of four major programs: the WRF Preprocessing System (WPS), WRF-DA, ARW solver, and post-processing and visualization tools.

The WPS program is used primarily for real-data simulations. Its functions include 1) defining simulation domains; 2) interpolating terrestrial data (such as terrain, land use, and soil types) to the simulation domain; and 3) degribbing and interpolating meteorological data from another model to the simulation domain. The WRF-DA program is optional, but can be used to ingest observations into the interpolated analyses created by WPS. It can also be used to update WRF model's initial conditions when the WRF model is run in cycling mode. The ARW solver is the key component of the modeling system, which is composed of several initialization programs for idealized, and real-data simulations, and the numerical integration program.

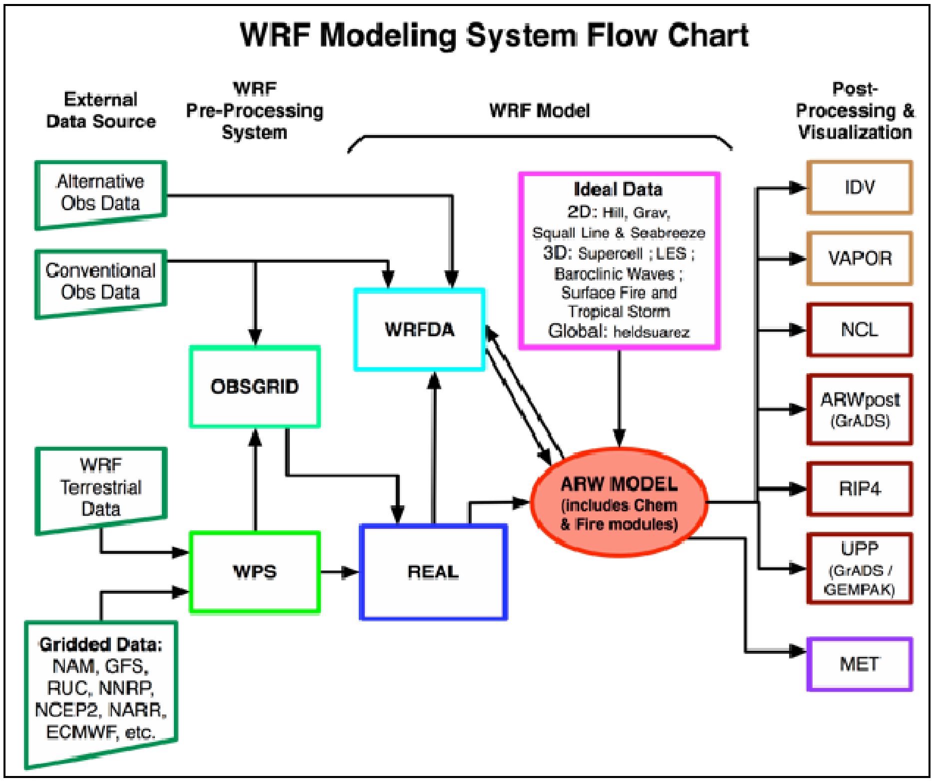

Figure 1. A flowchart describing the different components of the WRF Modeling System Version 3.

The WRF model version 3.5 (Skamarock et al., 2008) is implemented in a configuration with two nested grids. The largest domain is the North American West Coast with a horizontal resolution of 18 km; the inner domain covers the U.S. West Coast area with a horizontal resolution of 6 km (Figure 2). The coarser grid reproduces the large-scale synoptic features that force the local dynamics in the second grid. The coarser grid simulation was first run independently. It was initialized with the Climate Forecast System Reanalysis (CFSR) reanalysis for 30 December 1994 and integrated for 20 years with time-dependent boundary conditions interpolated from the same 6-hourly reanalysis. 40 vertical levels are used (0.0016, 0.0044, 0.0065, 0.0085, 0.0109, 0.0142, 0.0183, 0.0224, 0.0265, 0.0306, 0.0347, 0.0389, 0.0431, 0.0473, 0.0527, 0.0595, 0.0663, 0.0740, 0.0852, 0.1010, 0.1234, 0.1511, 0.1948, 0.2508, 0.3052, 0.3630, 0.4244, 0.4898, 0.5601, 0.6361, 0.7191, 0.8101, 0.9110, 1.0244, 1.1548, 1.3117, 1.4905, 1.6888, 1.9238, units: 10^4 m). SST forcing is derived from the Operational Sea Surface Temperature and Sea Ice Analysis (OSTIA) 1-Day product (Donlon et al., 2009). The nested domain was initialized from the CFSR reanalysis on 30 December 1994 and integrated in one-way nesting mode for 20 years.

A full set of parameterization schemes is included in WRF. The model configuration is setup with the following parameterizations that have proved in previous experiments to be the most accurate for U.S. West Coast: the WRF Single-Moment 6-class scheme microphysics (Hong and Lim, 2006); the Kain-Fritch cumulus parameterization (Kain and Fritsch, 1990); the rapid radiative transfer model (RRTM) for longwave radiation, based on the work by Mlawer et al. (1997); the Dudhia scheme (Dudhia, 1989) for shortwave radiation; the Noah land surface model

(Skamarock et al., 2008); and the planetary boundary layer (PBL) scheme used is the Mellor-Yamada-Nakanishi-Niino version 2.5 (MYNN2.5) (Nakanishi and Niino, 2006). An atmospheric surface layer parameterization, adapted from the so-called Common Ocean Reference Experiment (CORE) bulk formulation (Large, 2006), has been implemented by our WRF team to predict air-sea fluxes over water.

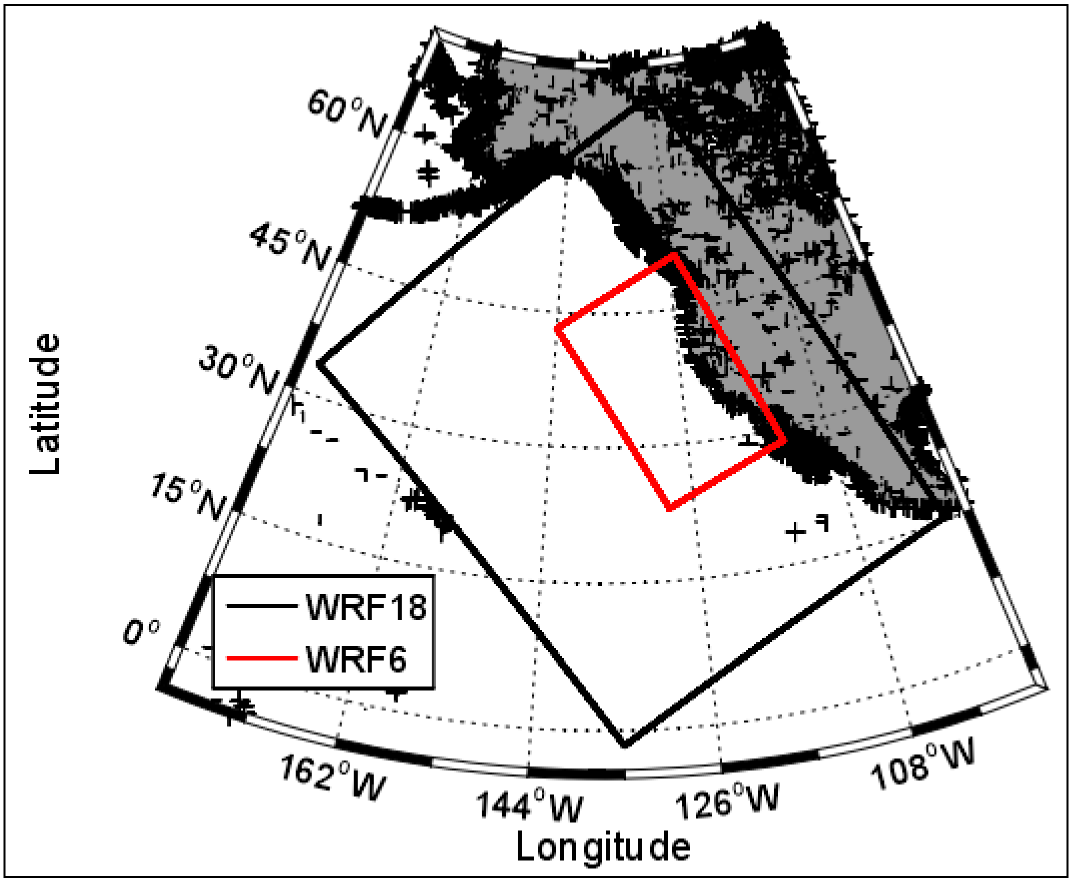

Figure 2. WRF model domain.

The black and red boxes represent the 18 km and 6 km resolution domains, respectively.

2.2 The ROMS hindcast

2.2.1 ROMS

The oceanic simulations are performed with the ROMS (Shchepetkin and McWilliams, 2005). The ROMS version used in this study is ROMS_AGRIF (ROMS-Adaptive Grid Refinement In Fortran), which is maintained by Institut de Recherche pour le Développement (IRD; *Research Institute for Development*) and Institut National de Recherche en informatique et en Automatique (INRIA; *French National Institute for Computer Science and Applied Mathematics*). ROMS is a new generation ocean circulation model that has been specially designed for accurate simulations of regional oceanic systems. The model solves the primitive equations in an Earth-centered rotating environment, based on the Boussinesq approximation and hydrostatic vertical momentum balance. It is discretized in coastline- and terrain-following curvilinear coordinates using high-order numerical methods. ROMS is a split-explicit, free-surface oceanic model, in which short time steps are used to advance the surface elevation and barotropic momentum equations, with a larger time step used for temperature, salinity, and baroclinic momentum. A third-order, upstream-biased advection operator allows the generation of steep gradients in the solution, enhancing the effective resolution of the solution for a given grid size when the explicit viscosity is small.

In this study, the ROMS model has two domains (**错误!未找到引用源。**). The outer domain (domain 1) extends from 142.1° W to 114.4° W and from 23.9° N to 50.0° N with a horizontal resolution of 4 km and has 42 vertical levels. The inner domain (domain 2) covers the central and southern part of California (Figure) with a horizontal spatial resolution of 1 km. The model has 42 vertical levels. The vertical s-coordinate parameter settings are $\theta_s = 6, \theta_b = 0.5, and\ h_c = 250$ m. These values give a higher resolution in the upper layer of the ocean. Vertical mixing is parameterized using the K-Profile Parameterization (KPP) boundary layer formulation (Large et al. 1994), and the dominant lateral mixing is due to the upstream-biased advection operator.

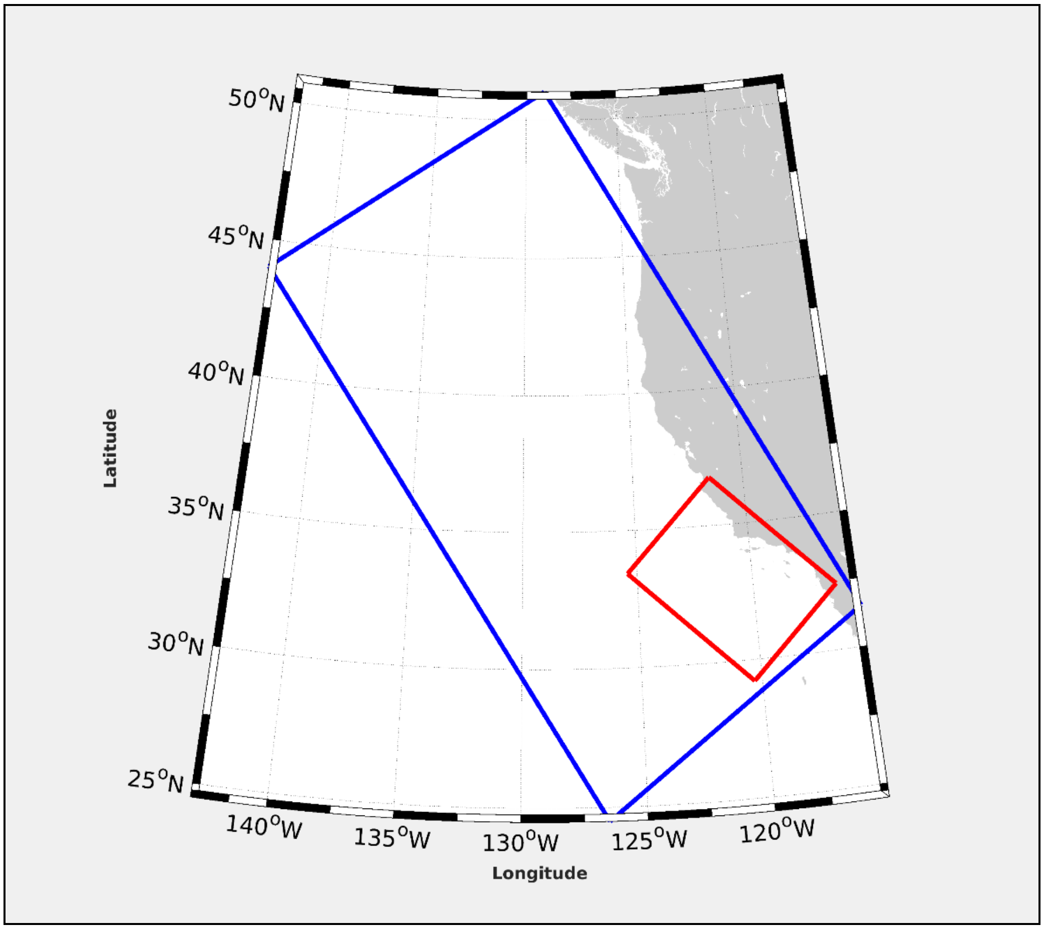

Figure 3. Two nested ROMS model grids.

The blue and red boxes represent the 4 km and 1 km resolution domains, respectively. An enlarged inner model domain with 1 km horizontal grid resolution can be seen in Figure.

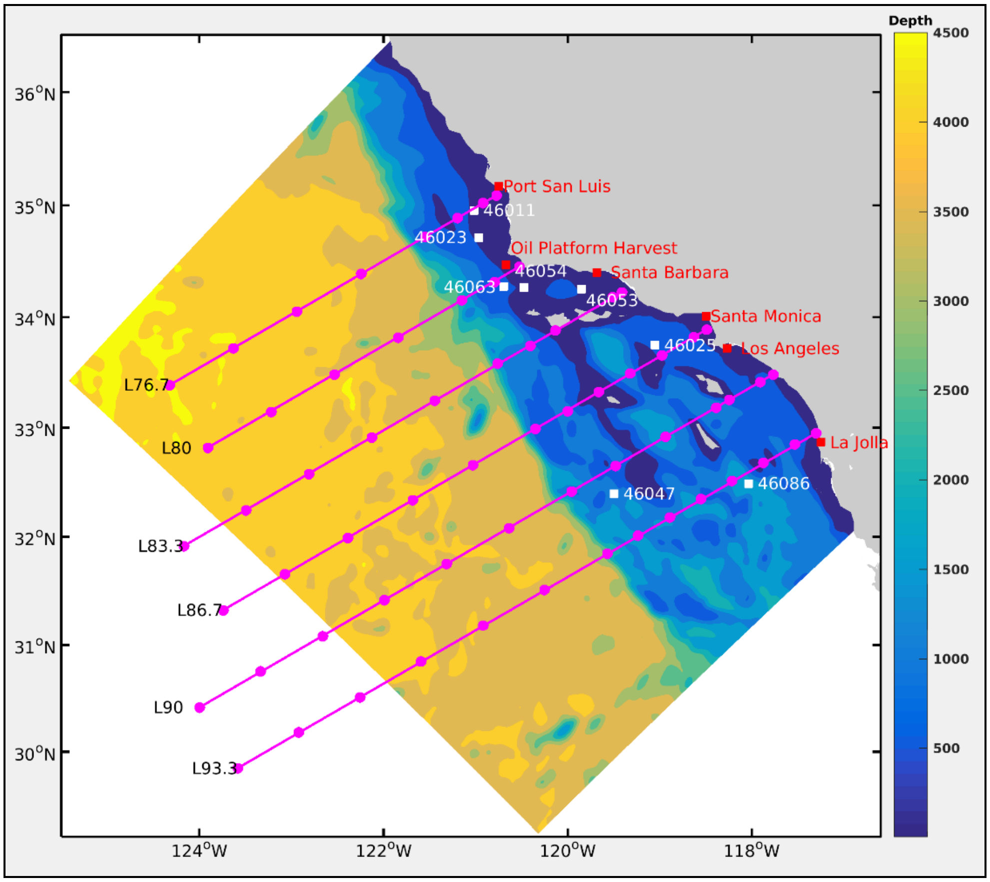

Figure 4. ROMS model domain and bathymetry.

The color shadings show the bathymetry (units: m). Pink lines are the CalCOFI cruise lines with dots showing stations and line numbers marked on the western ends. White squares denote the National Buoy Data Center (NDBC) buoy stations. Red squares represent six tidal gauges, including the station ID.

2.2.2 Surface boundary conditions

This model configuration was forced by 10 years (2004–2013) of WRF products with 6 km horizontal resolution. WRF provides ROMS with the following atmospheric fields every 1 hour: 2 m air temperature, specific humidity, surface wind vector, net shortwave and downwelling longwave fluxes, and precipitation, depicted in Figure. A bulk Formulation (CORE, Large et al., 2006) has been implemented and is used to compute the turbulent heat and momentum fluxes.

2.2.3 Lateral boundary conditions

Mixed boundary conditions are used along the open boundaries. The Orlanski radiation condition (Orlanski, 1976). is applied in the tangential direction, and the Flather condition (Flather, 1976) with adaptive restoration of material properties is imposed under inflow conditions. The restoring data of domain 1 for the lateral open-boundary conditions are from the daily HYCOM (HYbrid Coordinate Ocean Model) global oceanic reanalysis product with a horizontal resolution of 1/12 degrees and 40 vertical levels. It includes temperature, salinity, currents, and SSH. The solid boundary around the islands and the mainland has no-normal and no-slip conditions implemented through a landmask algorithm. The lateral boundary conditions of domain 2 (this study) lateral are supplies from domain 1.

Table 1. Comparison between D09 and this study

Type	D09	This study
Version	ROMS_AGRIF	ROMS_AGRIF v3.1.1
Surface boundary conditions	MM5	WRF
Lateral boundary conditions	Nested grids: Domain1: SODA Domain2: one-way nested with Domain1 Domain3: one-way nested with Domain2	Nested grids: Domain1: HYCOM Domain2: one-way nested with Domain1
Vertical Mixing parameterization	KPP scheme	KPP scheme
Grid Settings	Nested grids: Domain1: 20 km Domain2: 6.7 km Domain3: 1.0 km	Nested grids: Domain1: 4 km Domain2: 1 km
Vertical s-coordinate parameters	$\theta_s = 5.0, \theta_b = 0, h_m = 10\ m$	$\theta_s = 6.0, \theta_b = 0.5, h_c = 250\ m$
Bathymetry	ETOPO2	ETOPO1
Data assimilation	-	EnOI
Tidal model	-	TPX07

2.3 The SWAN hindcast

The SWAN model is a third-generation wave model based on the action density balance equation. The SWAN model solves the evolution of the action density equation:

$$\frac{\partial}{\partial t} N + \frac{\partial}{\partial x}\left(C_x N\right) + \frac{\partial}{\partial y}\left(C_y N\right) + \frac{\partial}{\partial \sigma}\left(C_\sigma N\right) + \frac{\partial}{\partial \theta}\left(C_\theta N\right) = \frac{S(\sigma, \theta; x, y, t)}{\sigma} \quad (1),$$

where C_x and C_y are x and y components of the group velocity corrected for propagation on a current with a given velocity and $S(\sigma,\theta;x,y,t)$ is the source term which represents effects of generation, dissipation, and non-linear wave–wave interactions. It is usually given by

$$\begin{aligned} S(\sigma,\theta) &= S_{inp}(\sigma,\theta) + S_{wcp}(\sigma,\theta) + S_{nl4}(\sigma,\theta) + S_{brk}(\sigma,\theta) \\ &+ S_{frc}(\sigma,\theta) + S_{nl3}(\sigma,\theta) \end{aligned} \quad (2)$$

These terms denote, respectively, the deep-water source terms for generation due to wind input, dissipations due to whitecapping, non-linear quadruplet wave-wave interactions, and the shallow water source terms for dissipations due to depth-induced wave breaking, bottom friction, and triad wave-wave interactions. Details of these processes can be found in the SWAN manual.

This study uses SWAN version 41.01 with the recommended default setting: for whitecapping the expression by Janssen et al. (1989, 1991) is applied. Quadruplet interactions are used. The Joint North Sea Wave Project (JONSWAP) bottom friction formulation is used with C_{fjon}= 0.038 m^2s^{-3} according to Zijlema et al. (2012). Depth-limited wave breaking is modelled according to the bore-model of Battjes and Janssen (1978) using alfa = 1 and gamma = 0.73.

The spatial resolution for the wave model is 0.02 ° (1/50 °) for the computational grid for both longitude and latitude. The wave spectrum is discretized in 24 directions with a constant spacing of 15 ° and 24 geometrically spaced frequency bands over the frequency interval 0.0418–1 Hz. The simulation domain for the computational grid is bounded by longitude 115 °–126 °W and latitude 28 °–38 °N with a fine grid resolution of 0.02 ° for both directions. Details about geographical limits and parameters of the grid settings can be found in Table 2. Figure shows the model domain and the buoy stations.

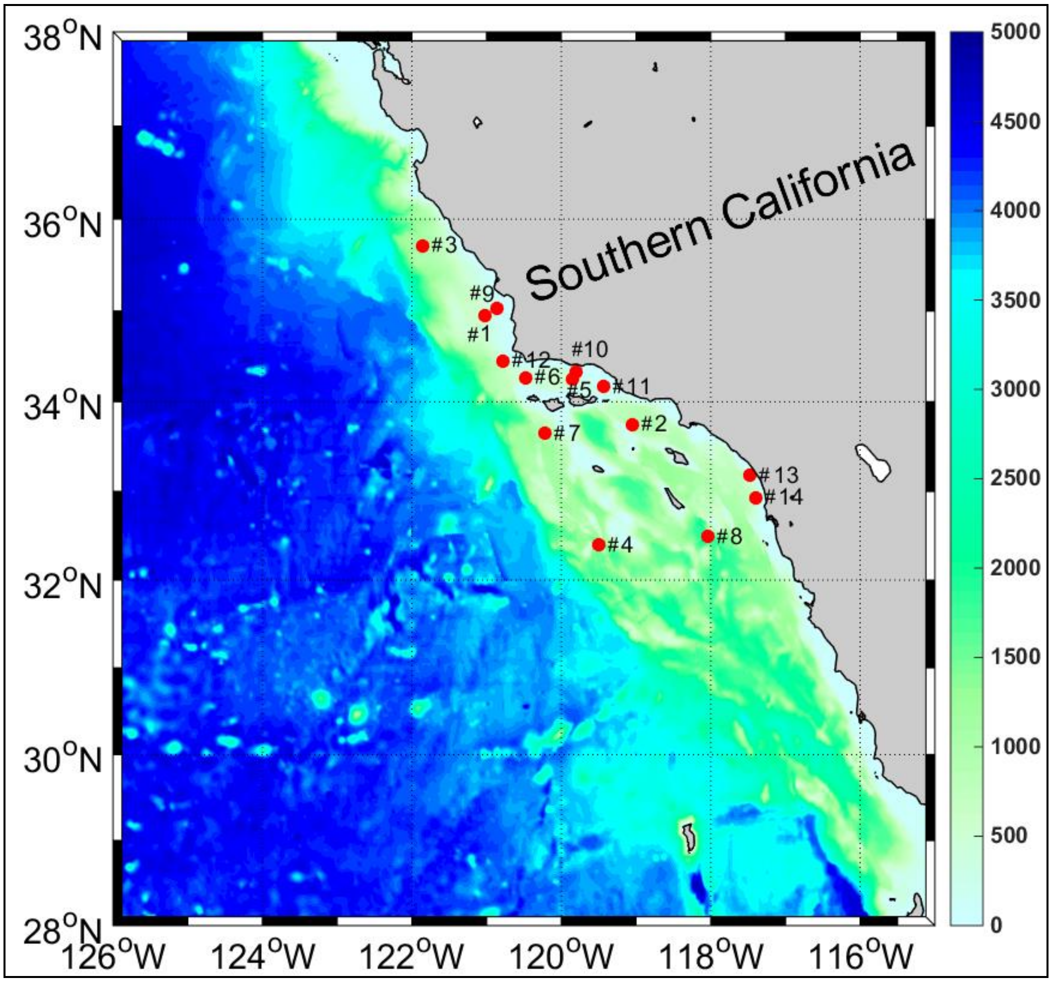

Figure 5. SWAN model domain and bathymetry (units: m).
Red dots represent 14 buoy stations.

Table 2. Grid settings of SWAN model

Parameter	Computational grid
Latitudes	38°–48°N
Longitudes	115°–126°W
Spatial resolution	0.02°×0.02°
Number of points in X-direction	550
Number of points in Y-direction	500

The bathymetry data used in wind-wave modeling were obtained from the ETOPO1 dataset of the National Geophysical Data Center by NOAA. ETOPO1 is a 1 arc-minute global relief model of Earth's surface that integrates land topography and ocean bathymetry. It was built from numerous global and regional datasets. The spatial resolution of the bathymetry data is 0.0167 °×0.0167 °.

As illustrated in Figure, the wind fields generated by the WRF model are used for calculating wave field in the SWAN model. As the SCB belongs to open sea, the European Centre for Medium-Range Weather Forecasts (ECMWF) data is used as the wave boundary condition. The ECMWF data is a comprehensive numerical modeling system with the data assimilation of observational data. It provides a variety of products, including the ERA-Interim datasets, which are used in the SWAN model. It is produced with different versions of the Integrated Forecasting System (IFS), including atmospheric model and data assimilation system developed by the ECMWF (Aarnes et al., 2015). The ERA-Interim is based on a 2006 release of the IFS (Cy31r2). The detailed description of IFS can be found in the homepage of the ECMWF.

The SWAN model was applied in non-stationary mode because the area of interest is too large to allow stationary computations as the time scale of wave propagation through the area of interest is larger than the time scale of changes in wind forcing. We have applied the SWAN model with a time step of 5 minutes and 4 iterations per time step were found to be sufficient.

2.4 Data assimilation

A state-of-the-art data assimilation is applied to assimilate the observational data into the oceanic current product by the ROMS. The ROMS has developed several data assimilation methods, such as 3D-Var, 4D-Var, Ensemble Kalman Filter (EnKF), Ensemble Optimum Interpolation (EnOI), and Nudging. Since the project aims to produce 10-year high-resolution hindcast product, both computation efficiency for the simulation and product accuracy need to be considered. For this purpose, the EnOI is chosen for this project (Figure). The analysis step of EnOI is similar to that of a traditional EnKF but much less expensive (Oke et al., 2005, Counillon and Bertino, 2009). It has been widely used in the Australian Bluelink system (Oke et al. 2010) and also in engineering projects by the PI. It has been approved as an efficient and reliable data assimilation approach. The observational data assimilated into the ROMS include satellite remote sensing data (SSH and SST) and in situ data (CalCOFI ship-borne data) (Table 3). Model Validation and Analysis Model results (buoy, sea surface salinity (SSS), tidal gauges, HF radar, etc.) have been assessed against the observational data. D09 has conducted an extensive evaluation and analysis of the 1996–2007 SCB product as noted above based on multiple scales of the variation.

Table 3. Datasets for assimilation

Type	Variables	Description	Source	Time	Location
SSH	Sea level anomaly	TOPEX/Poseidon, Jason -1/2	JPL, NASA	2004–2013	SCB
SST	Sea surface Temperature	AVHRR	NOAA	2004–2013	SCB
Cruise	Temperature and salinity	Cruise observations	CalCOFI	2004–2013	SCB

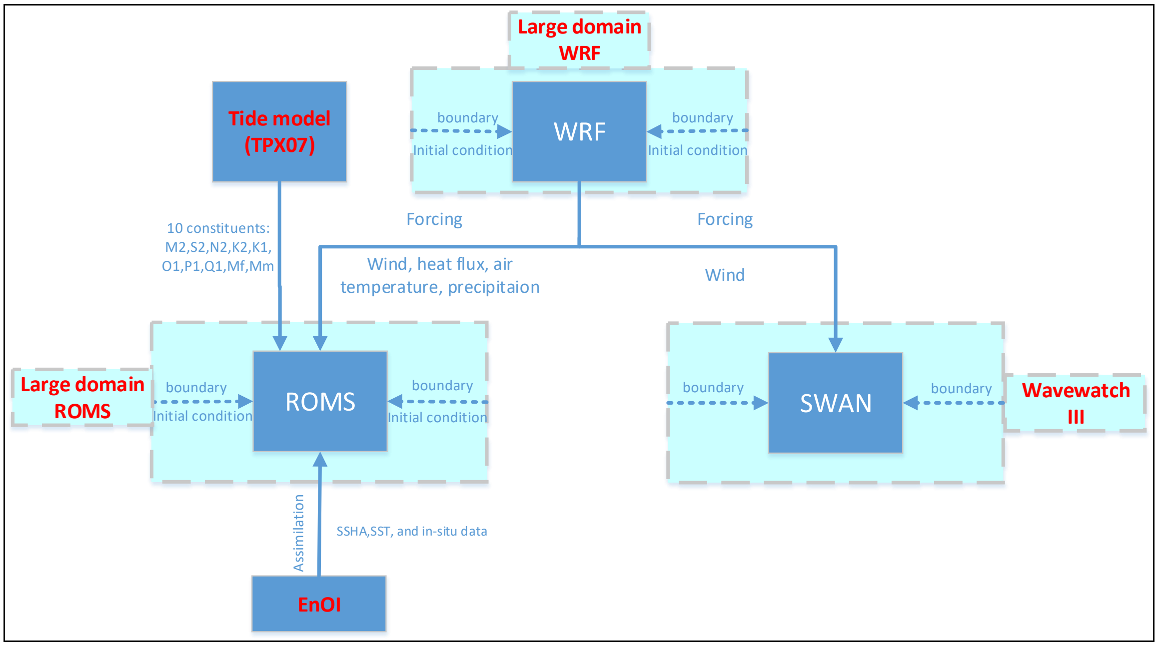

Figure 6. Schematic diagram of the model configurations.

3. Data Management

Data management involves two types of data:

(1) Observational data
The project collects all the observational data within the model domain, including NDBC buoy data, tidal gauge data, satellite remote sensing data (SST, SSH, wind, etc.), CalCOFI cruise data. The collected observational data have been saved in standard MATLAB® format and saved at the Department of Atmospheric and Oceanic Sciences, UCLA.

(2) Numerical output
The numerical output from WRF, ROMS, and SWAN has been saved in a standard Network Common Data Form (NetCDF) format at the Department of Atmospheric and Oceanic Sciences, UCLA. Numerical output summarized in Table 4 has been copied to individual disks and delivered to agencies. No sensitive or personal information is kept in the project data files.

Table 4. List of model output variables

Model	Variables	Time span	Dimension	Temporal frequency	Horizontal resolution	Vertical levels
WRF	Horizontal wind velocity	2004–2013	(x, y)	hourly	6 km	Sea surface
ROMS	Horizontal current velocity	2004–2013	(x, y, z)	hourly	1 km	42
	Vertical current velocity	2004–2013	(x, y, z)	hourly	1 km	42
	temperature	2004–2013	(x, y, z)	hourly	1 km	42
	salinity	2004–2013	(x, y, z)	hourly	1 km	42
	Sea surface height	2004–2013	(x, y)	hourly	1 km	Sea surface
	Vertical viscosity	2004–2013	(x, y, z)	hourly	1 km	42
	Vertical averaged currents	2004–2013	(x, y)	hourly	1 km	Vertical-averaged
	Surface mixed layer thickness	2004–2013	(x, y)	hourly	1 km	Sea surface

Model	Variables	Time span	Dimension	Temporal frequency	Horizontal resolution	Vertical levels
SWAN	Significant wave height, Swell wave height, Mean wave direction, Peak wave direction, Direction of energy transport, Peak period, Average absolute wave period, Mean absolute wave period, Mean absolute zero-crossing period, Wind velocity	2004–2013	(x, y)	hourly	1 km	Sea surface

4. Validation of the WRF Simulation

4.1 Observational data

The hourly wind data from the NDBC and the Cross-Calibrated Multi-Platform (CCMP; Atlas et al. 1996) 10-m winds over the California shelf for the period of 2004–2013 are used to validate the U.S. West Coast wind from the WRF simulation. The buoys used in this study are summarized in Table 5. Note that the anemometer height correction has not been applied on the data used.

Table 5. Buoy stations for WRF model output validation

No.	Latitude (° N)	Longitude (° W)
46011	34.96	121.01
46012	37.36	122.88
46013	38.24	123.30
46014	39.23	123.97
46022	40.74	124.57
46026	37.75	122.84
46027	41.85	124.38
46028	35.71	121.86

The CCMP gridded surface vector winds are produced using satellite, moored buoy, and model wind data, and as such, are considered to be a Level-3 ocean vector wind analysis product. A new version of CCMP vector wind analysis fields, Version-2 (V2.0) CCMP L3, is now available from Remote Sensing Systems (RSS) as daily NetCDF4 files containing six-hourly wind field maps. The V2 CCMP processing combines Version-7 RSS radiometer wind speeds, QuikSCAT and Advanced Scatterometer (ASCAT) wind vectors, moored buoy wind data, and ERA-Interim model wind fields using a Variational Analysis Method (VAM) to produce four maps daily of 0.25 °×0.25 °gridded vector winds.

This study also uses the pentad Global Precipitation Climatology Project (GPCP) precipitation data (Adler et al., 2003) on a 2.5 °×2.5 °grid from 1979 to 2010 to obtain the observed climatological mean precipitation.

4.2. Validation of 10-m winds

4.2.1 Comparison between the CCMP observations and WRF simulation

Figure displays the seasonal mean CCMP winds averaged from 2004 to 2013. Season definition throughout the document is: winter (December, January, and February), spring (March, April, and May), summer (June, July, and August), and fall (September, October, and November). In winter (Figurea), strong southwesterlies occur in the northern part of the region, and northwesterlies appear along the U.S. southwest coast. In the subtropical region, easterly wind prevails. In spring (Figureb), westerlies are located in the northern region with smaller magnitude compared to winter. Meanwhile, northwesterlies off the California coast intensify significantly. In summer (Figurec), northerlies dominate along the U.S. West Coast with the maximum off the California coast. Wind pattern in fall (Figured) resembles that of winter season, but with smaller wind speed.

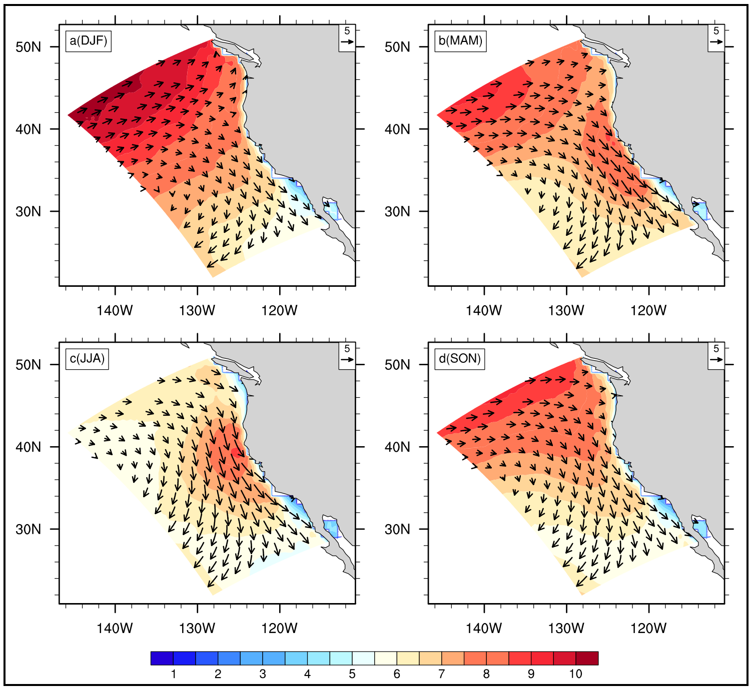

Figure 7. Seasonal mean CCMP 10-m winds (vectors; units: m s-1) and wind speed (color shadings; units: m s-1) in (a) winter, (b) spring, (c) summer, and (d) fall.

The WRF simulation reproduces the seasonal mean 10-m winds fairly well (Figure). Strong northerlies off the California coast are evident in spring and summer. The pattern correlation coefficients between the CCMP and WRF wind speed are 0.94, 0.87, 0.70, and 0.90 for winter, spring, summer, and fall, respectively. This shows that WRF did not capture the summertime wind speed as accurately in the other seasons. It is due to WRF simulated nearshore wind speed being much larger than that in the CCMP data during summer. The region with strong wind is also much broader in the WRF output. This may arise from the high resolution of the WRF model.

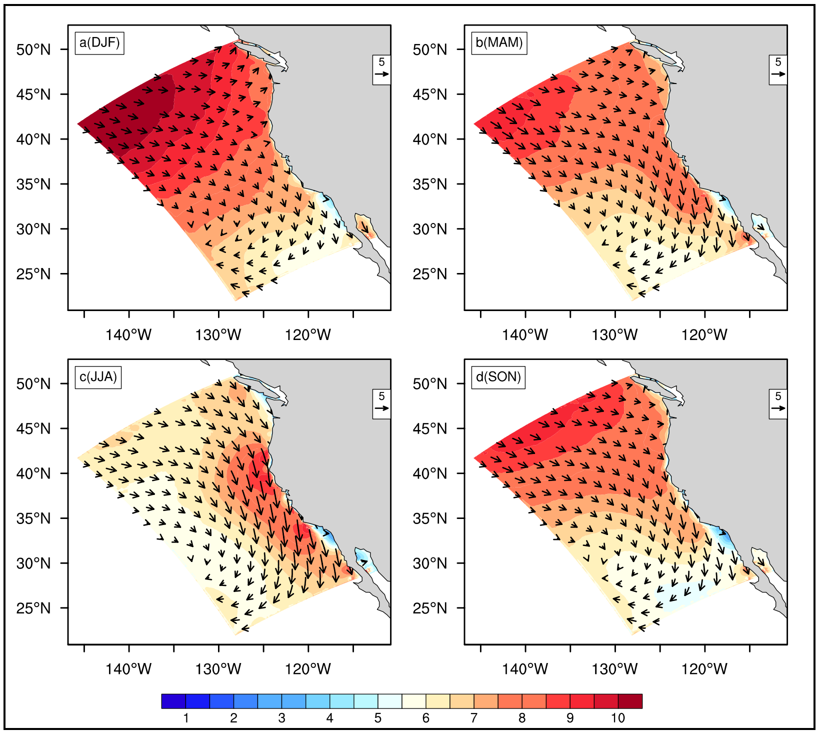

Figure 8. Same as Figure, but for the WRF simulation.

CCMP wind speed averaged along 140 °–100 °W (red curves in Figure) displays pronounced seasonal variation, with the strongest meridional difference in winter and a peak of about 7 m s^{-1} near 40 °N in summer. The WRF simulation captures the characteristics reasonably well (black curves in Figure).

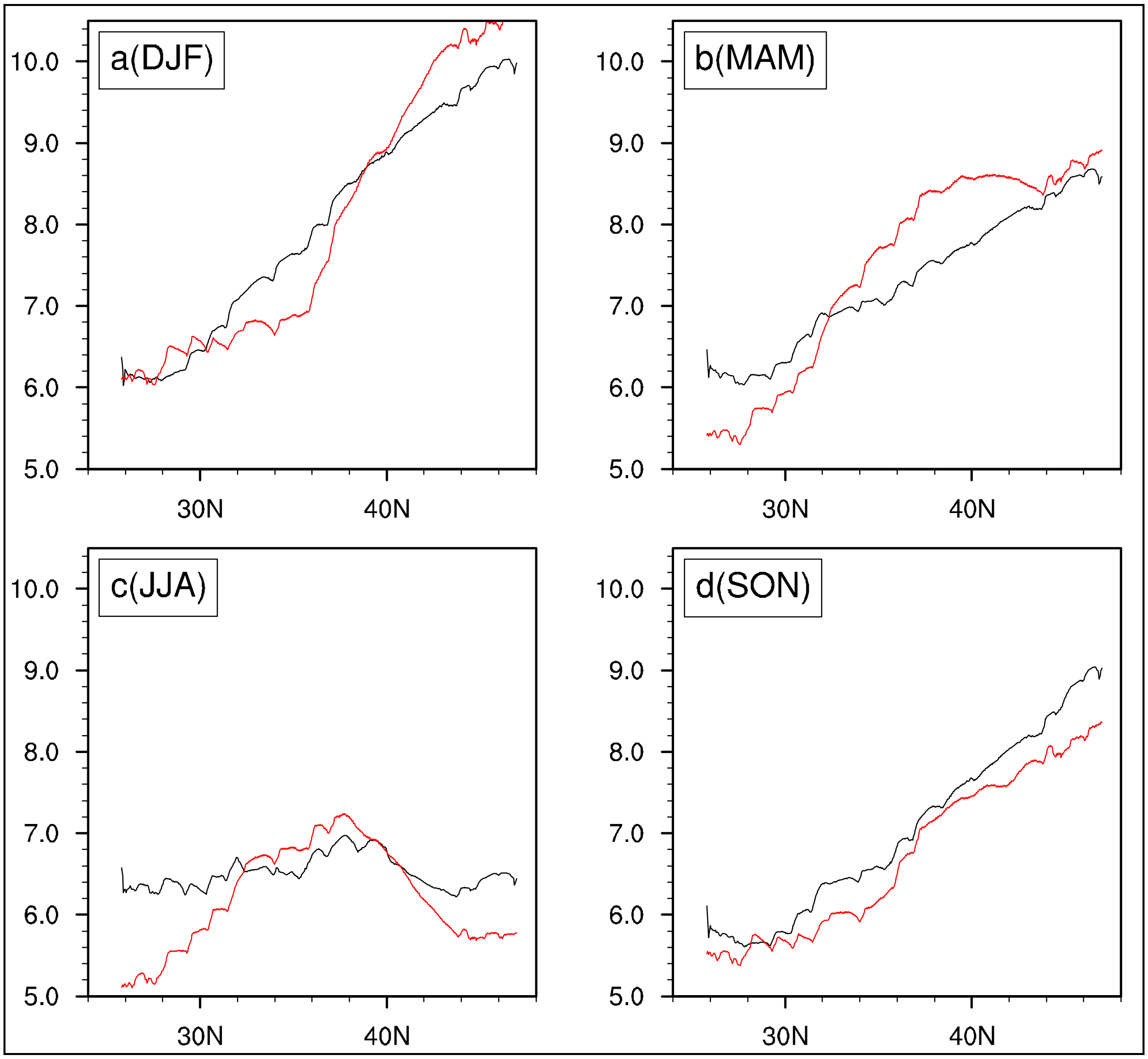

Figure 9. Seasonal mean CCMP (red curves) and WRF simulated (black curves) 10-m wind speed (units: m s-1) averaged along 140°-100°W in (a) winter, (b) spring, (c) summer, and (d) fall.

Figure shows the CCMP wind curl. Strong cyclonic wind curl occurs in the nearshore zone during all four seasons. In winter and spring, the northern part of the domain was dominated by cyclonic wind curls The WRF simulation (Figure) is consistent with the observations where large wind curl values are observed along the coast. In addition, the strongest wind curl occurs in summer in both observations and WRF simulation.

To present a clearer picture of the wind curl in the nearshore zone, the WRF simulated monthly mean 10-m wind curl close to the coast from January to December in 2004 is displayed (Figure). It is evident that the wind curl is much stronger in spring and summer than that in winter and fall. Combined with the monthly variations in wind speed (Figure), it is found that large wind shear in spring and summer gives rise to the concurrent large wind curl. In addition, the wind shear is related to the wind drop-off phenomenon, which is characterized by a weakening of the wind speed close to the coast. The wind drop-off characteristics exhibit a similar seasonal variability as the wind speed but with much stronger wind drop-off in spring and summer. The results are in agreement with the work done by Capet et al. (2004) and Renault et al. (2016).

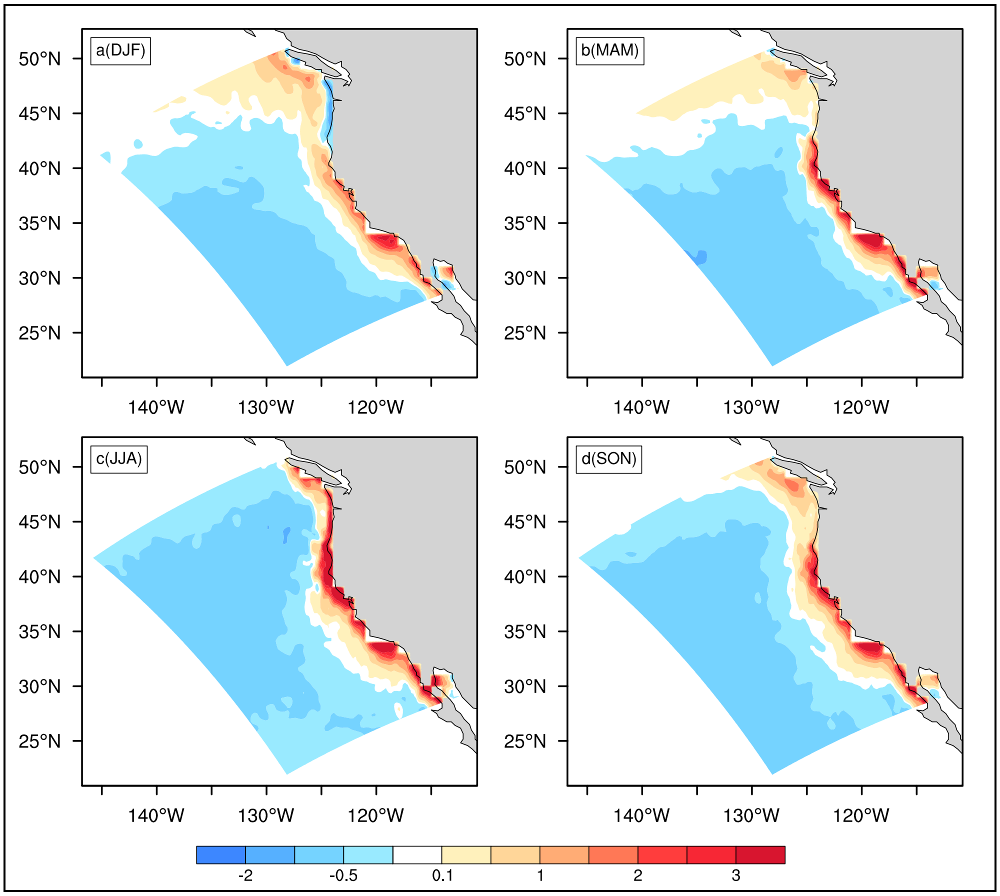

Figure 10. Seasonal mean CCMP 10-m wind curl (color shadings; units: 10^{-5} s^{-1}) in (a) winter,

(b) spring, (c) summer, (d) and fall.

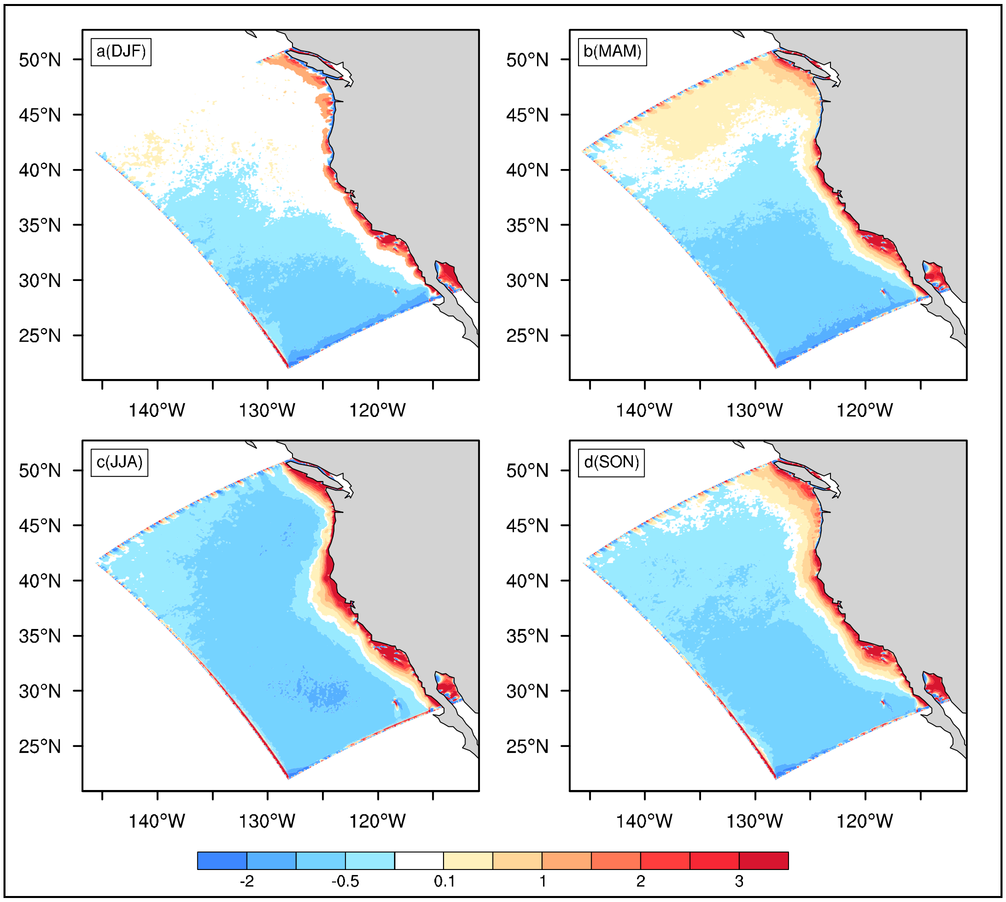

Figure 11. Same as Figure, but for the WRF simulation.

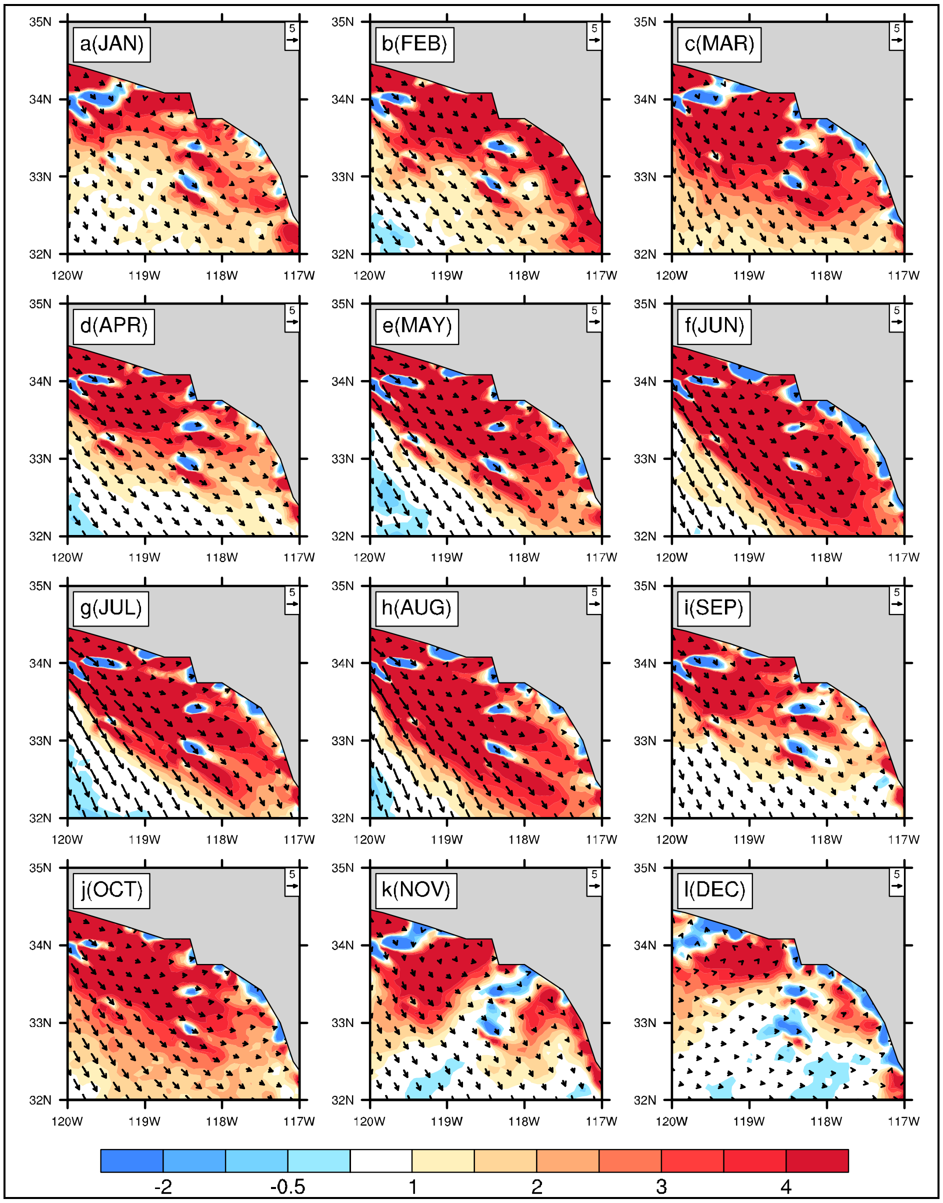

Figure 12. WRF simulated monthly mean 10-m wind curl (color shadings; units: 10^{-5} s^{-1}) and winds (vectors; units: m s^{-1}) from (a–l) January to December in 2004.

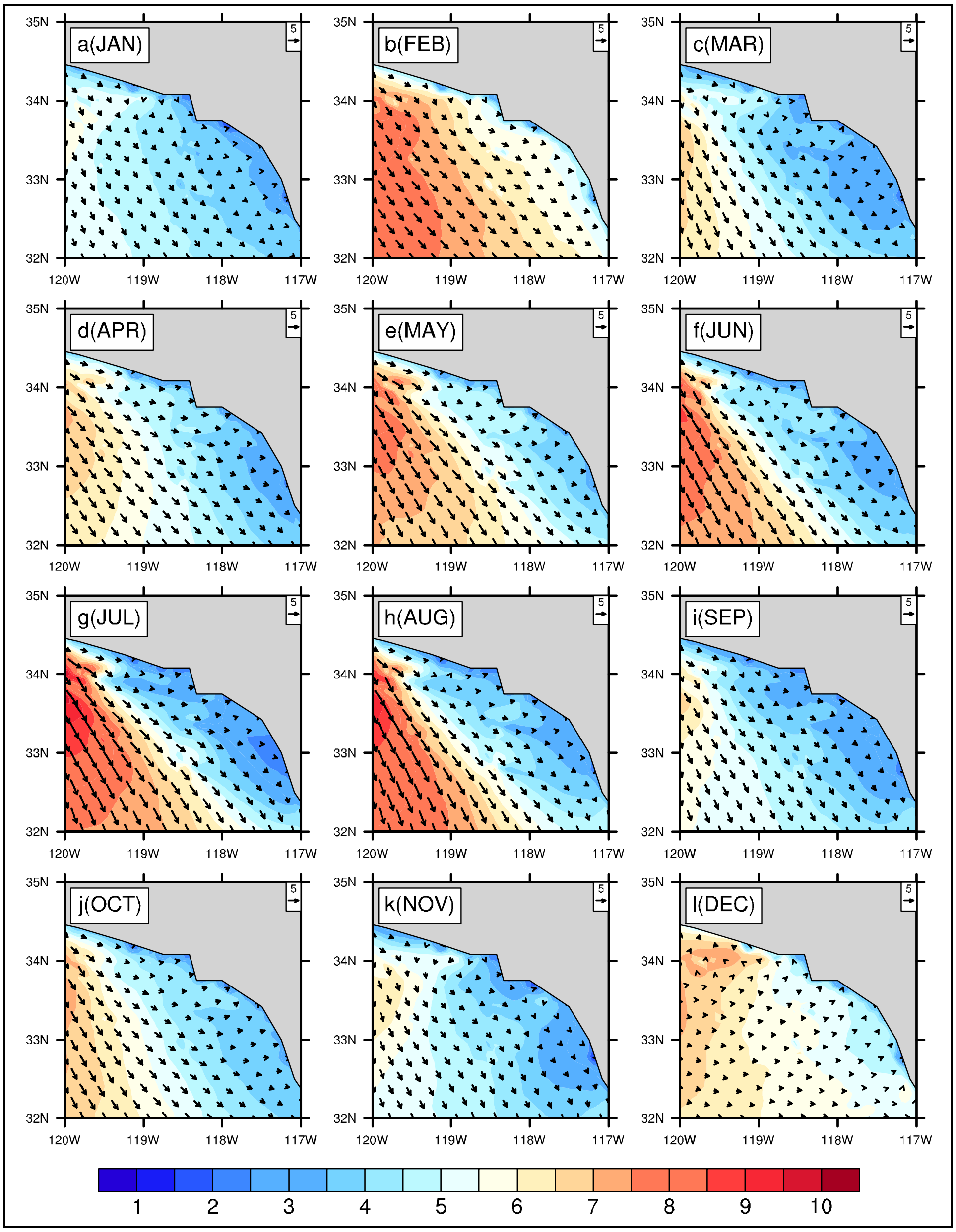

Figure 13. WRF simulated monthly mean 10-m wind speed (color shadings; units: m s^{-1}) and winds (vectors; units: m s^{-1}) from (a–l) January to December in 2004.

Figure presents the interannual variations of model domain mean wind speed for both observations and WRF simulation. The correlation coefficients between them are 0.43, 0.81, 0.53, and -0.12 in winter, spring, summer, and fall, respectively. The spring wind speed from the WRF simulation corresponds with the observations better than the other seasons.

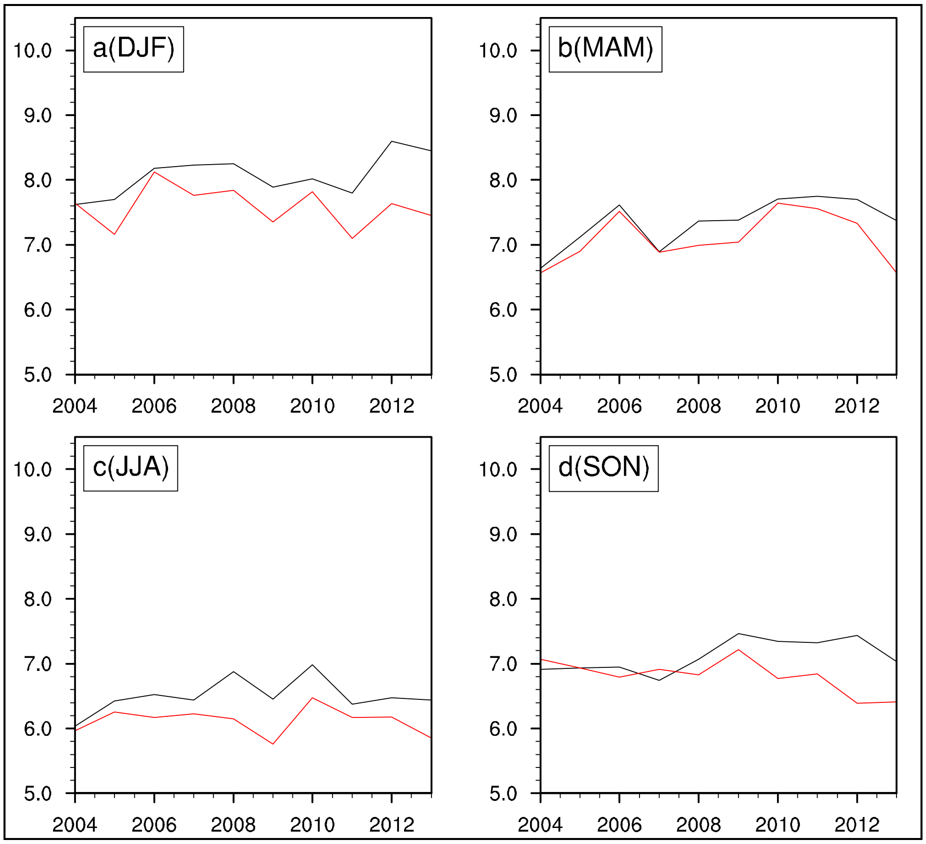

Figure 14. Interannual variations of model domain mean wind speed (units: m s^{-1}) from the WRF simulation (black curves) and observations (red curves) in (a) winter, (b) spring, (c) summer, and (d) fall.

4.2.2 Comparison between the buoy observations and WRF simulation

Buoy data are used to validate the WRF simulation in the nearshore zone. Figure shows the locations of the buoys used in this study. Figure depicts the interannual variations of wind speed at buoy 46011 for all four seasons. The WRF simulated wind speed is generally stronger than observations, with the largest difference observed in summer. Comparison between the wind speed from WRF simulation and observations at other buoy stations yields similar results. The overestimation of wind speed in the WRF simulation may be due to that the anemometer height correction has not been applied to the buoy data.

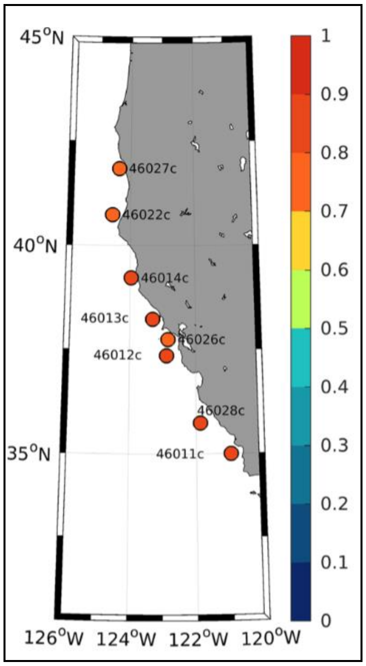

Figure 15. Locations of the buoys used in this study.

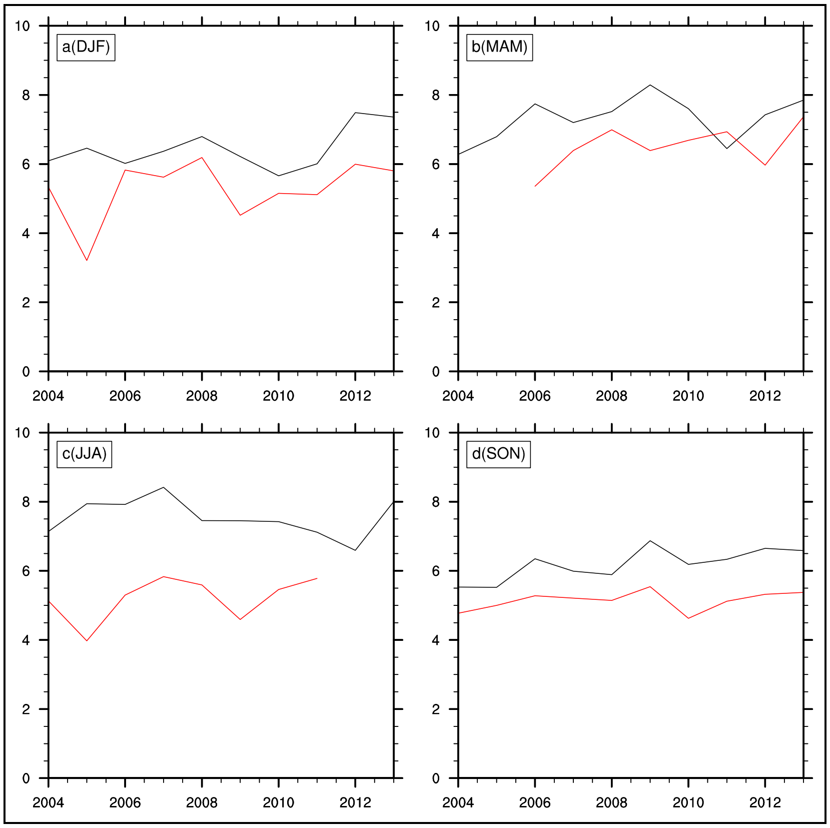

Figure 16. Interannual variations of wind speed (units: m s^{-1}) at buoy 46011 from the WRF simulation (black curves) and observations(red curves) in (a) winter, (b) spring, (c) summer, and (d) fall.

Figure illustrates the seasonal mean wind speed at each buoy location. The WRF simulation is in fair agreement with the buoy observations, with correlation coefficients of 0.84, 0.81, 0.78, and 0.85 for winter, spring, summer, and fall, respectively. The simulated wind speed is confirmed to have larger magnitude for all four seasons. The largest difference occurs in summer, sharing consistency with Figure.

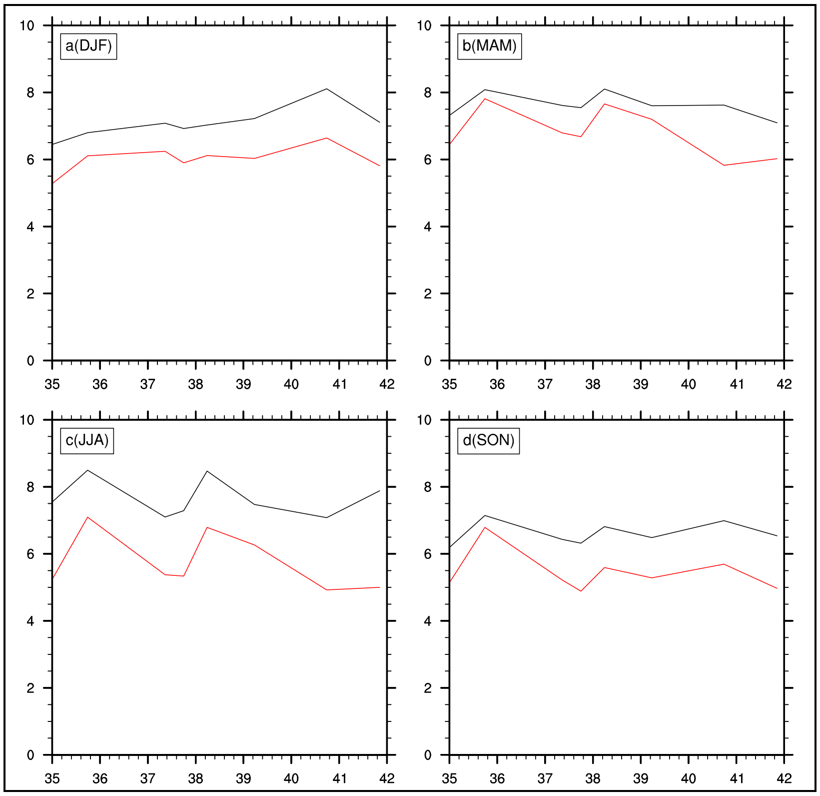

Figure 17. Seasonal mean wind speed (units: m s^{-1}) at each buoy location from the WRF simulation (black curves) and observations (red curves) in (a) winter, (b) spring, (c) summer, and (d) fall.

4.3 Validation of precipitation, cloud, and radiation

Figure shows the seasonal mean total precipitation based on the GPCP dataset. Over the U.S. West Coast, precipitation increases from south to north, with the maximum located northwest of Washington State. The precipitation is much greater in winter and fall than that in spring and summer. This is associated with the SST cooling that arises from the strong upwelling in spring and summer (related to the stronger cyclonic wind curl observed in Figure). The WRF simulation captures the primary spatial and temporal variation characteristics of the precipitation, but with stronger precipitation along the coast (Figure). The stronger precipitation may be attributed to the higher resolution of the WRF simulation.

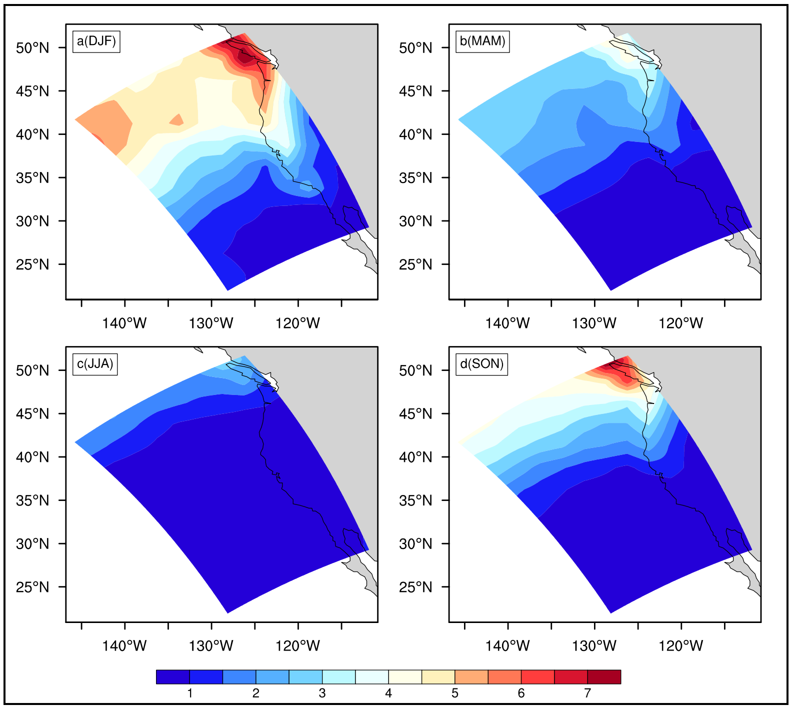

Figure 18. Observed seasonal mean total precipitation (units: mm day^{-1}) in (a) winter, (b) spring, (c) summer, and (d) fall.

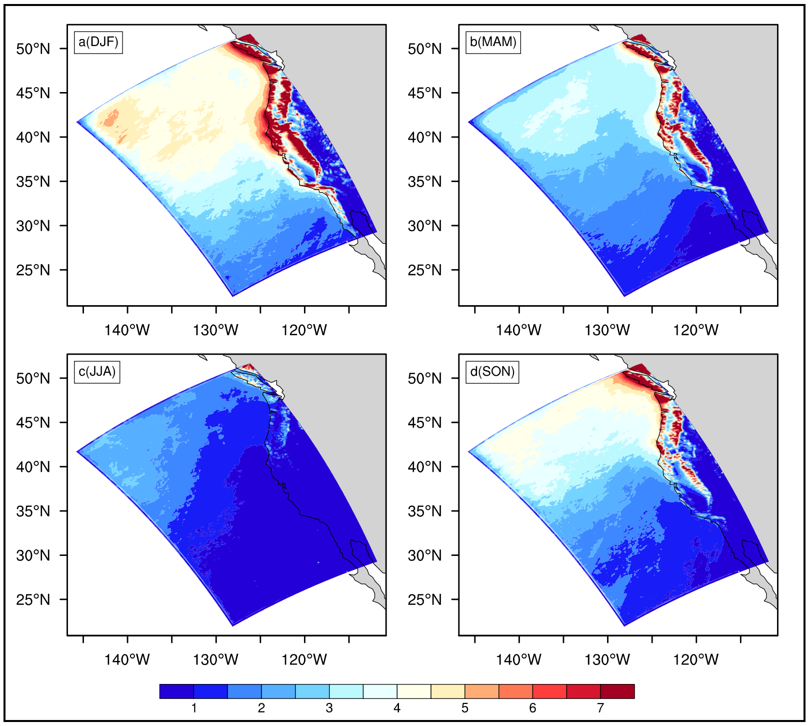

Figure 19. Same as Figure, but for the WRF simulation.

Figure and Figure illustrate the simulated non-convective and convective precipitation, respectively. The non-convective precipitation is the primary contributor of the total precipitation. It determines the spatial pattern in Figure. The large convective precipitation occurs in a narrow band along the coast and over the western part of the model domain.

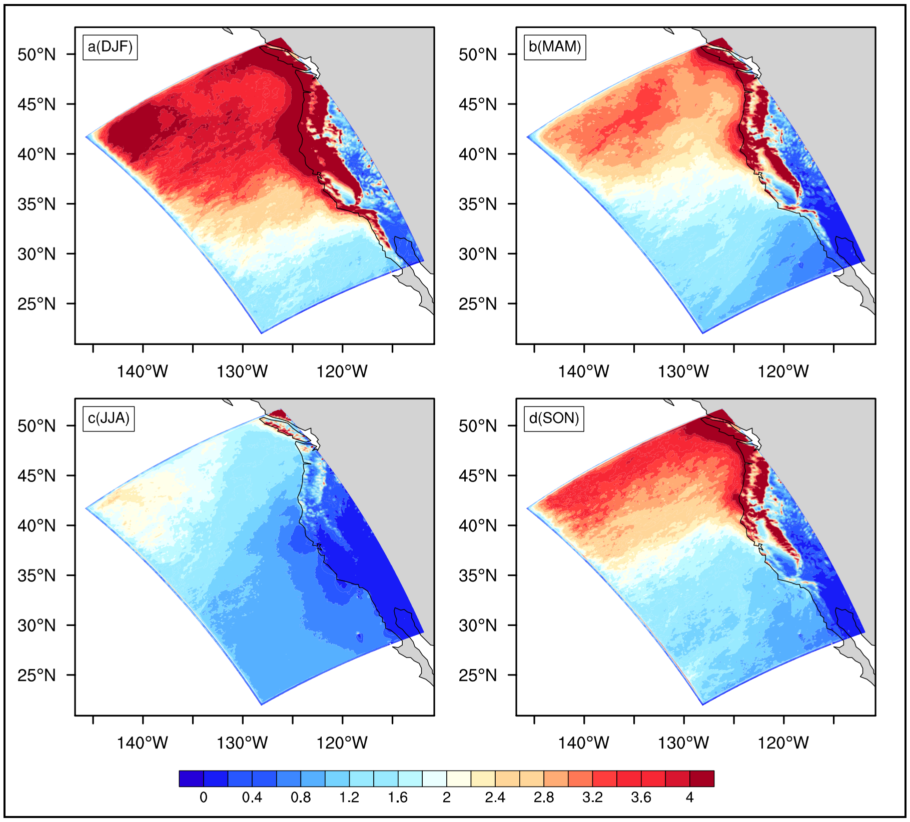

Figure 20. Seasonal mean non-convective precipitation (units: mm day^{-1}) in (a) winter, (b) spring, (c) summer, and (d) fall.

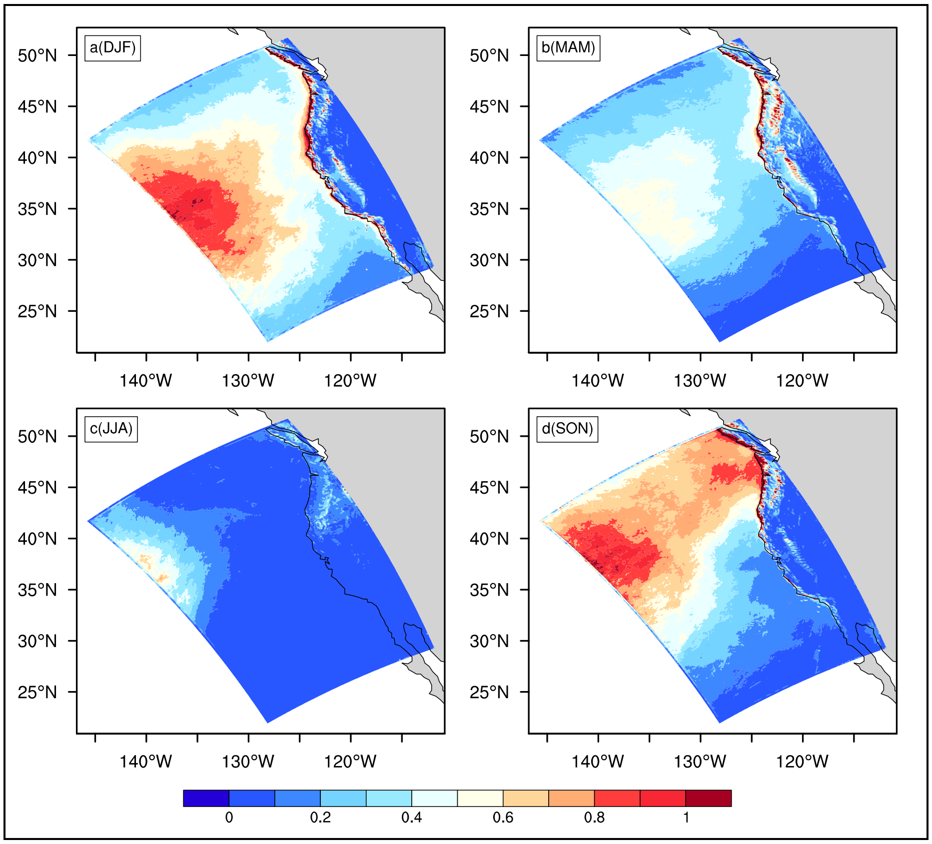

Figure 21. Seasonal mean convective precipitation (units: mm day^{-1}) in (a) winter, (b) spring, (c) summer and (d) fall.

Figure shows the cloud cover (CC) from both observations and WRF simulation. WRF has a general good agreement with the observations and reproduces fairly the seasonal cycle of the CC.

The simulated net shortwave radiation also reproduces both the spatial distribution and seasonality features of the observations (Figure). The realistic representation of the CC in the model demonstrates a fair representation of the shortwave radiation. The maximum biases occur over the Central California region (up to 20 W m^{-2}) where the model has a positive CC bias.

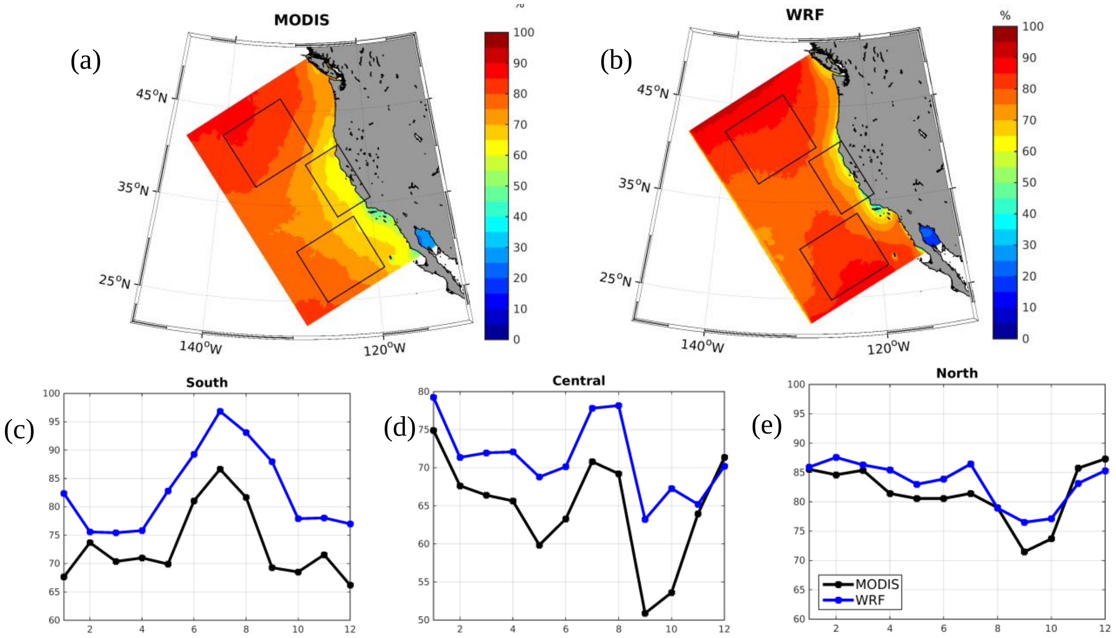

Figure 22. Cloud cover (CC; units: %) from observations and WRF model.

Annual mean from (a) Moderate Resolution Imaging Spectroradiometer (MODIS) satellite and (b) WRF model. (c), (d), and (e) represent the monthly CC variations estimated over the same period from MODIS and WRF averaged over the boxes indicated in (a) and (b).

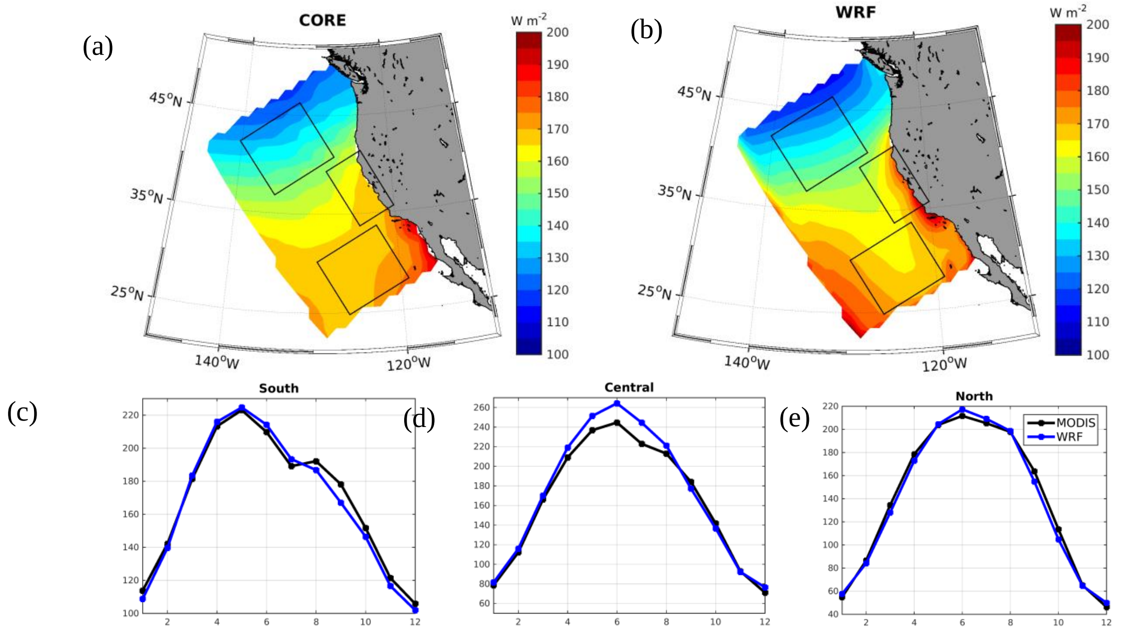

Figure 23. Same as Figure, but for net shortwave radiation.

5. Validation of the ROMS Simulation

5.1 Observational data

To validate the ROMS output, various observation data, including satellite remote sensing, moored buoys and ship-borne measurements, are assembled (Table 6). HF radar derived current data are used to validate the ROMS surface currents. HF radars measure coastal currents in the upper ~1 m using a Doppler radar technique. The data used in this study is from October 2011 through December 2013 and has a horizontal resolution of 6 km.

Since 1949, hydrographic and biological data of the California Current System have been collected on CalCOFI cruises. There are four cruises during each season yearly; that is, in winter, spring, summer, and fall. This study collected 10-year (2004–2013) and 65 cast stations located within the model domain. The temperature and salinity are then averaged seasonally to compare with the model results at each station.

Table 6. Summary of the observational data

Type	Variables	Description	Source	Time	Location
Tidal gauge	Water level	Port San Luis, CA - Station ID: 9412110	CO-OPS station	2004–2013	(35.17° N, 120.75° W)
Tidal gauge	Water level	Oil Platform Harvest, Oil Platform Harvest - Station ID: 9411406	CO-OPS station	2004–2013	(34.47° N, 120.67° W)
Tidal gauge	Water level	Santa Barbara, CA - Station ID: 9411340	CO-OPS station	2005–2013	(34.40° N, 119.69° W)
Tidal gauge	Water level	Santa Monica, CA - Station ID: 9410840	CO-OPS station	2004–2013	(34.00° N, 118.50° W)
Tidal gauge	Water level	Los Angeles, CA - Station ID: 9410660	CO-OPS station	2004–2013	(33.72° N, 118.27° W)
Tidal gauge	Water level	La Jolla, CA - Station ID: 9410230	CO-OPS station	2004–2013	(32.87° N, 117.26° W)
SSH	Sea level anomaly	TOPEX/Poseidon, Jason -1/2	JPL, NASA	2004–2013	SCB
SST	Sea surface temperature	AVHRR	NOAA	2004–2013	SCB
SSS	Sea surface salinity	Aquarius	JPL, NASA	2011–2013	SCB
Cruise	Temperature and salinity	Cruise observations	CalCOFI	2004–2013	SCB

Type	Variables	Description	Source	Time	Location
High frequency Radar	Sea surface currents	High frequency radar systems	IOOS	2011–2013	SCB
Buoy	Temperature and salinity at 3 m	Station 46025	NDBC	2007–2009	(33.74°N, 119.05°W)
Buoy	Temperature and salinity at 2.3 m	Station 46053	NDBC	2007–2008	(34.25°N, 119.85°W)
Buoy	Temperature and salinity at 3 m	Station 46063	NDBC	2007–2009	(34.27°N, 120.7°W)
Buoy	Temperature and salinity at 3 m	Station 46086	NDBC	2006	(32.49°N, 118.03°W)
Buoy	Velocity from 26 m to 202 m	Station 46011	NDBC	2005–2008	(34.96°N, 121.01°W)
Buoy	Velocity from 25 m to 329 m	Station 46023	NDBC	2004–2005	(34.71°N, 120.97°W)
Buoy	Velocity from 23.8 m to 263.8 m	Station 46047	NDBC	2010–2012	(32.40°N, 119.50°W)
Buoy	Velocity from 24 m to 328 m	Station 46053	NDBC	2007	(34.25°N, 119.85°W)
Buoy	Velocity from 25 m to 329 m	Station 46054	NDBC	2004–2005	(34.26°N , 120.48°W)
Buoy	Velocity from 26 m to 330 m	Station 46063	NDBC	2006–2009	(34.27°N, 120.70°W)
Buoy	Velocity at 3.8 m	Station 46086	NDBC	2007, 2010, 2011	(32.49°N, 118.03°W)
Buoy	Velocity from 8 m to 46 m	Station 46233	SCCOOS	2007	(32.94°N, 117.32°W)

5.2 Seasonal mean water temperature, salinity, and currents in the ROMS

Figure 24 shows that the SST is highest in summer and lowest in winter. It reaches 20 ℃ in summer in the southeastern SCB while the highest SST in winter is about 13 ℃. In general, the temperature decreases with increase in latitude. The temperature in the west is warmer than that in the east. However, there is a warm pool (33.5 °N, 118 °W) in the east. The warm pool starts in spring, and reaches its highest intensity in summer.

Figure 25 shows that the sea water temperature at 50 m is lower than the surface. The highest temperature is around 17 ℃ occurring in fall and the lowest temperature (about 10 ℃) unexpectedly occurs in summer. The coastal water temperature is very cold in summer as compared to other seasons because of the upwelling current. The upwelling currents develop in spring and reach the strongest in summer. The spatial distribution of the sea temperature at 50 m is difference from that at the surface. Latitude is not the major influencing factor of water temperature.

As depth increases to 100 m, the water temperature further decreases (Figure 26). The seasonal variation becomes weak. Both the highest temperature (about 13 ℃) and lowest temperature (about 9 ℃) occur in summer. The cold water close to the coast is closely related to upwelling.

There is no significant seasonal variation of sea water temperature at a depth of 200 m (Figure 27). The highest temperature is about 9 ℃ and the lowest temperature is about 7.5 ℃.

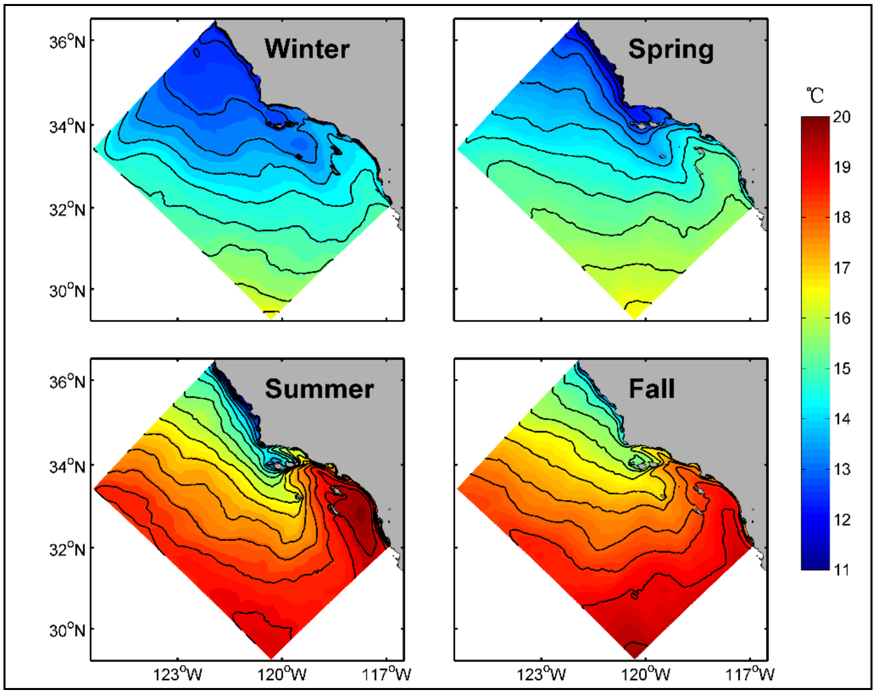

Figure 24. 10-year (2004-2013) seasonal mean temperature (units: °C) at the surface.

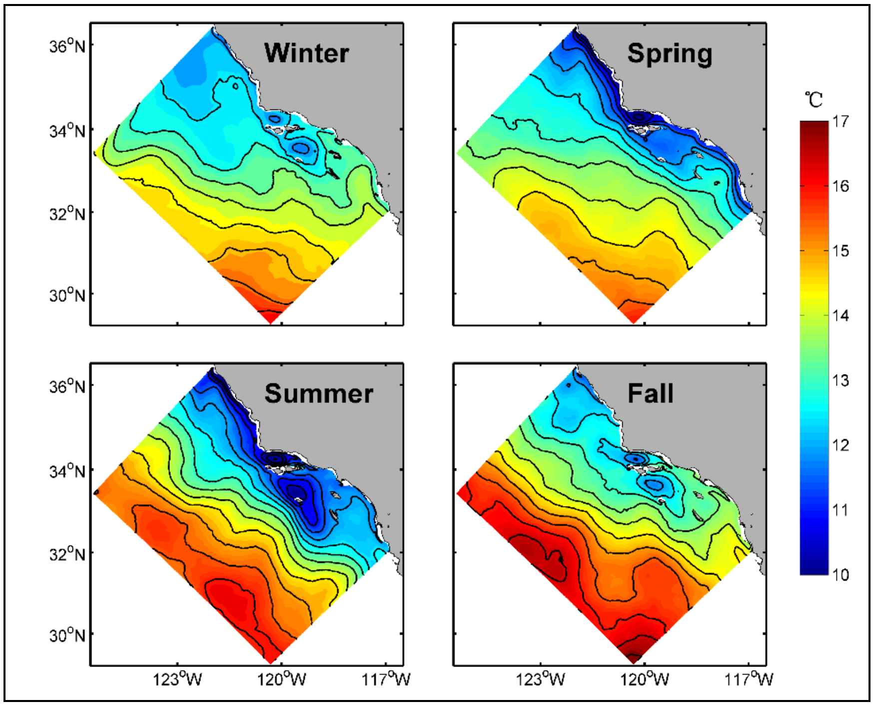

Figure 25. 10-year (2004–2013) seasonal mean temperature (units: °C) at a water depth of 50 m.

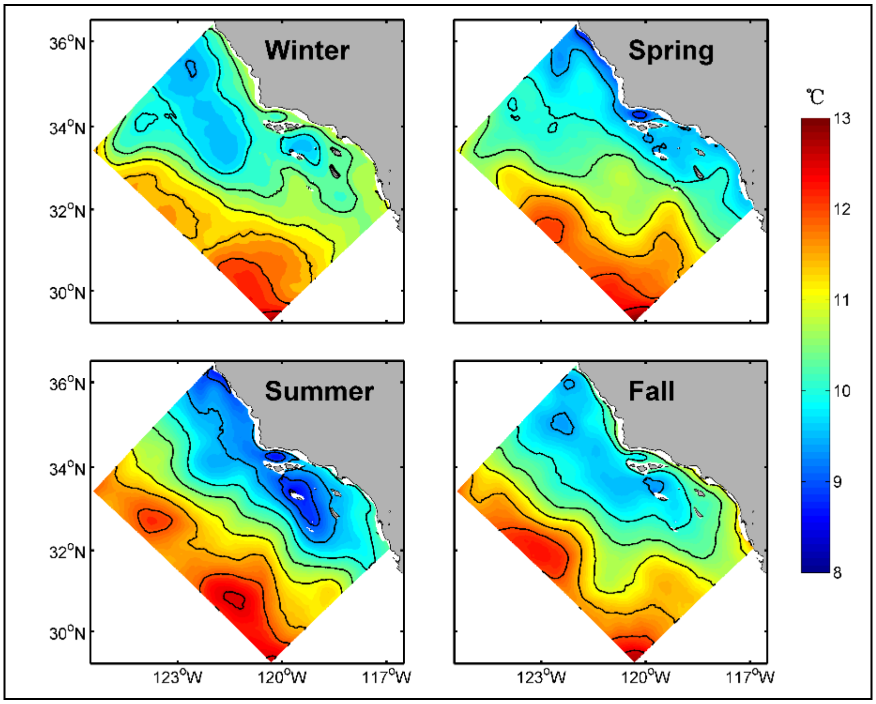

Figure 26. Same as Figure 25, but for 100 m.

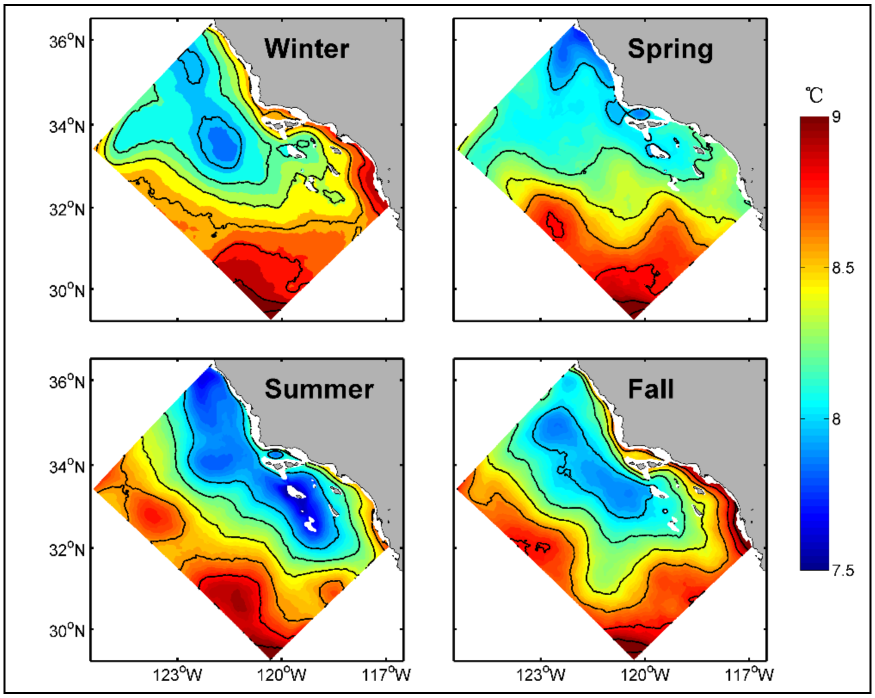

Figure 27. Same as Figure 25, but for 200 m.

Figure 28 shows that salinity is higher in the southeast and lower in the northwest part of the domain. Salinity is especially high near the coast. The highest salinity occurs in summer, with the maximum [about 33.7 PSU (practical salinity unit)] values observed in the southeast. In winter, the salinity is lower, with a minimum of about 33.1 PSU recorded in the northwest.

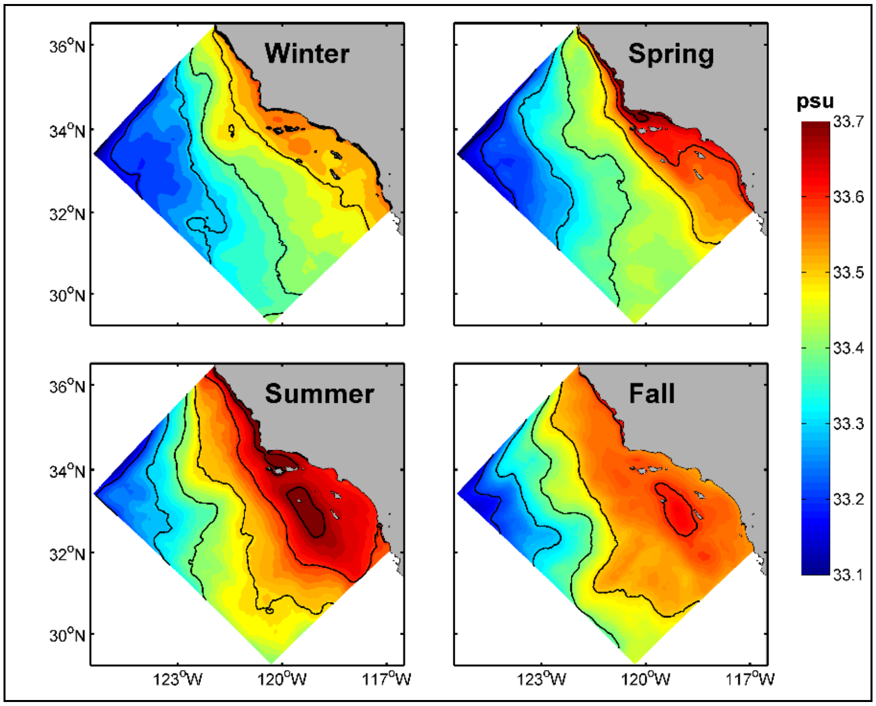

Figure 28. 10-year (2004–2013) seasonal mean salinity (units: PSU) at sea surface level.

Figure 29 shows the salinity at a water depth of 50 m. The salinity is lower in northwest and higher near the coast. In summer, the salinity is higher, with a maximum of about 33.8 PSU observed around the Channel Islands of California. In winter, the salinity is lower with the minimum of about 33.1 PSU located in the northwest.

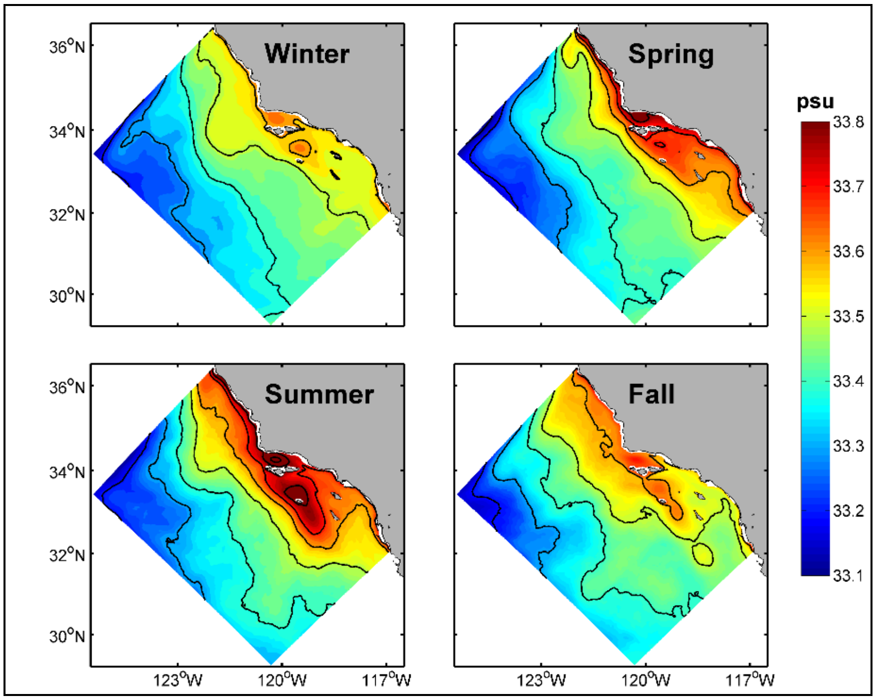

Figure 29. 10-year (2004–2013) seasonal mean salinity (units: PSU) at a water depth of 50 m.

In all four seasons, the salinity at the water depth of 100 m is lower (higher) away from (close to) the coast (Figure 30). The salinity near the coast is highest with a maximum (about 34 PSU) in summer, and lowest in winter. The 200 m salinity features (Figure 31) are similar to those at a depth of 100 m.

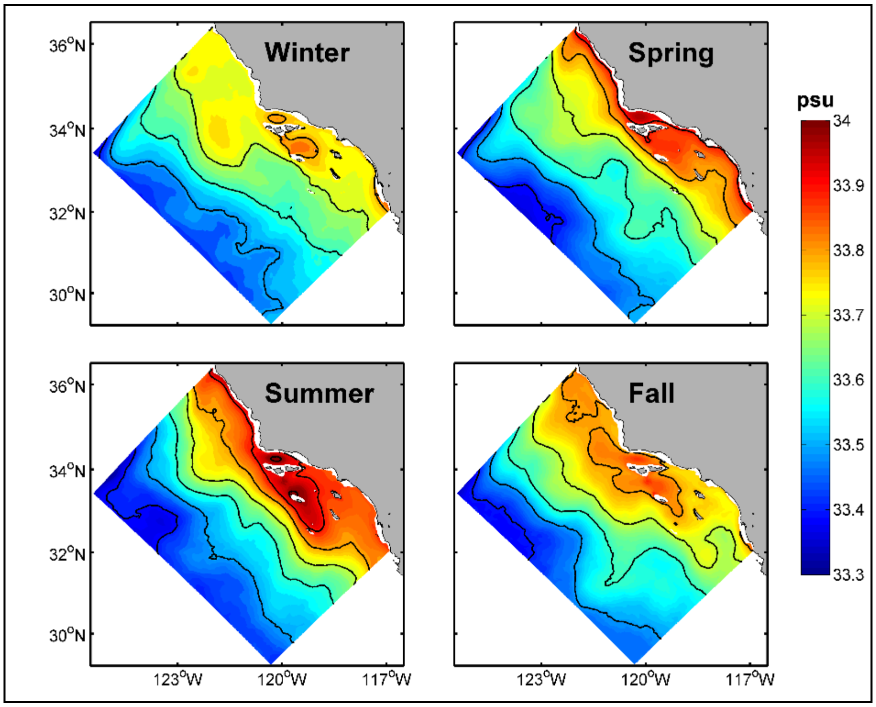

Figure 30. Same as Figure 29, but for 100 m.

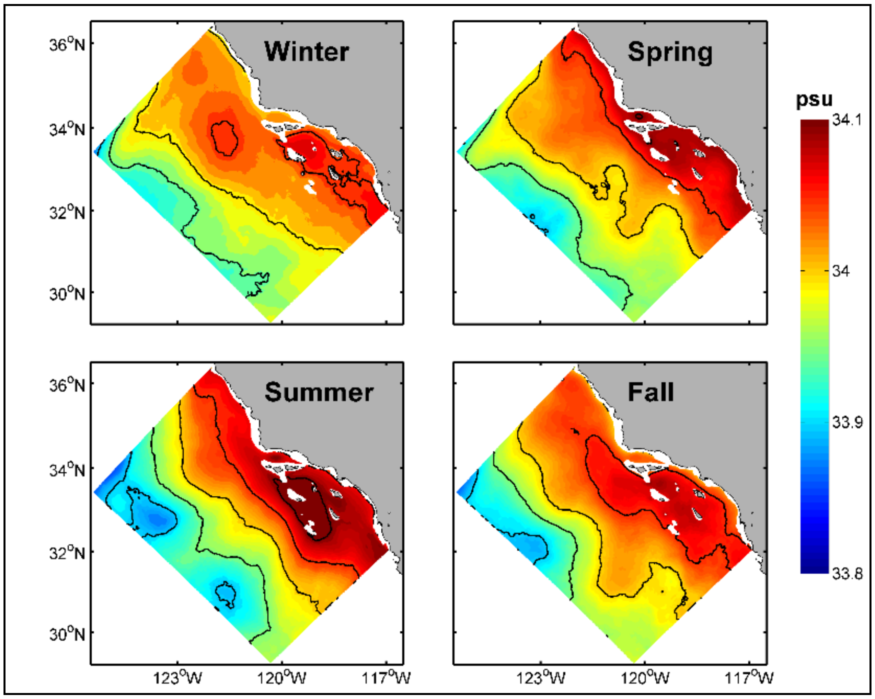

Figure 31. Same as Figure 29, but for 200 m.

Figure 32 shows the seasonal mean currents at sea surface. A significant seasonality of sea surface currents exists within the domain. The strongest flow occurs in summer where the largest velocity reaches 0.2 m s^{-1}. The flow is weakest in winter as compared to the other seasons. In winter, the largest velocity at sea surface is about 0.1 m s^{-1}. An eddy is evident in the northwest. In spring, the strong currents occur along the coast.

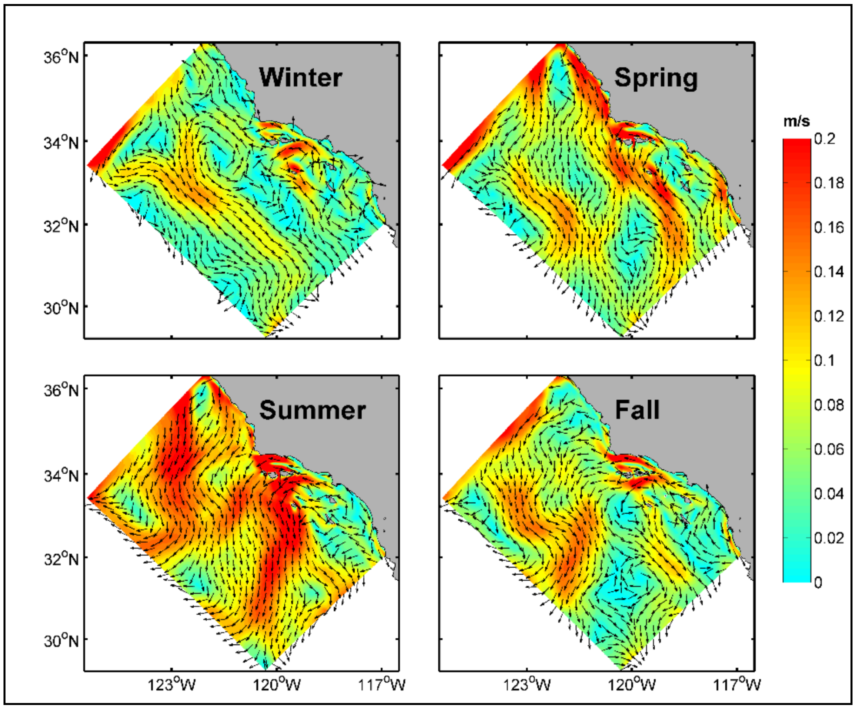

Figure 32. 10-year (2004–2013) seasonal mean currents (units: m s^{-1}) at sea surface level. Vectors represent the directions, and color shadings show the magnitude.

Figure 33 and Figure 34 show that the current velocities at 50 m and 100 m, respectively, are smaller than at the surface. The strongest flow occurs nearshore. In all four seasons, the current at both 50 and 100 m displays high velocity around the Santa Barbara Channel (SBC) in line with Auad et al. (1998).

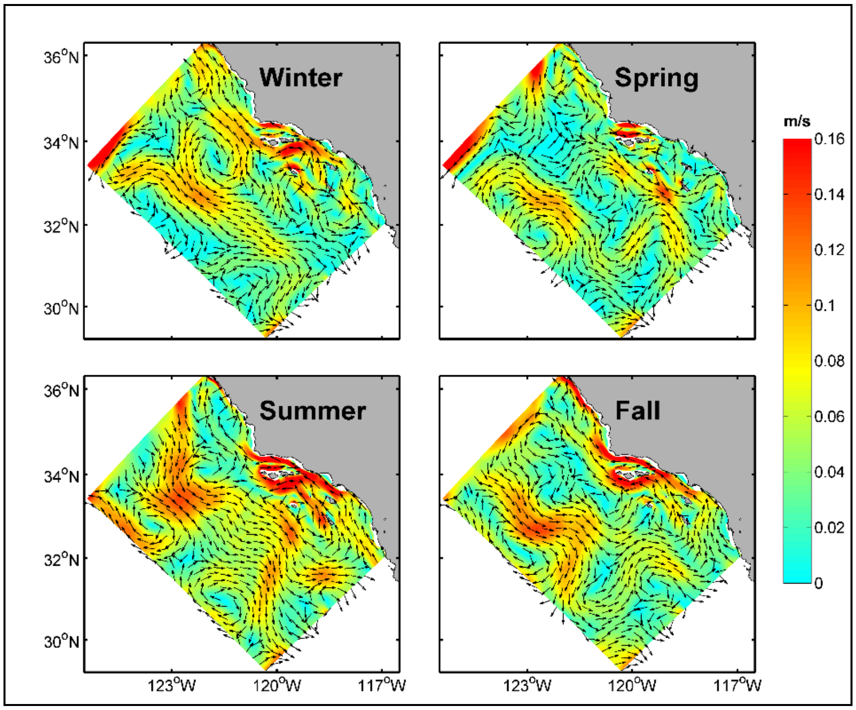

Figure 33. 10-year (2004-–013) seasonal mean currents (units: m s^{-1}) at a water depth of 50 m. Vectors represent the direction and color shadings show the magnitude.

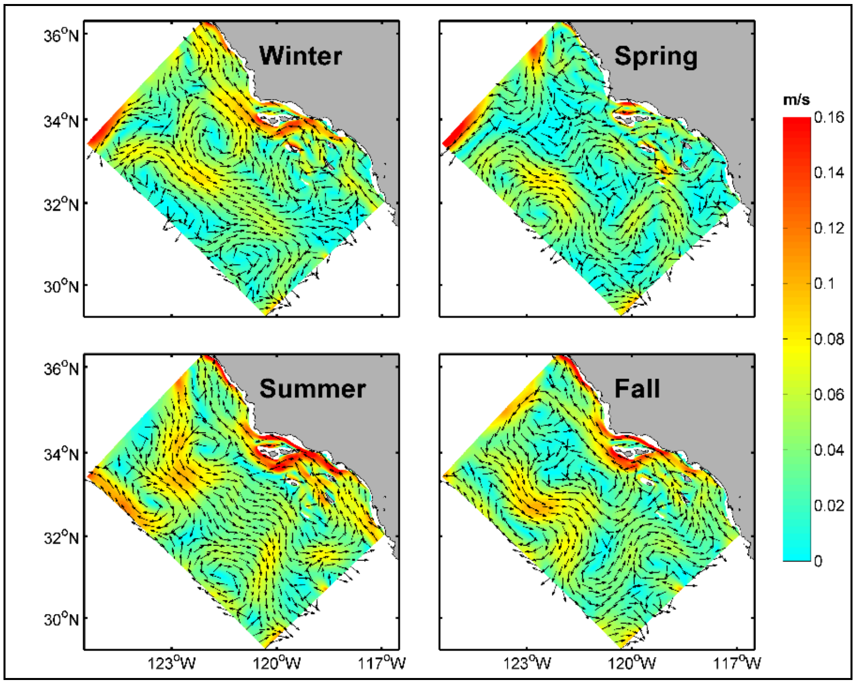

Figure 34. Same as Figure 33, but for 100 m.

No significant seasonality is found in the current velocity at 200 m (Figure 35) (Hickey, 1979, Auad et al., 2011). In summer, the alongshore current is strongest, with a maximum of about 0.08 m s^{-1}.

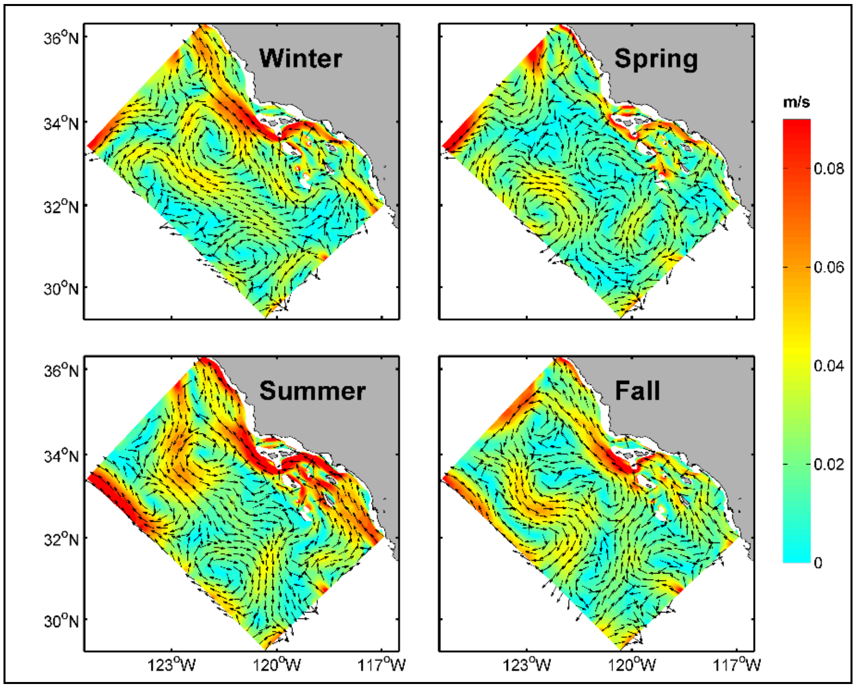

Figure 35. Same as Figure 33, but for 200 m.

5.3 Validation of tides

The tidal forcing is obtained from a global inverse barotropic tidal model (TPX07), which has a horizontal resolution of 0.25 °and applies an inverse modeling technique to assimilate satellite altimetry crossover observations. Eight major tide constituents of diurnal and semidiurnal frequencies (M2, K1, O1, S2, P1, N2, K2, Q1) are used to design the boundary condition. Six tidal gauges located in SCB are compared with the ROMS output. Note that due to model resolution, the tidal gauge San Diego (ID: 9410170), which is located in the Bay of San Diego, is not simulated by ROMS. The following six tidal gauges are used: Port San Luis (ID: 9412110), oil platform Harvest (ID: 9411406), Santa Barbara (ID: 9411340), Santa Monica (ID: 9410840), Los Angeles (ID: 9410660), and La Jolla (ID: 9410230). T_TIDE package (Pawlowicz et al., 2002) is used for the tidal harmonic analysis. The software performs a least-square fit to tidal constituents with certain frequencies.

Figure 36 shows the amplitudes and phases of SSH for the M2 and K1 constituents in the SCB. It is observed that both the M2 and K1 amplitudes amplify towards the coast and both the M2 and K1 phases show increasing trend with the increasing latitudes.

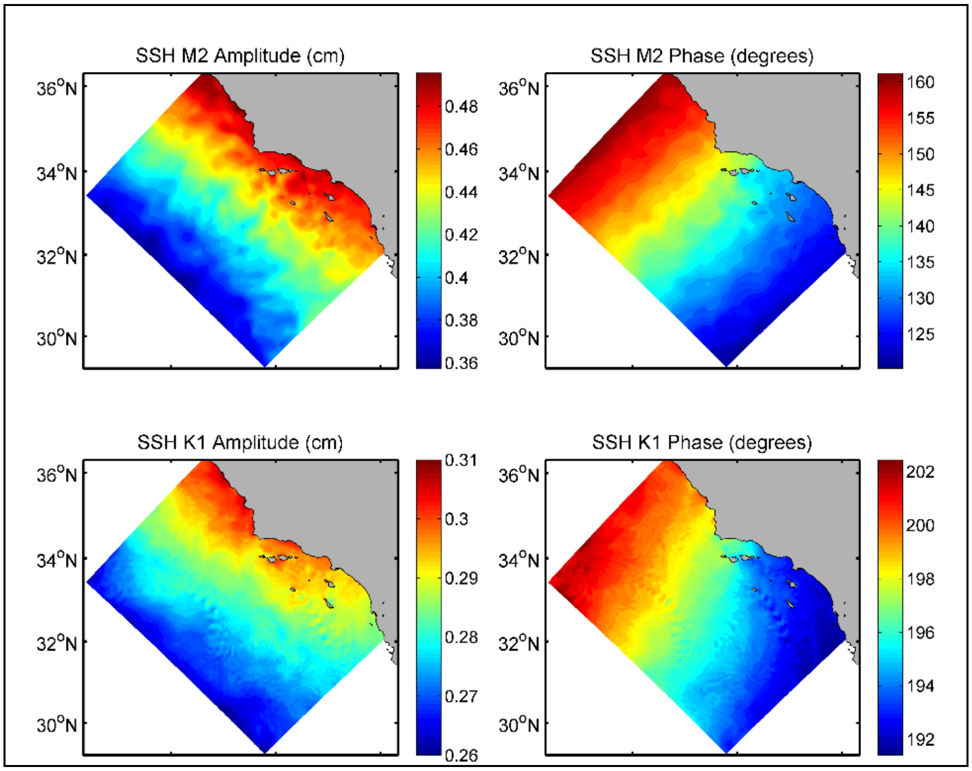

Figure 36. ROMS simulated amplitude and phase of SSH for the M2 (upper panels) and K1 (lower panels) constituents.

Figure 37 compares water level derived from observations and ROMS output for January 2006. It shows that the simulated SSH correlates well with observations, with correlation coefficients exceeding 0.95. Moreover, the correlation coefficients in the whole period (2004-2014) for the six tidal stations all exceed 0.96 (Table 7), which implies that the ROMS model can simulate both the short-time scale tide variation (including semidiurnal, diurnal, spring-neap constituents) and the long-time scale tide variation (such as the annual variation).

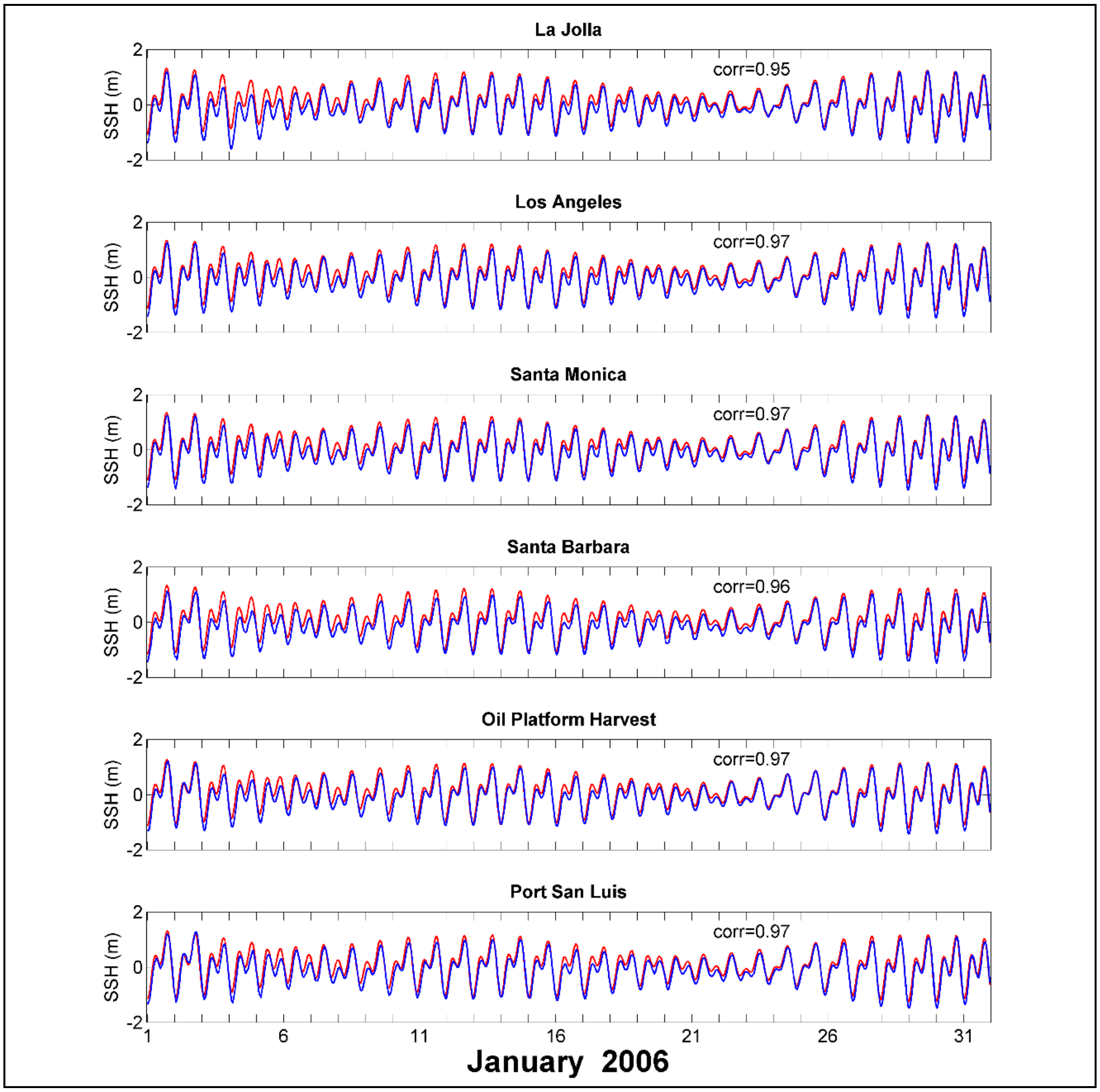

Figure 37. Observed and simulated SSH at six tidal gauge locations. Blue and red lines represent the observations and ROMS output, respectively.

Table 7. Correlation coefficients between tidal and modeled water levels

Location	Time	Location	Correlation Coefficients
Port San Luis, CA - Station ID: 9412110	2004–2013	(35.17° N, 120.75° W)	0.960
Oil Platform Harvest, Oil Platform Harvest - Station ID: 9411406	2004–2013	(34.47° N, 120.67° W)	0.960
Santa Barbara, CA - Station ID: 9411340	2005–2013	(34.40° N, 119.69° W)	0.963
Santa Monica, CA - Station ID: 9410840	2004–2013	(34.00° N, 118.50° W)	0.967
Los Angeles, CA - Station ID: 9410660	2004–2013	(33.72° N, 118.27° W)	0.967
La Jolla, CA - Station ID: 9410230	2004–2013	(32.87° N, 117.26° W)	0.963

Figure 38 compares the tidal amplitudes between ROMS output and tidal gauge observations. It shows that M2 and K1 are the most significant constituents in the SCB, with the amplitude of M2 and K1 reaching 50 and about 35 cm, respectively.

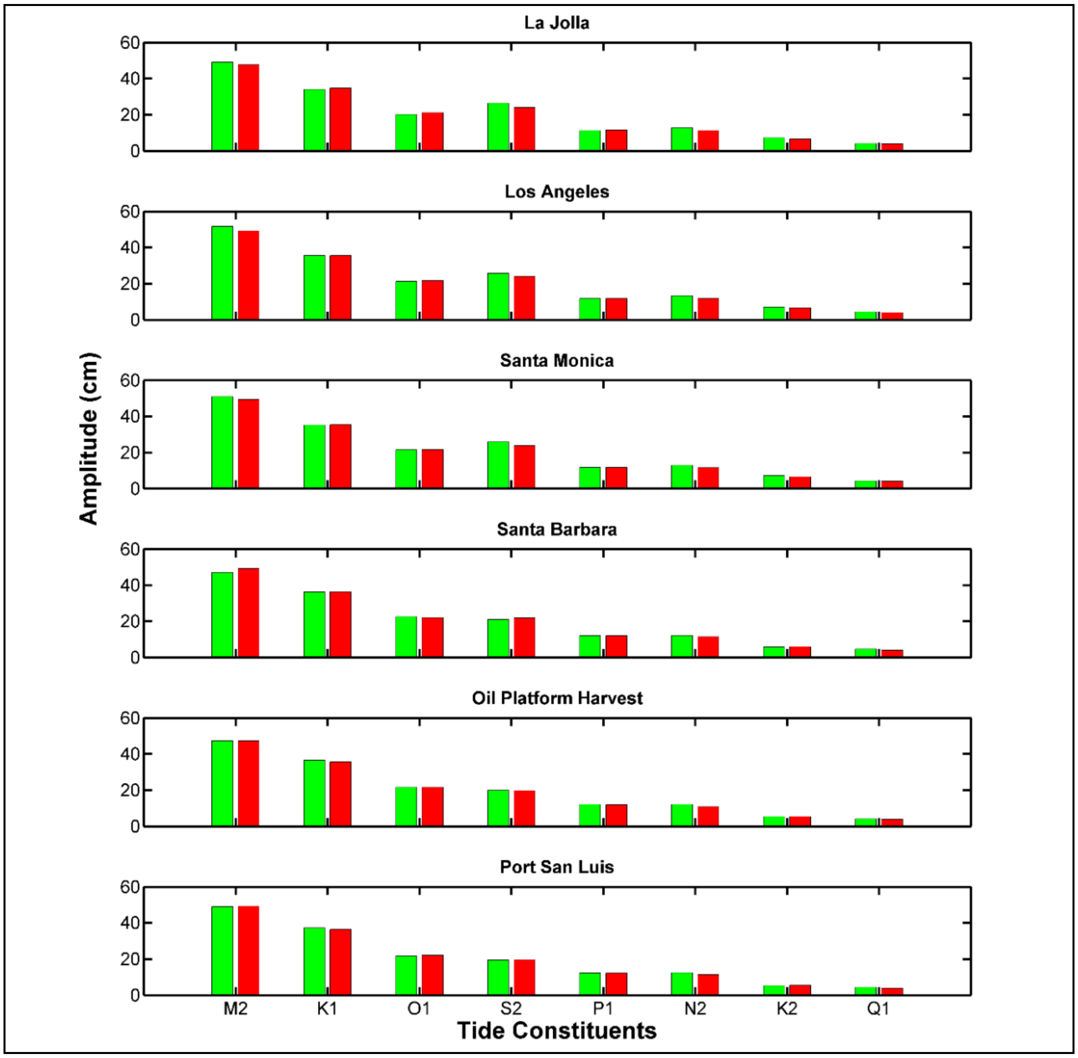

Figure 38. ROMS-derived and the tidal gauge-derived tidal amplitudes at the six tidal gauge locations and for eight tidal frequencies.

Green and red bars represent ROMS output and observations, respectively.

Figure 39 compares the tidal phases between ROMS output and tidal gauge observations. The phases of the constituents are all larger than 150 °. P1 has the maximum phase, and N2 exhibits the minimum.

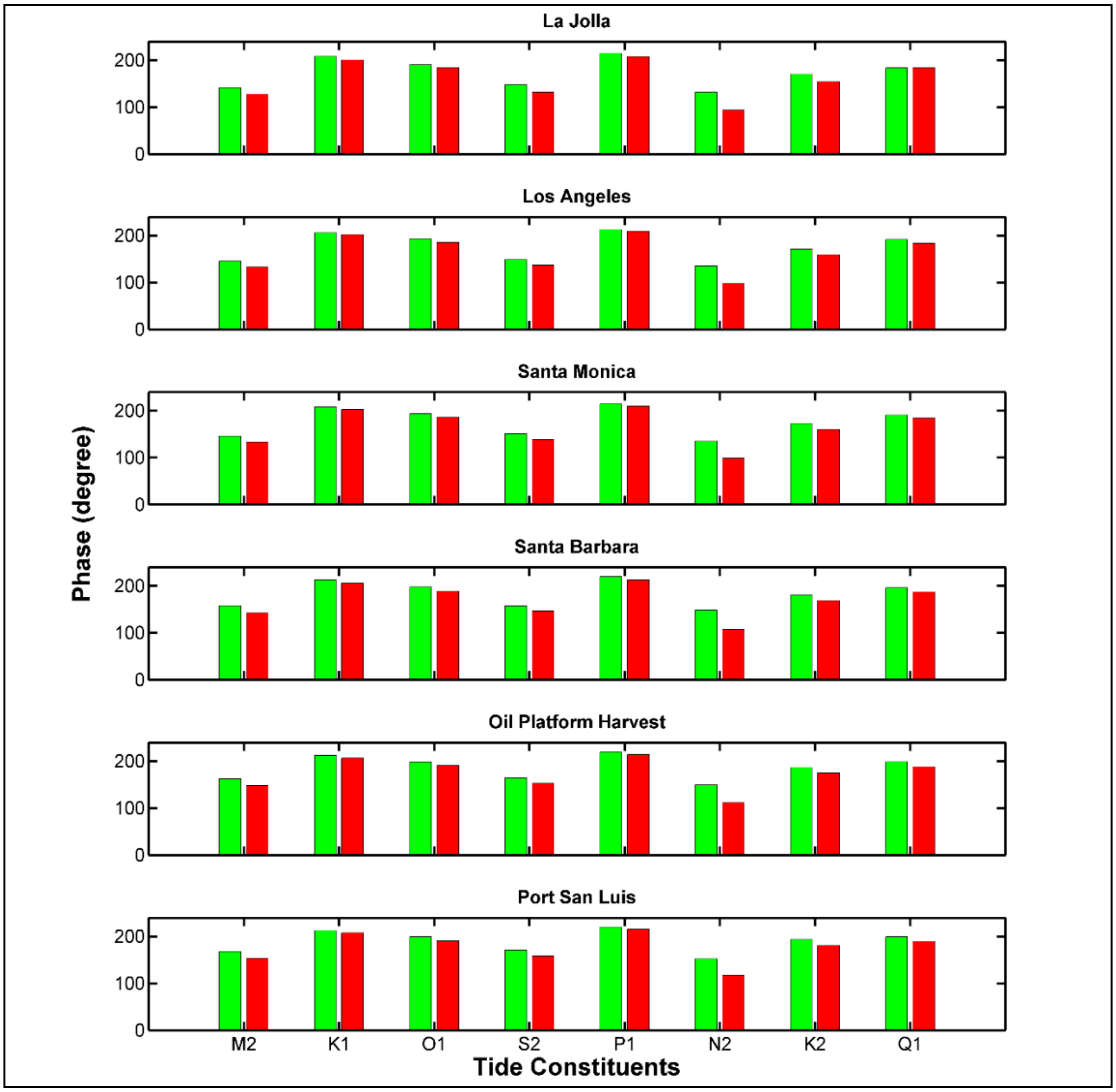

Figure 39. ROMS-derived and tidal gauge-derived tidal phases at the six tidal gauge locations and for eight tidal frequencies.

Blue and red bars represent ROMS output and observations, respectively.

Figure 40 shows the root mean square error (RMSE) of tidal amplitude and phase between six tidal gauge observations and ROMS output. The discrepancies between observed and model simulated amplitudes of eight tide constituents vary from 1.59 cm for M2 to 0.41 cm for K2 (upper panel in Figure 40).

The lower panel in Figure 40 shows that the phase discrepancy between ROMS output and tidal gauge observations is generally less than 14 °. The higher accuracy of the tidal solution in the model domain is associated with the better representation of coastal geometry and bottom bathymetry on the refined grid. The RMSE of the eight constituents' amplitudes and phases at the six tidal gauge locations is summarized in Table 8. Note that the maximum deviation (37.6 °) occurs at N2.

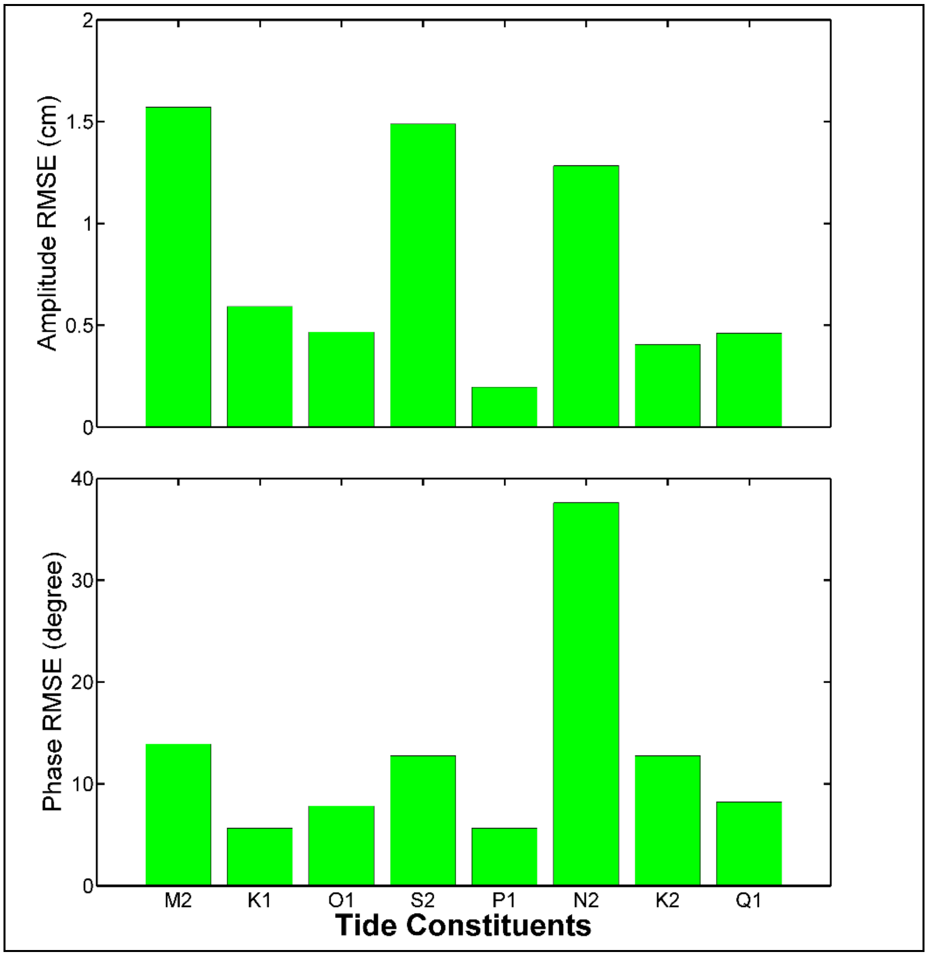

Figure 40. The RMSE of tidal amplitude and phase between six tidal gauges and ROMS output.

Table 8. RMSE of eight constituents' amplitudes and phases at six tidal gauge locations

Tide name	Amplitudes RMSE (cm)	Phase RMSE (degree)
M2	1.57	13.91
K1	0.59	5.63
O1	0.47	7.83
S2	1.49	12.76
P1	0.20	5.63
N2	1.28	37.58
K2	0.41	12.76
Q1	0.46	8.23

5.4 Validation of sea levels

Jason-1 SSH data are used to assess the low-frequency variability in the model simulation. Only five tracks pass through the SCB model domain (Figure 41), labeled as Passes 043, 119, 130, 206 and 221. The data sparseness explains why we prefer not to compare it with one of the gridded altimeter products. SSH anomalies along the five tracks from both Jason-1 observations and ROMS output are plotted in Figure 42- Figure 46. SSH anomalies from Jason-1 observations and ROMS output are both 10-day anomalies relative to 2004–2013 mean. There are evident interannual events that are coherent between the different tracks, in line with Bromirski et al. (2011) and, in most cases, between Jason-1 and ROMS data. The ROMS data has slightly larger anomalies than the Jason-1 data.

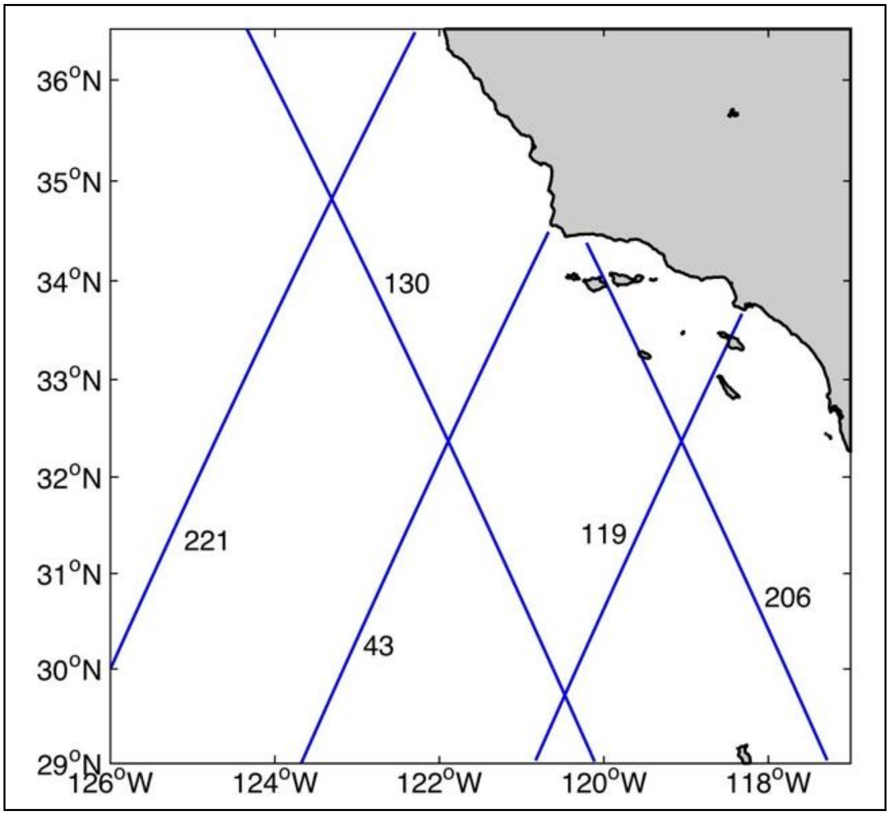

Figure 41. Jason-1 satellite tracks over the SCB.

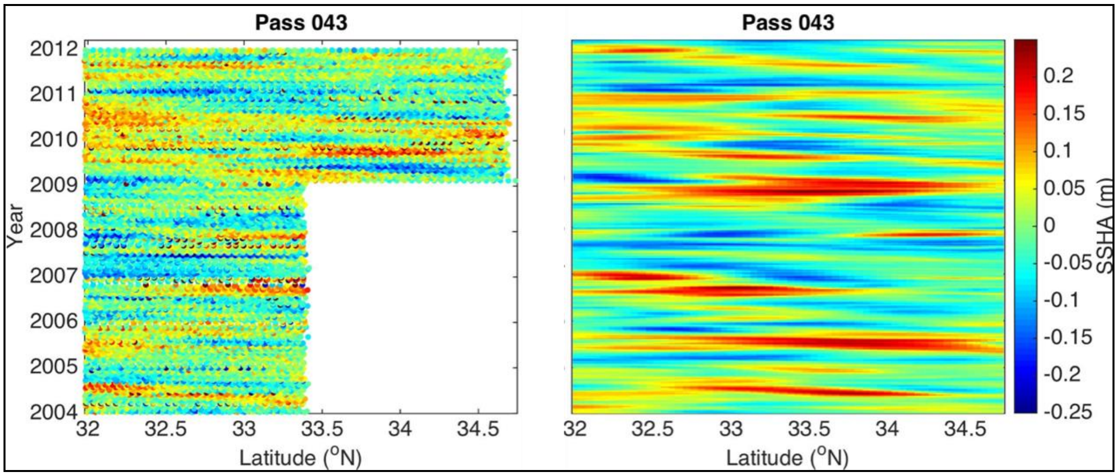

Figure 42. Along-track SSH anomalies (m) of Pass 043 from Jason-1 satellite (left) and ROMS data (right).

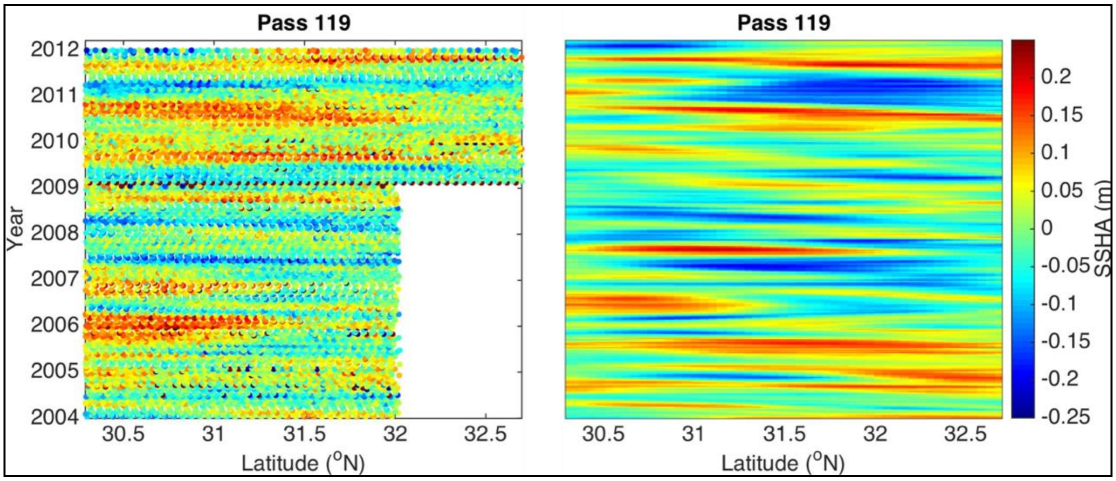

Figure 43. Along-track SSH anomalies (m) of Pass 119 from Jason-1 satellite (left) and ROMS data (right).

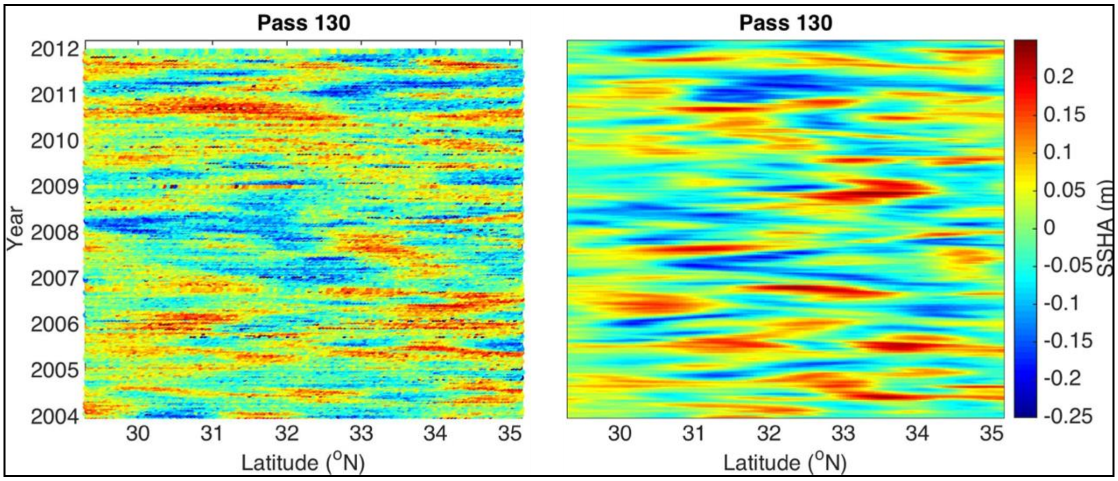

Figure 44. Along-track SSH anomalies (m) of Pass 130 from Jason-1 satellite (left) and ROMS data (right).

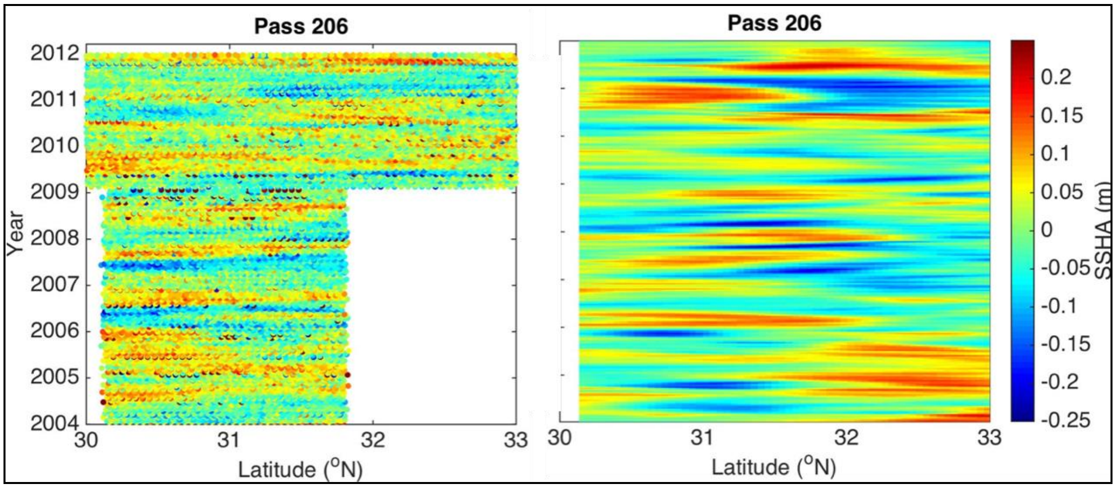

Figure 45. Along-track SSH anomalies (m) of Pass 206 from Jason-1 satellite (left) and ROMS data (right).

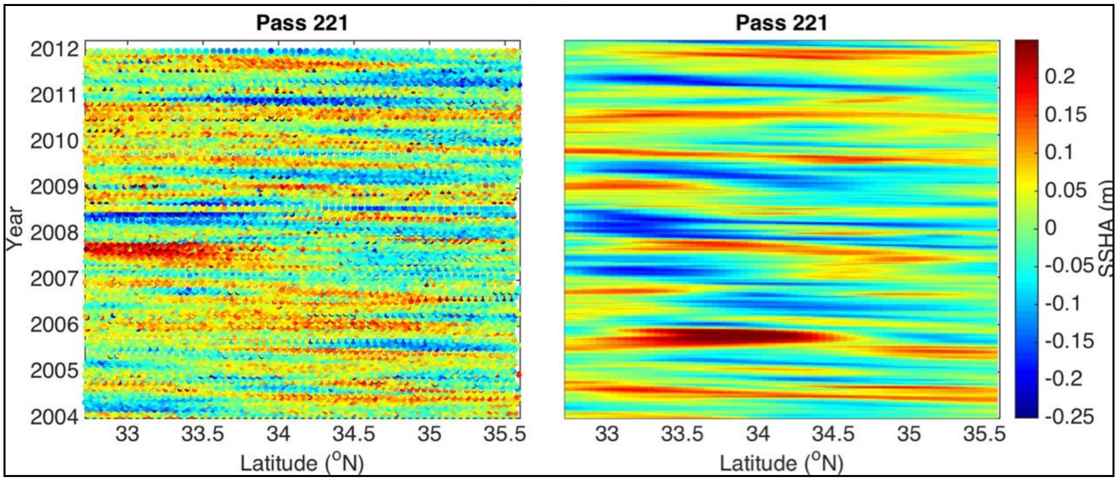

Figure 46. Along-track SSH anomalies (m) of Pass 221 from Jason-1 satellite (left) and ROMS data (right).

5.5 Validation of temperature and salinity

5.5.1 Sea surface temperature and salinity

Figure 47 shows the 10-year (2004–2013) mean SST from Advanced Very High Resolution Radiometer (AVHRR) (Cracknell, 1997) and ROMS data. The ROMS simulation agrees with the SST observations well in both magnitude and spatial pattern. SST decrease from the south to the north with the isothermals bending to the south. The coolest SST is observed along the northern coast of the study domain while the southern coast displays warm SSTs.

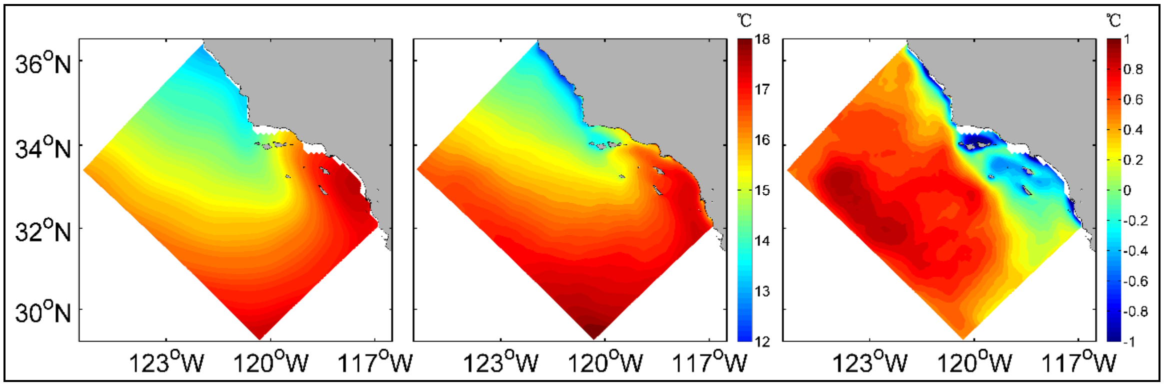

Figure 47. 10-year mean SSTs (units: °C) from AVHRR (left), ROMS output (middle), and their difference (right).

Figure 48 shows that the seasonal mean SSTs from observation and model and their differences. The seasonal cycle with warming in summer and cooling in winter is obvious both in the observation and model. In summer, due to the strong southern California Countercurrent, the temperature is highest (nearly 20 ℃) around the southern Channel Islands. In winter, the cold current of California Current is stronger, which leads to the coldest water in the SCB. The SST in the model is systematically warmer along the shore and colder west of that. The largest deviation locates in the SBC, especially in summer, which is about 2.5 ℃ warmer in the model.

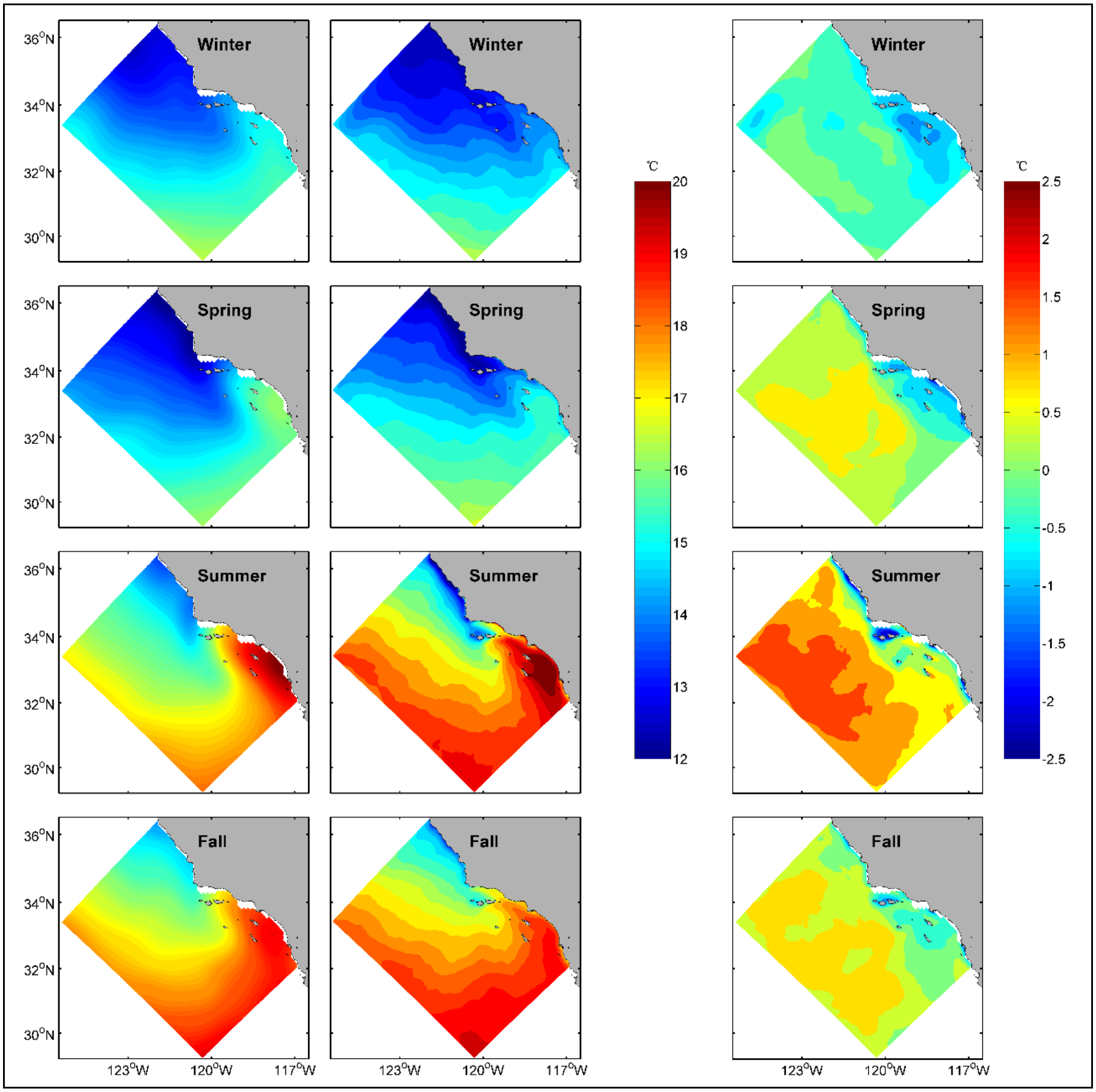

Figure 48. Seasonal mean SSTs (units: °C) from AVHRR (left), ROMS output (middle) and their difference (right).

From top to bottom are winter, spring, summer and fall.

Figure 49 shows that the pattern of mean salinity from ROMS output is similar to that of Aquarius (Springel et al., 2008). The salinity from ROMS is lower in the northwest than along the coast. Comparatively, the salinity from Aquarius is lower in the northwest with the value of about 33.1 PSU, similar to the salinity observed from ROMS output. However, Aquarius exhibited high values of about 34 PSU in the southeast, higher than the salinity from ROMS output over the same location. The coastal area salinities from ROMS output and Aquarius observations are different.

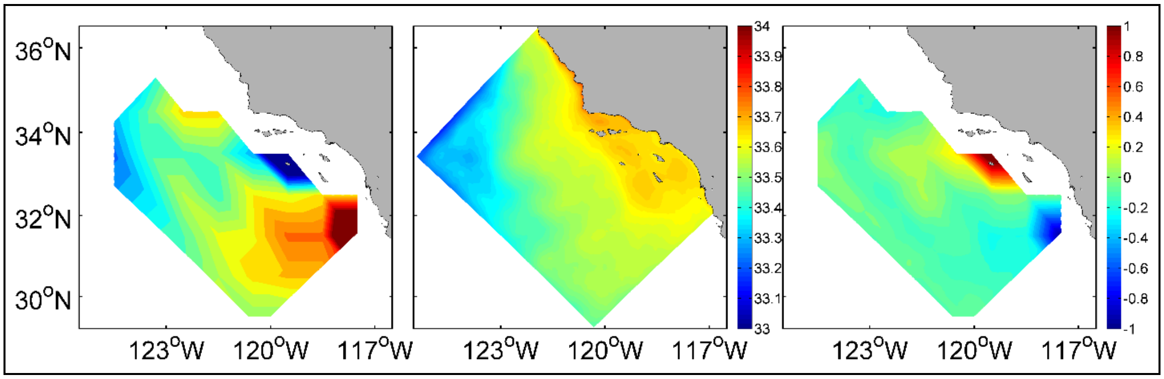

Figure 49. 10-year mean sea surface salinities (units: PSU) from Aquarius (left), ROMS output (middle) and their difference (right).

Figure 50 shows the seasonal mean salinity from Aquarius. It is noted that in all four seasons, the salinity is higher in the southeast and lower in the northwest of the domain. The asymmetry between the southern and northern parts is clearest in winter. The salinity in ROMS is also higher in the southeast and lower in the northwest, which is consistent with the Aquarius observations. The asymmetry between the southern and northern parts in winter is also reproduced by ROMS. However, the maximum salinity is lower in ROMS output than in Aquarius observations.

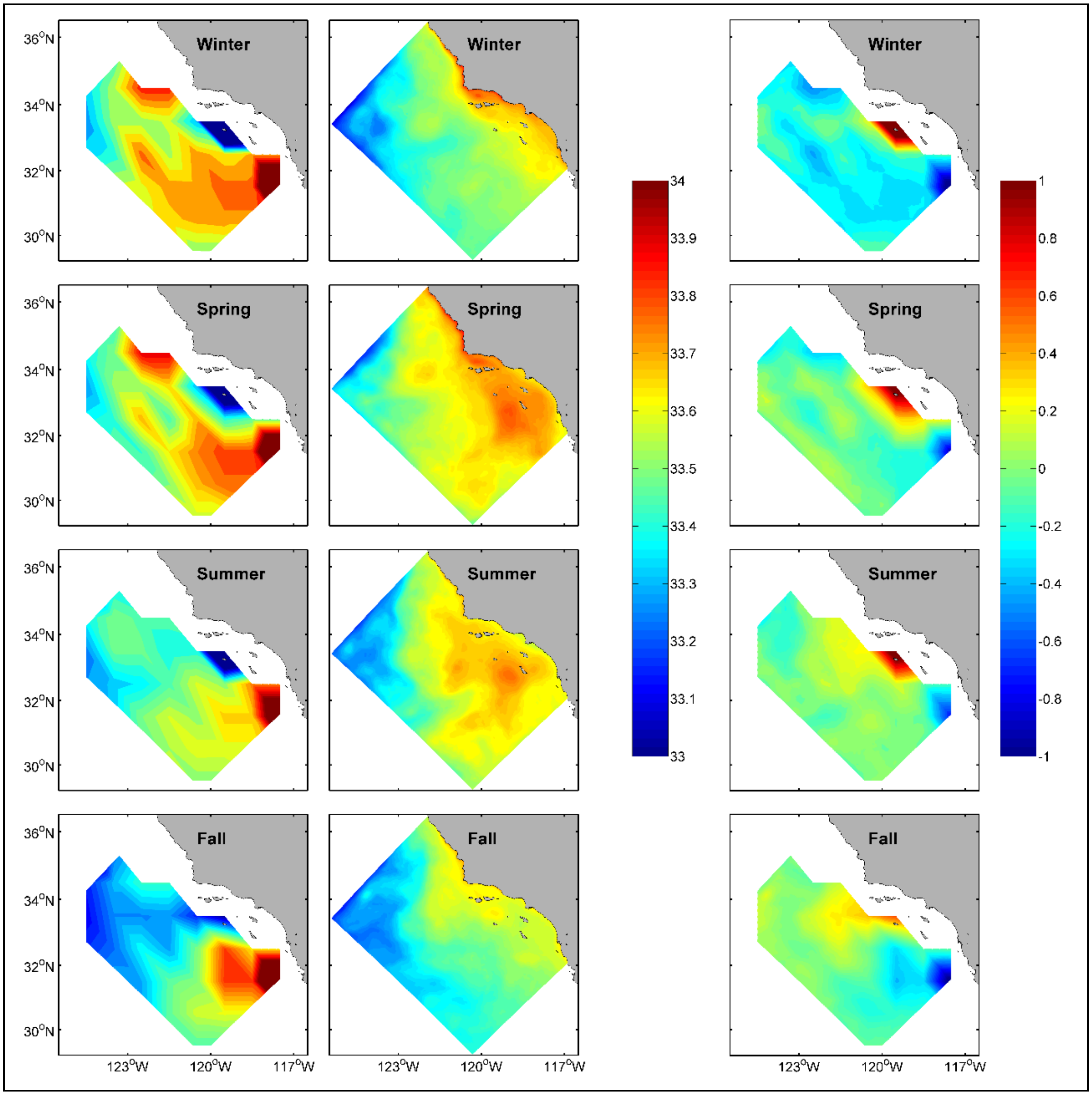

Figure 50. 10-year mean sea surface salinities (units: PSU) from Aquarius (left), ROMS output (middle) and their difference (right).

From top to bottom are winter, spring, summer and fall.

5.5.2 Buoy observations

Figure 51 and Figure 52 show the relationship between buoy observations and ROMS simulated salinity and temperature at buoy stations 46053 and 46063, respectively. In general, the variations of salinity and temperature are well reproduced by the ROMS, including the temperature increase and the salinity decrease in summer of June 2007.

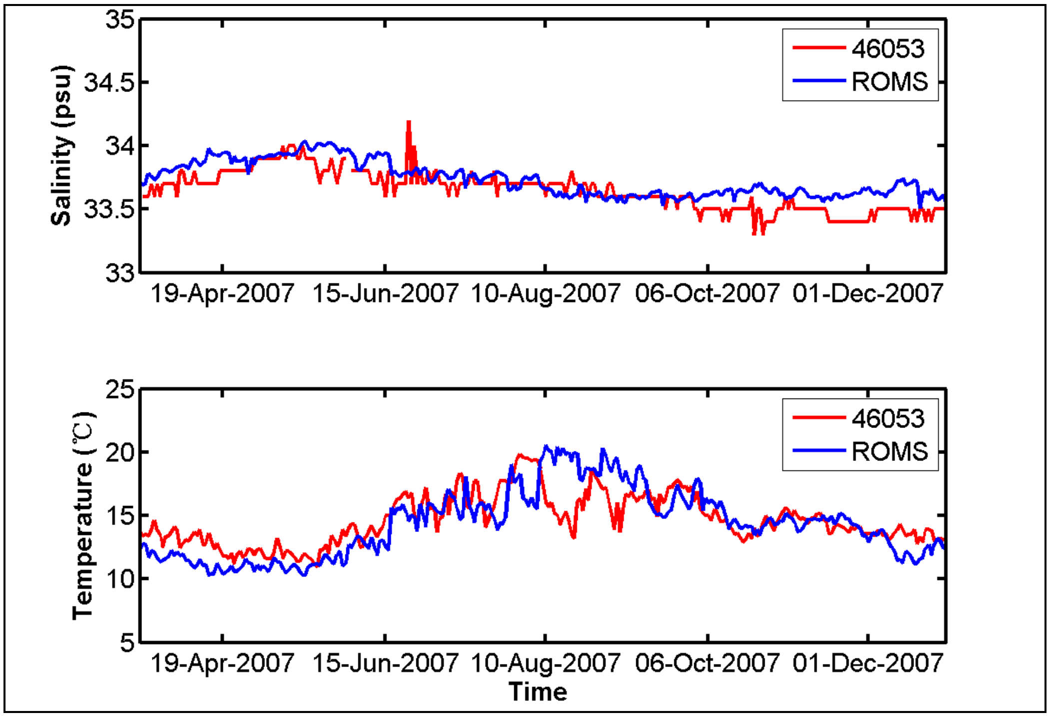

Figure 51. Time series of salinity (top) and temperature (bottom) from buoy station 46053 and ROMS output.

The red and blue lines represent buoy observations and ROMS output, respectively.

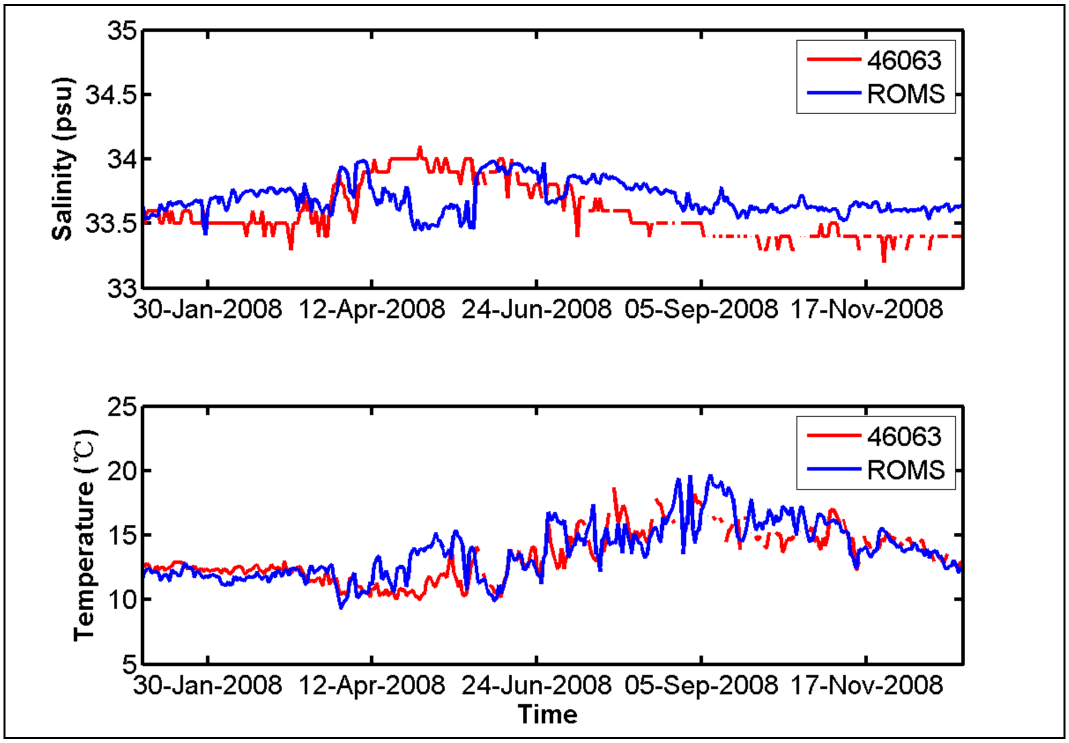

Figure 52. Same as Figure 51, but for the buoy station 46063.

5.5.3 CalCOFI

Figure 53 through Figure 58 show the cross-sections of seasonal mean temperature and salinity along CalCOFI Cruise lines and ROMS output in winter and summer. Figure 53 shows that the thermocline layer in summer is shallower and the isopycnal slopes are steeper than in winter. The uplift of the thermohaline near the middle of the cruise line shows the Central-SCB Eddy. The magnitudes and structural patterns of temperature and salinity from ROMS output and CalCOFI Cruise lines data agree fairly well with each other. Furthermore, the vertical gradients within the top 100 m are slightly stronger in the model.

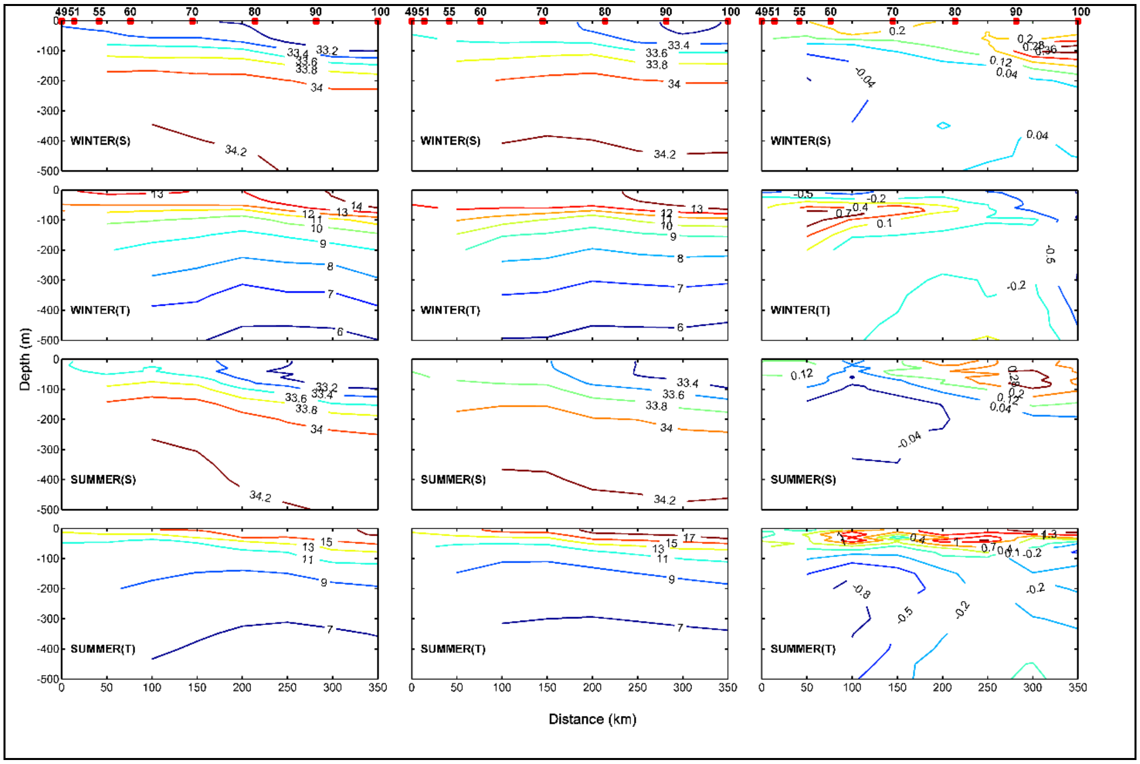

Figure 53. Cross-sections of seasonal mean temperature and salinity along Line 76.7 from CalCOFI (left panels), ROMS output (middle panels) and their difference (right panels) during winter and summer over 10 years (2004–2013).

From top to bottom: seasonal mean salinity in winter, seasonal mean temperature in winter, seasonal mean salinity in summer, and seasonal mean temperature in summer. The ordinate represents the depth and the abscissa represents the distance from the beginning point of a track in the domain. See Figure.

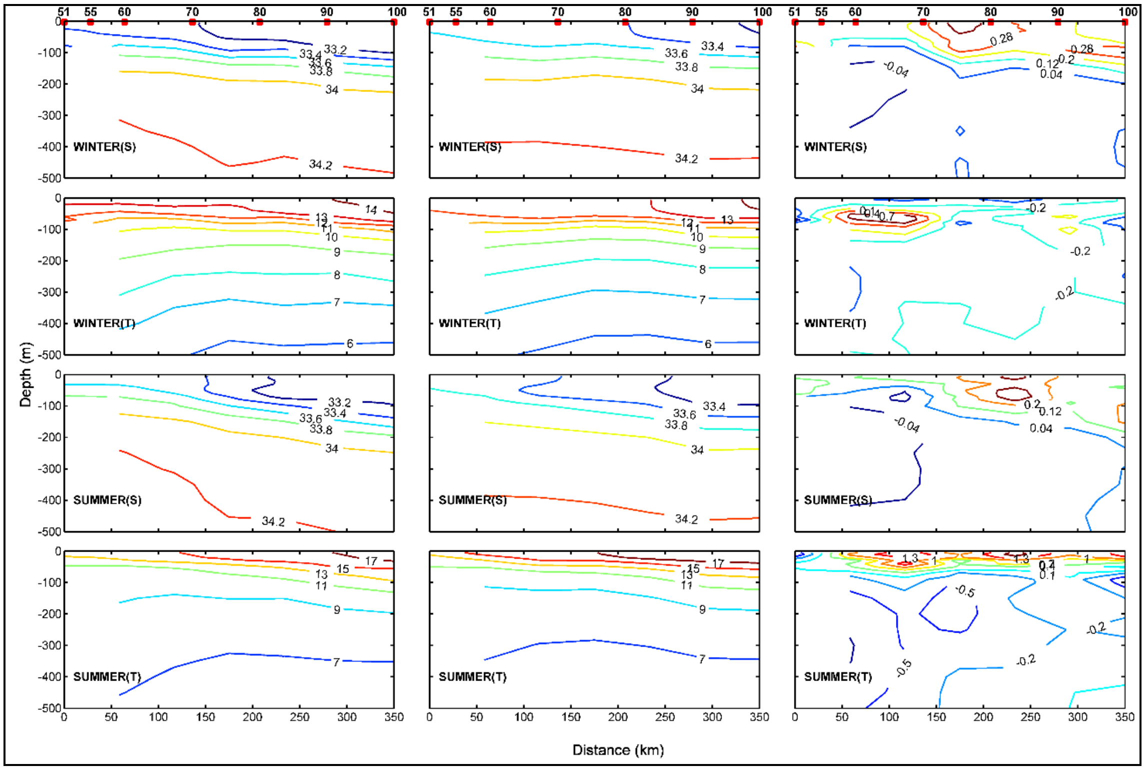

Figure 54. Same as Figure 53, but for Line 80.

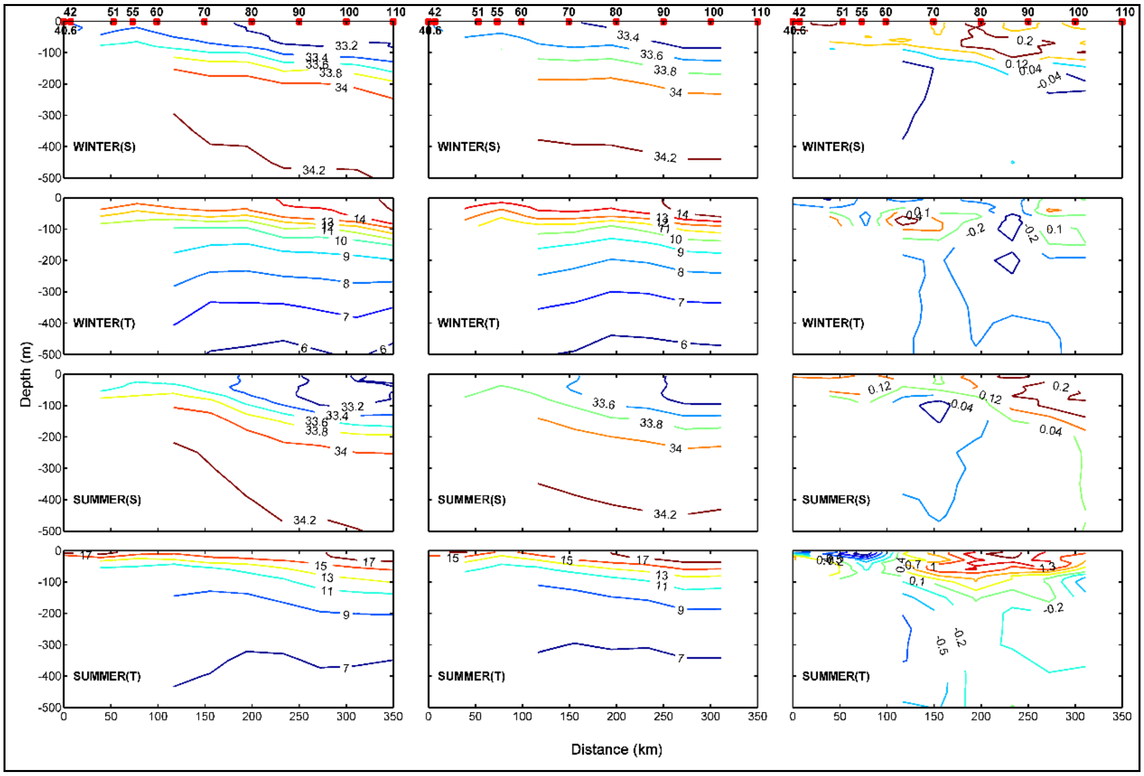

Figure 55. Same as Figure 53, but for Line 83.3.

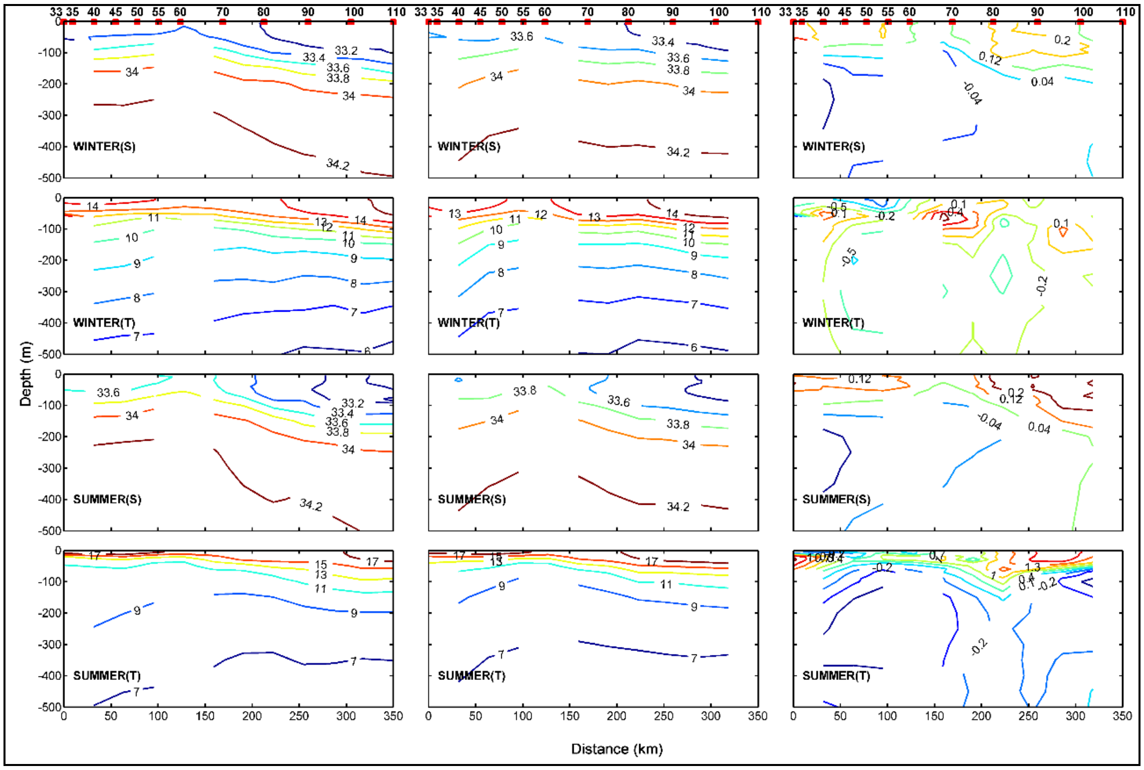

Figure 56. Same as Figure 53, but for Line 86.7.

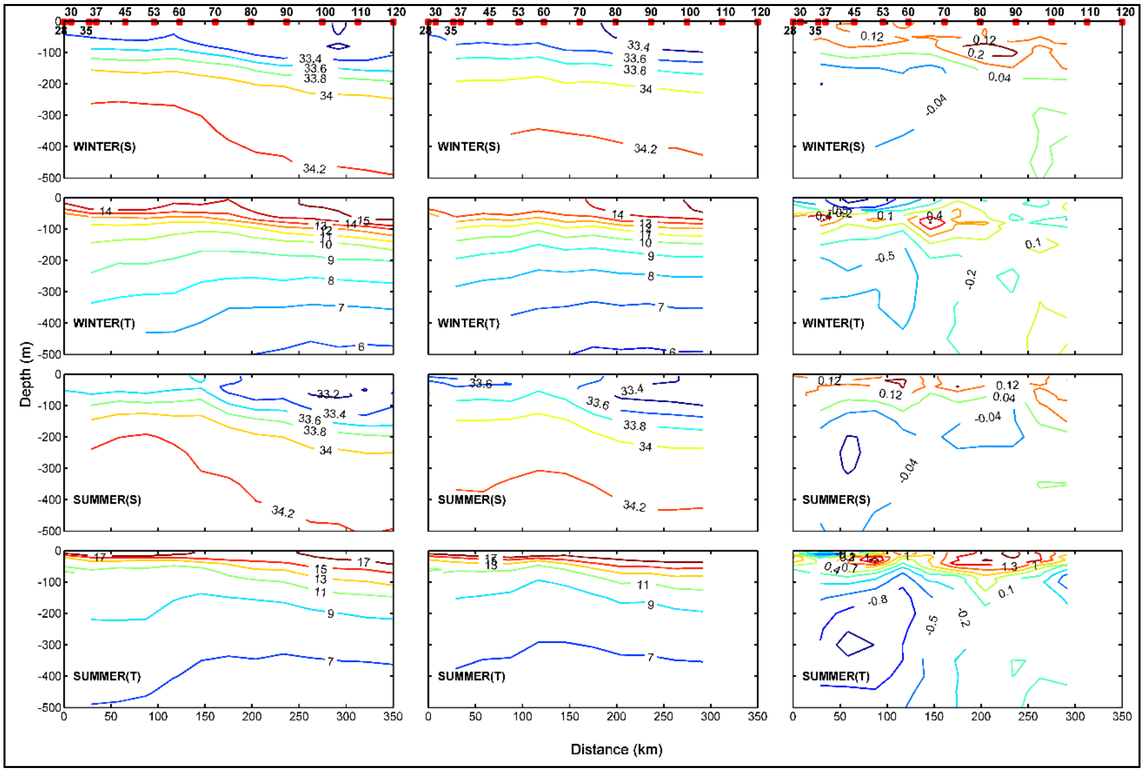

Figure 57. Same as Figure 53, but for Line 90.

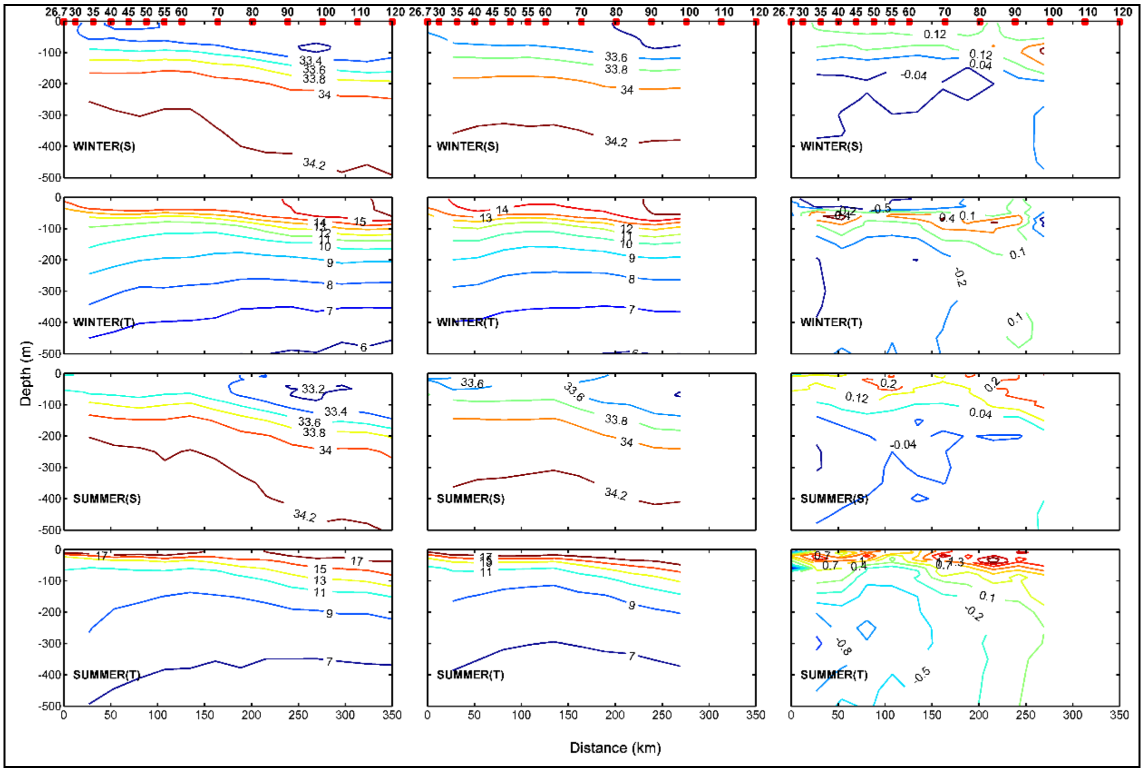

Figure 58. Same as Figure 53, but for Line 93.3.

5.6 Validation of currents

5.6.1 HF Radar

Figure 59 shows the surface currents in the SBC from HF radar observations and ROMS output. The results are observed to follow similar patterns. The largest velocity occurs in summer and a cyclonic eddy exists year-round over the western SBC, from both data sources. Note that the flow direction over the western part of the domain is different between the two data sets in winter.

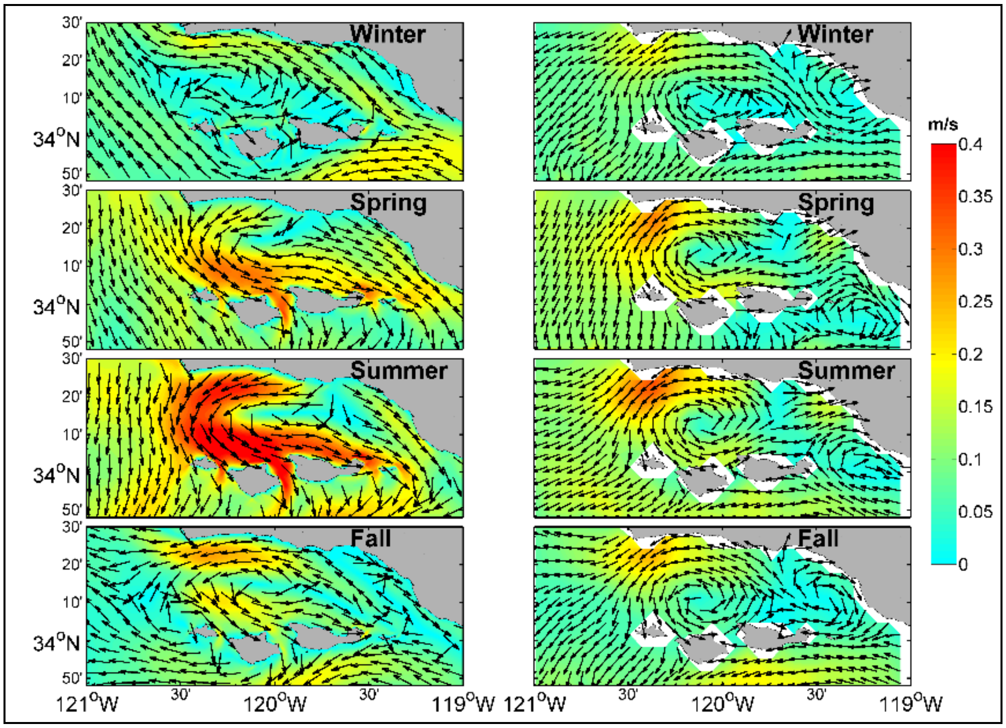

Figure 59. Seasonal mean surface current in the SB Channel from HF radar observations (left panel) and ROMS output (right panel) during the period 2011–2013.

5.6.2 Buoy observations

To further assess the ROMS simulation, the ROMS output velocity fields are compared with the ADCP buoy data. Figure 60 presents the vertical profiles of horizontal velocity components. Generally, both the ROMS simulation and observations display similar mean profiles and range of variation at the three stations. It is also shown that the horizontal current components in the deeper layers are better simulated than at the surface. The standard deviation of the ROMS output and ADCP data is similar.

Table 9 summarizes the mean and RMSE of the horizontal current velocity from buoy observations and ROMS output at each buoy station. The RMSE is on the order of tens of cm s^{-1}.

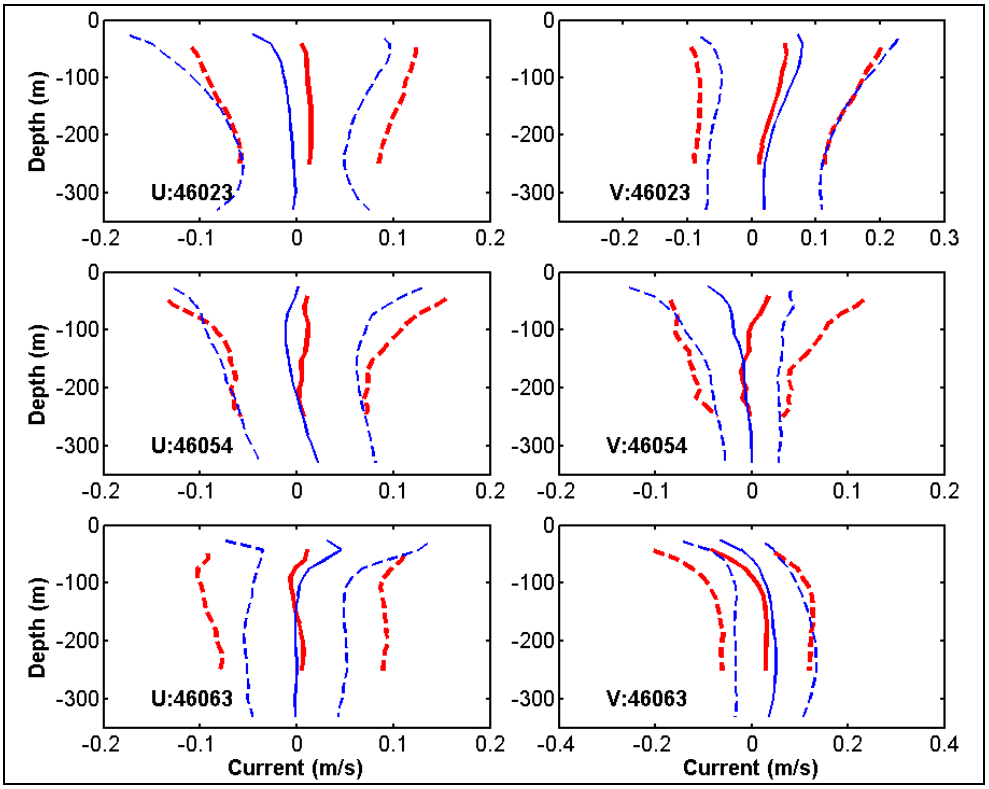

Figure 60. Vertical profiles of zonal (left panels) and meridional (right panels) velocity from ADCP measurements at buoy stations 46023 (top), 46054 (middle), and 46063 (bottom) from observations (red lines) and ROMS output (blue lines) over 2004–2005, 2004–2005 and 2006–2009 periods, respectively.

Solid lines are the time averages, and the two dashed lines are separated from the solid line by one standard deviation

Table 9. Time mean and RMSE of horizontal current velocity (units: m s^{-1}) from observations and ROMS output at each buoy station (umean: mean of zonal current; vmean: mean of zonal current)

Station	Time	obs u_{mean}	obs v_{mean}	ROMS u_{mean}	ROMS v_{mean}	u RMSE	v RMSE
46011	2005	0.0239	0.0041	0.0028	0.0612	0.0983	0.1021
46011	2006	0.0152	0.0093	-0.0101	0.0789	0.1147	0.1467
46011	2007	0.0227	-0.0427	0.0118	-0.0126	0.1083	0.1346
46011	2008	0.0187	-0.0541	0.0524	0.0292	0.1286	0.1478
46023	2004	0.0134	0.0222	-0.0107	0.0427	0.1039	0.1244
46023	2005	-0.0037	-0.0206	-0.0231	0.0260	0.0980	0.1267
46047	2011	0.0384	-0.0520	0.0528	-0.0673	0.1136	0.1061
46053	2007	-0.0106	0.0151	-0.0164	0.0217	0.0826	0.1059
46054	2004	0.0021	0.0078	0.0003	-0.0144	0.1490	0.1011

Station	Time	obs u_{mean}	obs v_{mean}	ROMS u_{mean}	ROMS v_{mean}	u RMSE	v RMSE
46054	2005	-0.0090	0.0053	-0.0002	-0.0118	0.1158	0.0723
46063	2006	-0.0172	-0.0016	-0.0492	0.0641	0.1036	0.1023
46063	2007	0.0015	0.0072	0.0053	0.0298	0.1053	0.1365
46063	2008	-0.0126	-0.0171	-0.0259	0.0329	0.1196	0.1445
46063	2009	0.0055	-0.0371	0.0026	0.0374	0.1089	0.1212
46233	2007	0.0360	-0.0655	0.0120	-0.0701	0.0992	0.1839

6. Validation of the SWAN Simulation

6.1 Observational data

The monthly mean significant wave height (SWH) altimeter data with horizontal resolution of 2×2 are taken from L'Institut Français de Recherche pour l'Exploitation de la Mer (IFREMER; *French Research Institute for Exploitation of the Sea*). Altimeter SWH measurements are presently available almost continuously over a 23-year time period from the nine altimeter missions ERS-1&2, TOPEX-Poseidon, GEOSAT Follow-ON (GFO), Jason-1, Jason-2, ENVISAT ("Environmental Satellite"), Cryosat, and SARAL ("Satellite with ARgos and ALtika"). Each altimeter data product has specific characteristics (format, flags), and in order to facilitate the access to SWH altimeter measurements and the use of this longtime series, data are extracted from the original products, screened according to quality flag values, corrected and gathered into homogeneous daily data files.

This study uses the hourly wave data from the NDBC over the California shelf from January 2004 to December 2013. Only stations carrying the long-term data (2004–2013) are selected. These stations are: #1 46011, #2 46025, #3 46028, #4 46047, #5 46053, #6 46054, #7 46069, #8 46086, #9 46215, #10 46216, #11 46217, #12 46218, #13 46224, and #14 46225. The buoys used in this study are summarized in Table 10 and their locations are shown in Figure.

Table 10. Buoy stations used for SWAN output validation

No.	Latitude (°N)	Longitude (°W)
46011	34.96	121.01
46025	33.74	119.05
46028	35.71	121.86
46042	36.79	122.45
46047	32.40	119.50
46053	34.25	119.85
46054	34.26	120.48
46069	33.64	120.21
46086	32.49	118.03
46215	35.02	120.86
46216	34.33	119.80
46217	34.17	119.43
46218	34.45	120.78
46224	33.18	117.47
46225	32.93	117.39

The European Centre for Medium- Range Weather Forecasts (ECMWF) is a comprehensive numerical modeling system with the data assimilation of the observational data. It provides a variety of products, among which, the sea surface wind and wave from ERA-Interim datasets are used in the present study. The ERA-Interim is based on a 2006 release of the Integrated Forecasting System (IFS) (Cy31r2). The number of observations assimilated in ERA-Interim has increased from approximately 106 per day on average in 1989, to nearly 107 per day in 2010. The overwhelming majority of data, and most of the increase over time, originate from satellites. This includes clear-sky radiance measurements (quantified as brightness temperatures) from polar-orbiting and geostationary sounders and imagers, atmospheric motion vectors derived from geostationary satellites, scatterometer wind data, and ozone retrievals from various satellite-borne sensors. Also derived from satellite observations are the total precipitable vapor estimates produced within the 1D+4D-Var scheme. Measurements of atmospheric refraction (quantified as bending angles) obtained from global positioning system (GPS) radio occultation began to be used in ERA-Interim in 2001, growing to significant numbers by the end of 2006. The conventional observing system, in spite of much lower data volumes, still serves as an indispensable constraint to the atmospheric reanalysis. In situ measurements of upper air temperatures (*T*), wind (*u/v*), and specific humidity (*q*) were available from radiosondes, pilot balloons, aircraft, and wind profilers. Data counts for these sources are more or less steady during the reanalysis period, with the exception of aircraft reports whose numbers increased greatly after 1998. Observations of surface pressure (*Ps*), 2 m temperature, 2 m relative humidity (*RH*), and near-surface (10 m) winds (*u/v*) from ships, drifting buoys, and land stations were also assimilated in steady numbers.

The dataset has a spatial resolution of 0.125˚×0.125˚ and a six-hourly temporal sampling frequency. The data within the period of 2004–2013 is used in this study.

6.2 Validation of SWH

The SWH is defined traditionally as the mean wave height (trough to crest) of the highest third of the waves ($H_{1/3}$). Nowadays, it is defined as four times the standard deviation of the surface elevation—or equivalently as four times the square root of the zeroth-order moment (area) of the wave spectrum (Holthuijsen, 2007). The symbol H_{m0} is usually used for that latter definition. The significant wave height may thus refer to H_{m0} or $H_{1/3}$ since the difference in magnitude between the two definitions is only a few percent.

Figure 61 presents the seasonal mean IFREMER SWH averaged from 2004 to 2013. In winter (Figure 61a), the SWH decreases from northwest to southeast; that is, the wave field shows a decreasing trend from offshore to nearshore. This may be related to the strong wind and strong swell in open sea. When it propagates to nearshore, the wave height becomes shorter, which is mainly due to the decreasing water depth. With the change in bathymetry, the bottom friction becomes larger and the wave energy consumption gradually increases resulting in smaller wave height.

The spatial patterns in spring, summer, and fall are similar to that of winter but with smaller magnitudes. The lowest SWH occurs in summer (Figure 61b). The seasonal SWH from ERA-Interim is shown in Figure 62. As the ERA-Interim data has a higher resolution, it shows a finer spatial pattern. Nevertheless, the primary feature is consistent with the altimeter result.

The SWAN simulation reproduces the SWH fairly well (Figure 63). The SWH pattern for each season resembles that from observations. The SWH near the shore is less than 1.5 m and becomes larger than 1.5 m in the open sea. Furthermore, the SWAN simulation shows the effect of the islands on the wave, which demonstrates the ability of SWAN in simulating the reflection and diffraction of the waves in the SCB region.

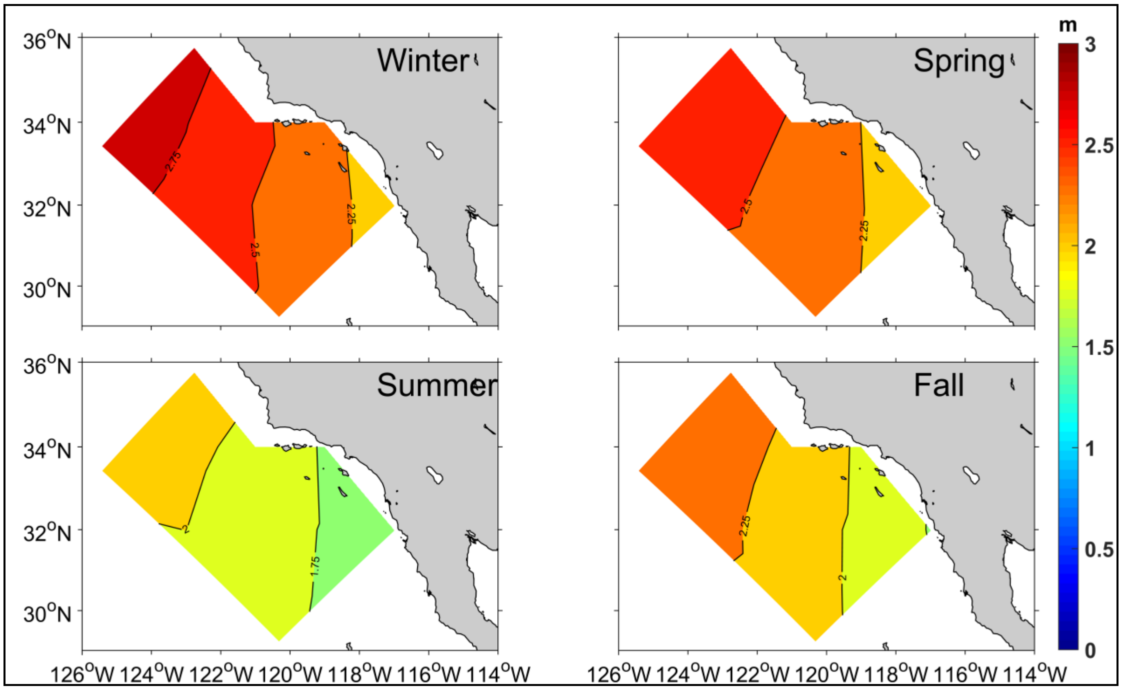

Figure 61. Seasonal SWH for altimeters (units: m) in (a) winter, (b) spring, (c) summer, and (d) fall.

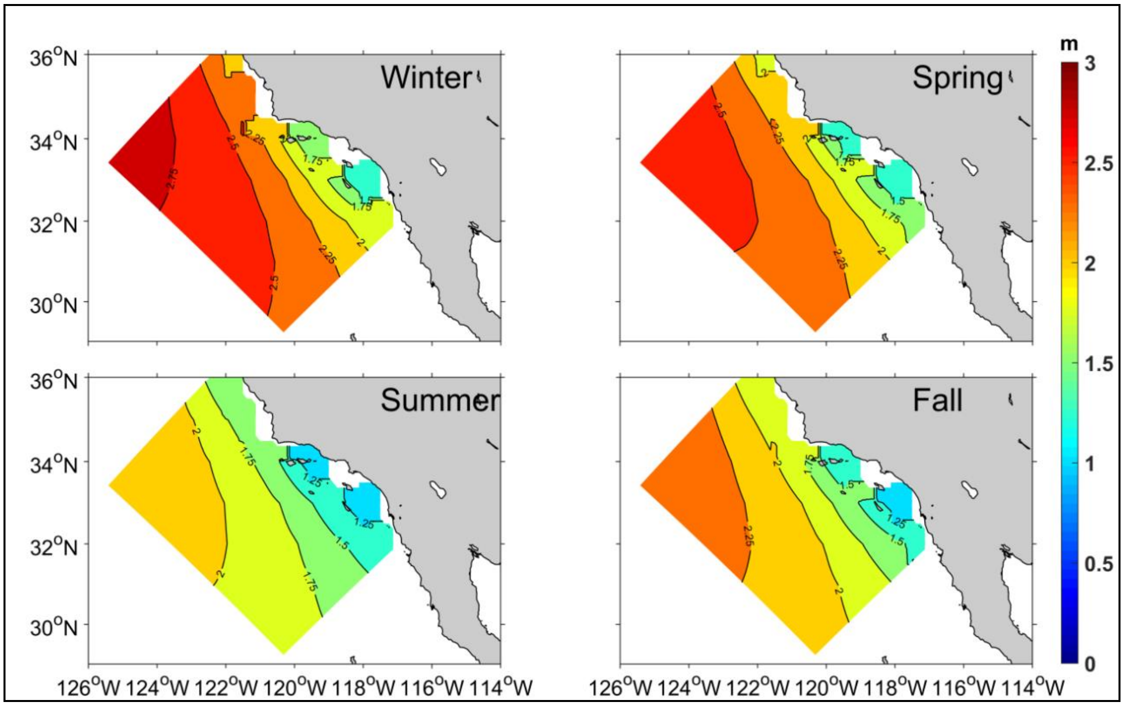

Figure 62. Same as Figure 61, but from ERA-Interim.

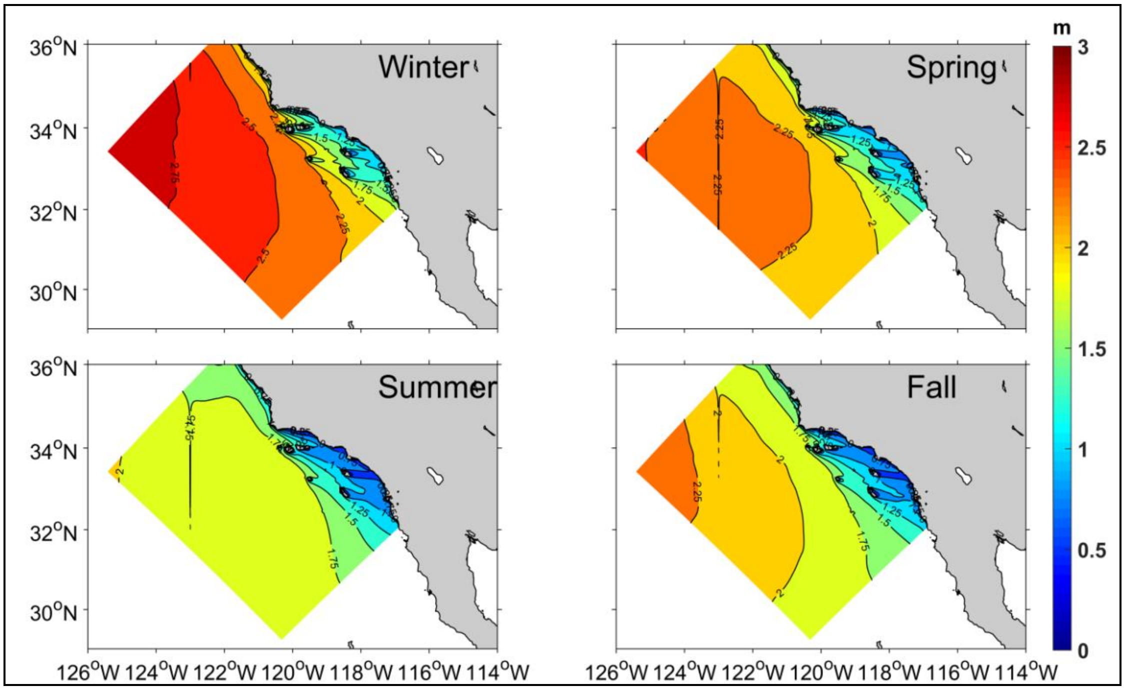

Figure 63. Same as Figure 61, but from SWAN.

Table 11 shows the correlation coefficients and the RMSE of the SWH between SWAN output and 15 buoy station data in 2004–2013. The simulated SWH is well correlated to the observed one, indicating the good performance of the SWAN model in the SWH simulation.

Table 11. Correlation coefficients and RMSE of SWH between SWAN output and data from 15 buoy stations in 2004–2013

	Station Number	Correlation coefficients	RMSE (m)
Buoy, SWAN	46011	0.82	0.39
	46025	0.85	0.29
	46028	0.80	0.50
	46042	0.68	0.60
	46047	0.89	0.34
	46053	0.83	0.34
	46054	0.83	0.38
	46069	0.91	0.34
	46086	0.89	0.34
	46215	0.72	0.56
	46216	0.65	0.52
	46217	0.68	0.45
	46218	0.70	0.60
	46224	0.73	0.38
	46225	0.73	0.38

Figure 64 through Figure 68 show the observed and SWAN simulated time series of hourly SWH in 2008. The correlation coefficients between the observations and simulations are high for stations 46028, 46047, 46053, 46069, 46216, 46217, and 46225.

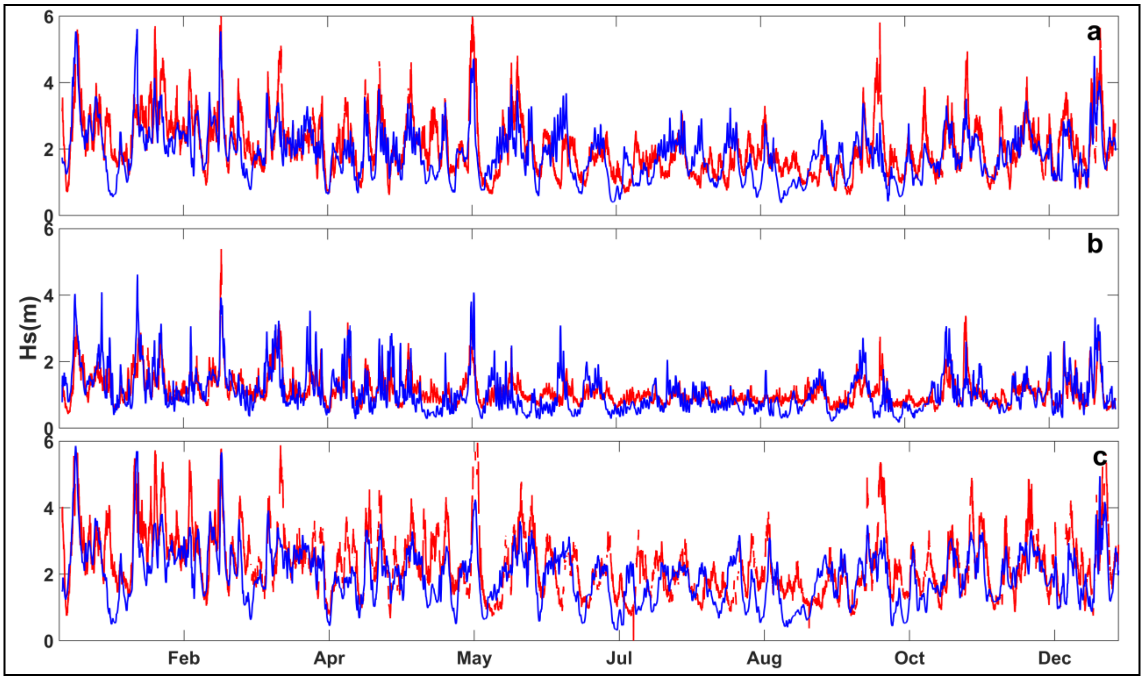

Figure 64. Comparison of the hourly SWH between SWAN output and in-situ data at station (a) 46011, (b) 46025, and (c) 46028 in 2008.

Red and blue lines represent the simulated results and observations, respectively.

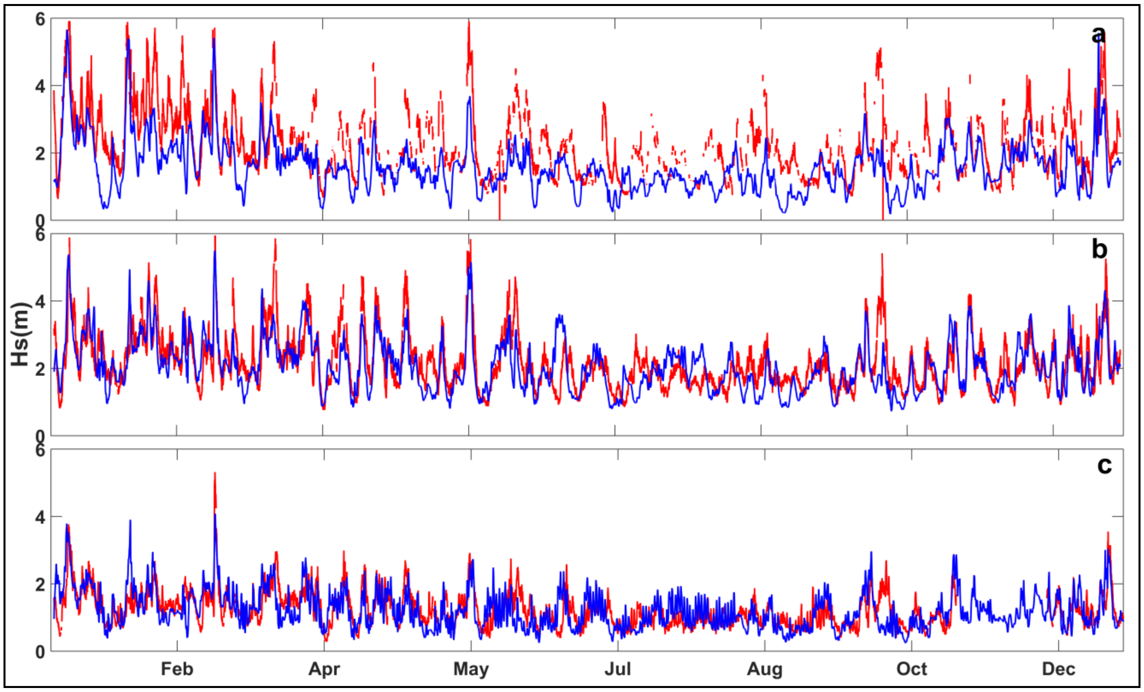

Figure 65. Same as Figure 64, but for station (a) 46042, (b) 46047, and (c) 46053.

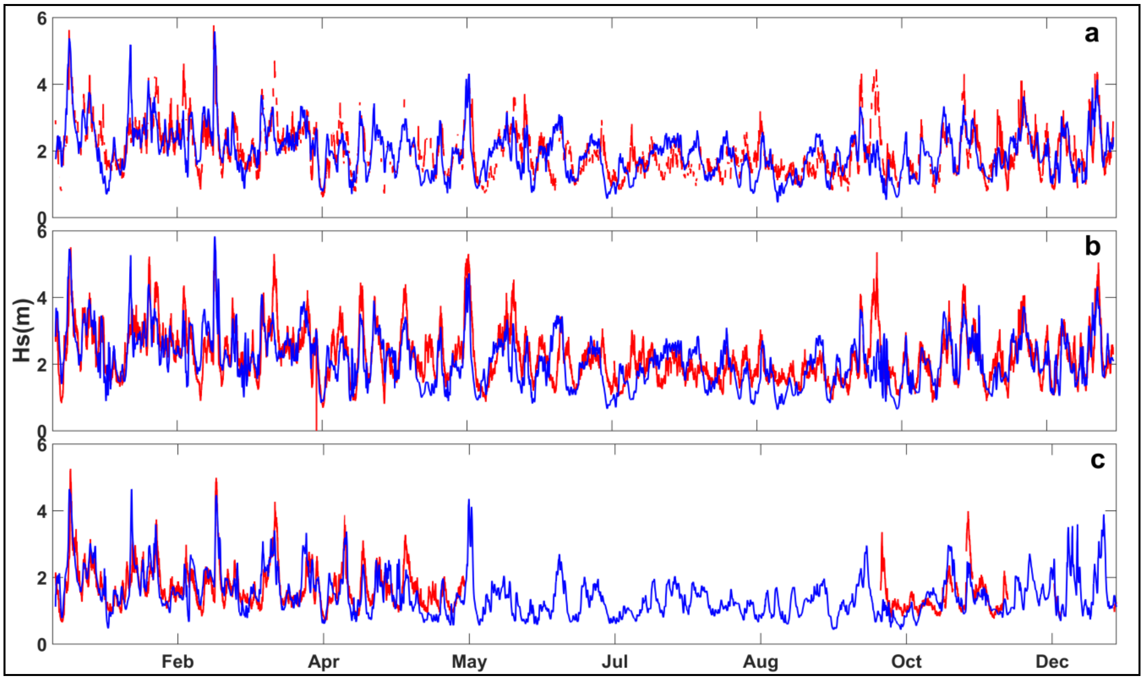

Figure 66. Same as Figure 64, but for station (a) 46054, (b) 46069, and (c) 46086.

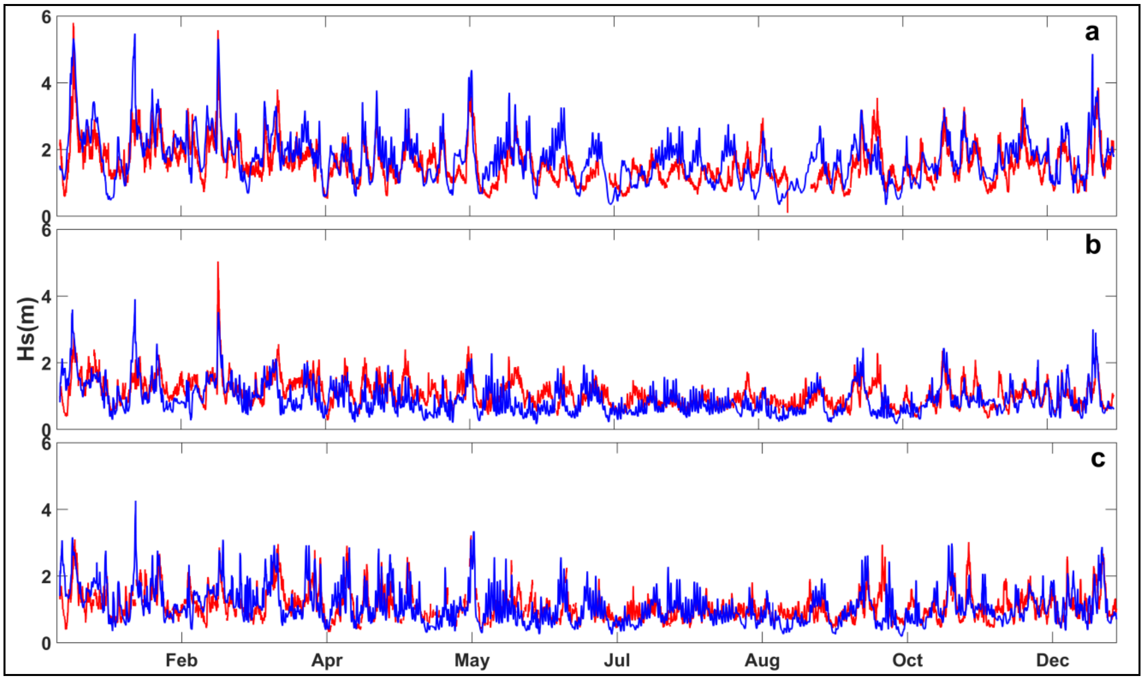

Figure 67. Same as Figure 64, but for station (a) 460215, (b) 46216, and (c) 46217.

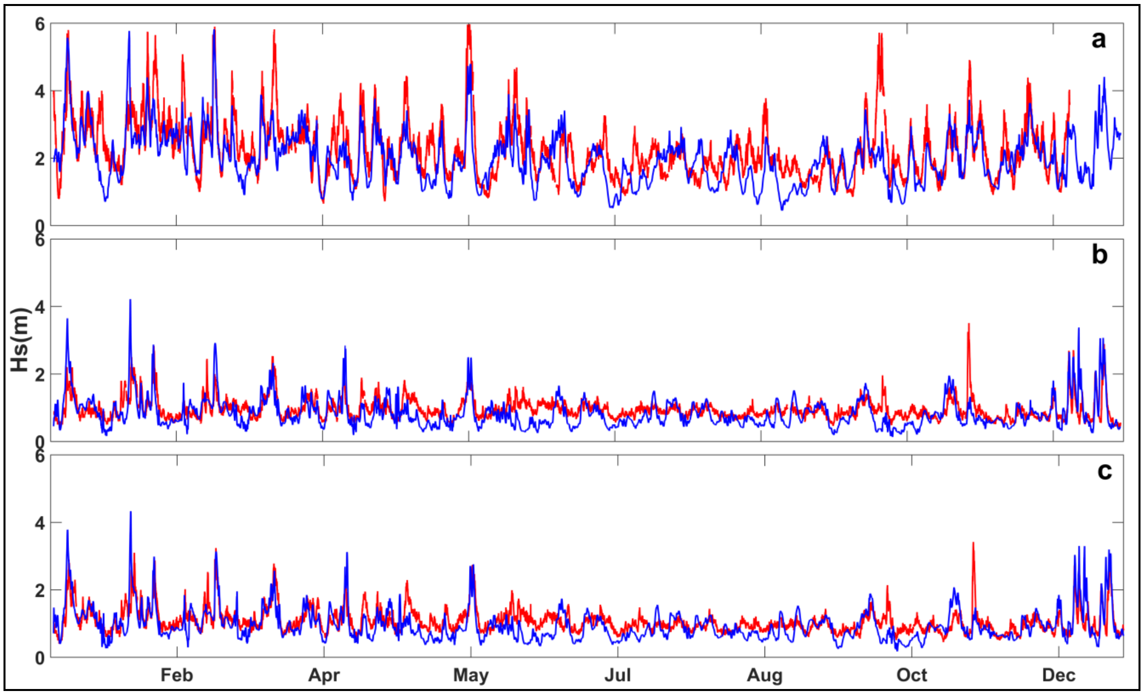

Figure 68. Same as Figure 64, but for station (a) 460218, (b) 46224, and (c) 46225.

Figure 69 shows the SWH correlation and RMSE between observations and SWAN output. The left panel presents the pie chart of the correlation coefficients. It is observed that 11% of the correlations are larger than 0.8, and 36% of the correlations are larger than 0.6. Only 7% are less than 0.2. Moreover, about 70% of the RMSE are less than 0.7 m and only 1.5% are larger than 1 m. This result indicates that the SWAN model simulates the SWH well.

Figure 69a shows the percentage of the correlation coefficients of SWH between observations and simulations at each buoy station based on the hourly SWH data. 11% of the correlations are larger than 0.8, and 36% of the correlations are larger than 0.6. Only 7% are less than 0.2. The RMSE between all observations (14 points) and SWAN output shows that about 70% of the RMSE are less than 0.7 m and only 1.5% are larger than 1 m (Figure 69b). This result indicates that the SWAN model simulates the SWH well.

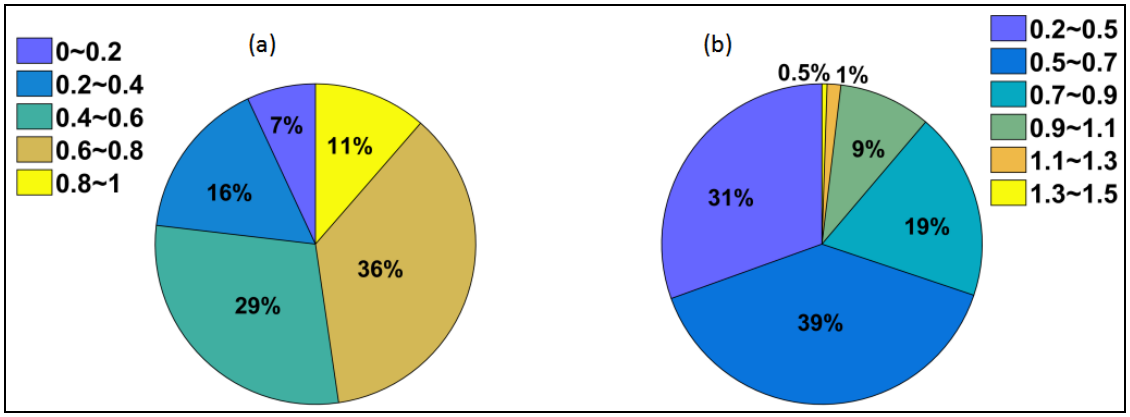

Figure 69. (a) Pie chart of correlation coefficients of SWH between observations and simulations. (b) Pie chart of the SWH RMSE (units: m).

6.3 Validation of mean wave direction

Mean wave diffraction (MWD) indicates the direction from which the waves during the dominant period (DPD) are coming. The units are degrees from true North, increasing clockwise, with North as 0 degrees and East as 90 degrees.

In this study, a random selection of the MWD data from 2009 is analyzed. Figure 70 shows the seasonal MWD from ERA-Interim. It is found that the MWD is southeastward in the open sea, and turns eastward or northeastward as it approaches the coast. Figure 71 shows the seasonal MWD and SWH in the SWAN simulations. The pattern resembles that in observations.

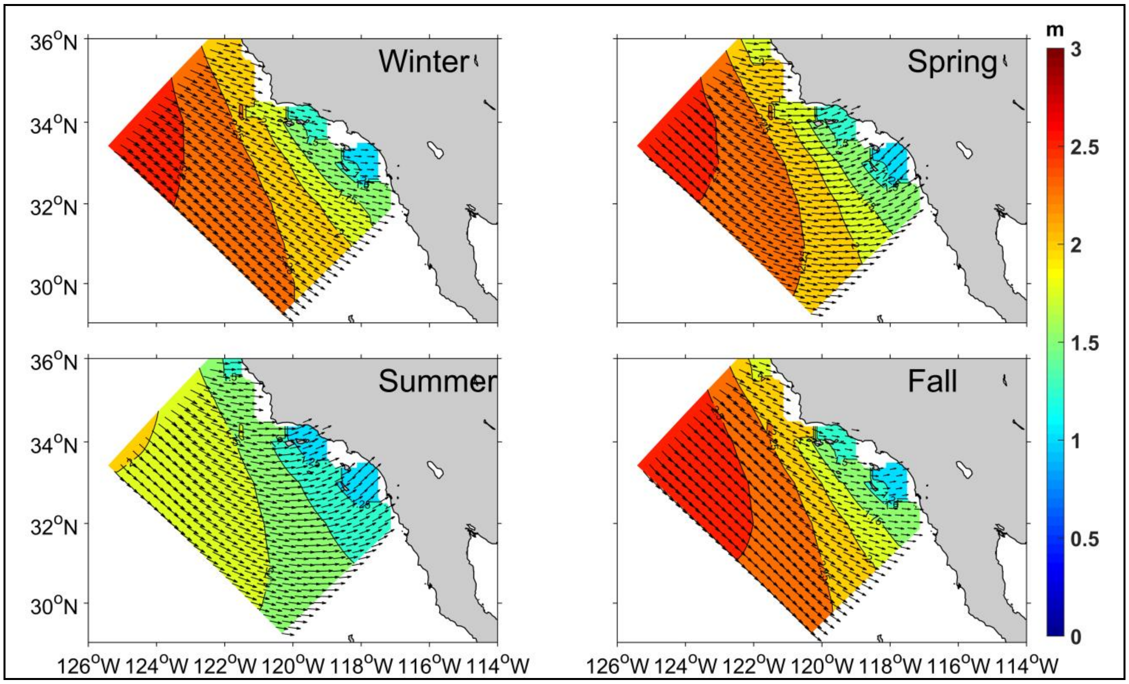

Figure 70. Seasonal SWH (color shadings) and MWD (vectors) from ERA-Interim (units: m) in (a) winter, (b) spring, (c) summer, and (d) fall.

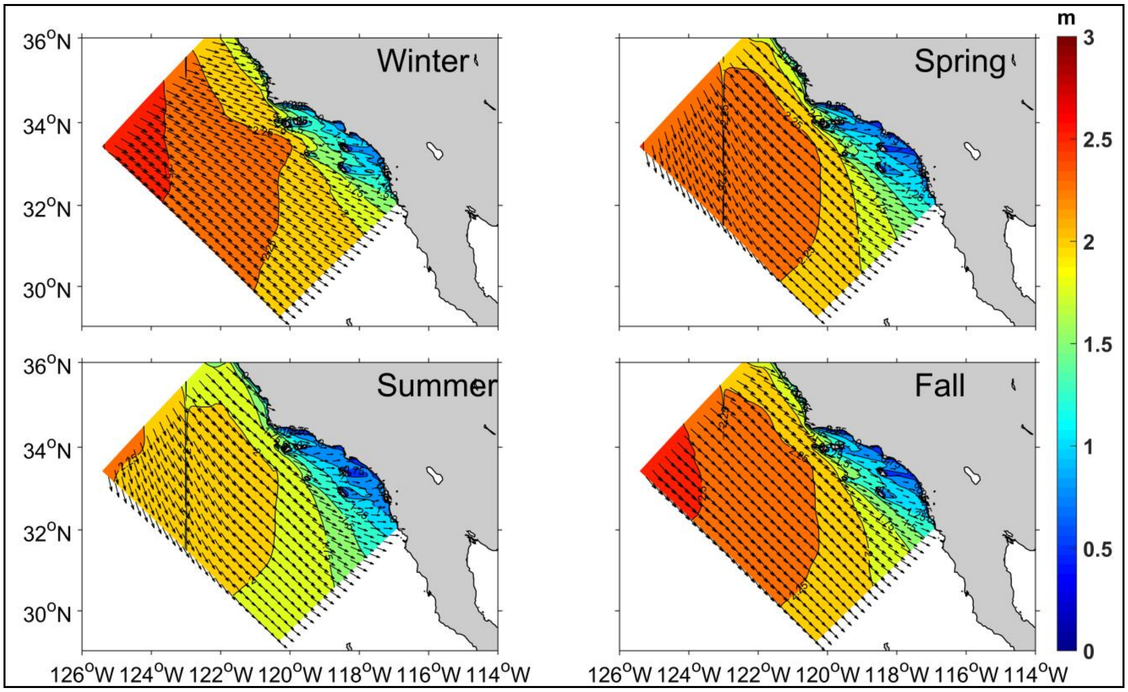

Figure 71. Same as Figure 70, but from SWAN.

Figure 72 shows the rose plot for the SCB MWD. The upper panels present the seasonal MWD at station 46011 in 2012, and the lower panels show the SWAN results at the station locations. It is noted that the wave direction is mostly southeastward. The SWH is larger in winter and spring than in summer and fall. Generally, the SWAN reproduces the MWD and SWH features, and captures the seasonality. Figure 73 through Figure 82 present the rose plots for the MWD at the other buoy stations. Large differences between the observed and SWAN simulated MWD occur at stations 46053, 46216, and 46217.

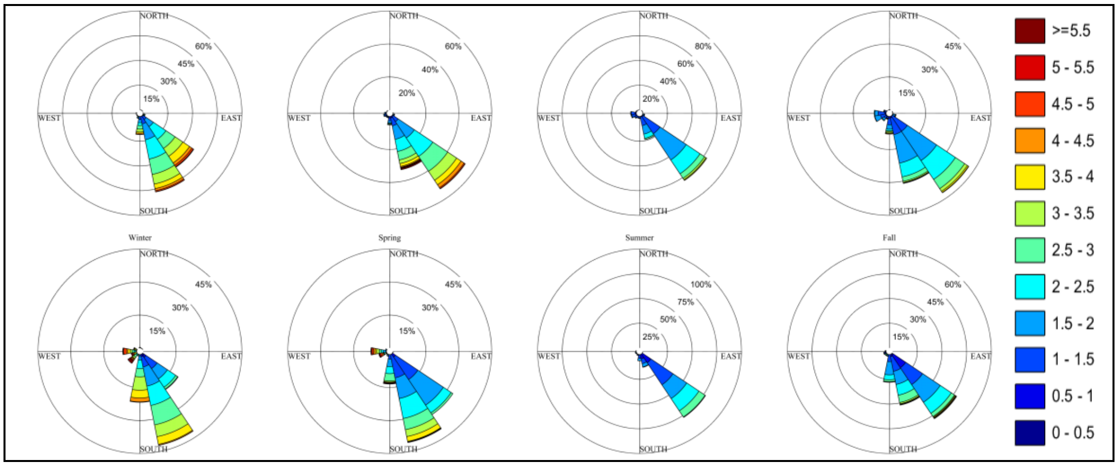

Figure 72. Seasonal MWD roses from observations and SWAN simulations at station 46011 in 2012. The upper panels show in-situ observations and the lower panels represent the SWAN simulations. The SWHs are represented by the different colors shown in the legend (units: m).

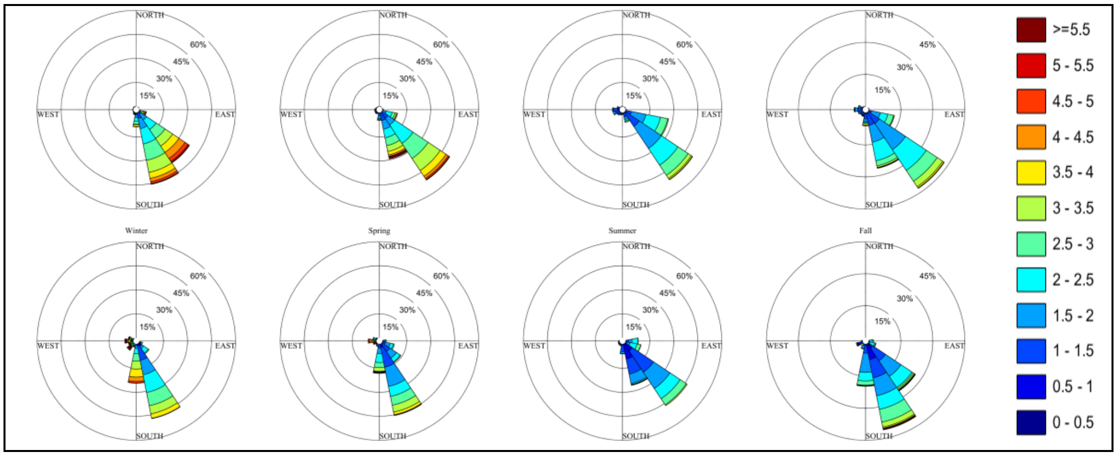

Figure 73. Same as Figure 72, but for station 46028.

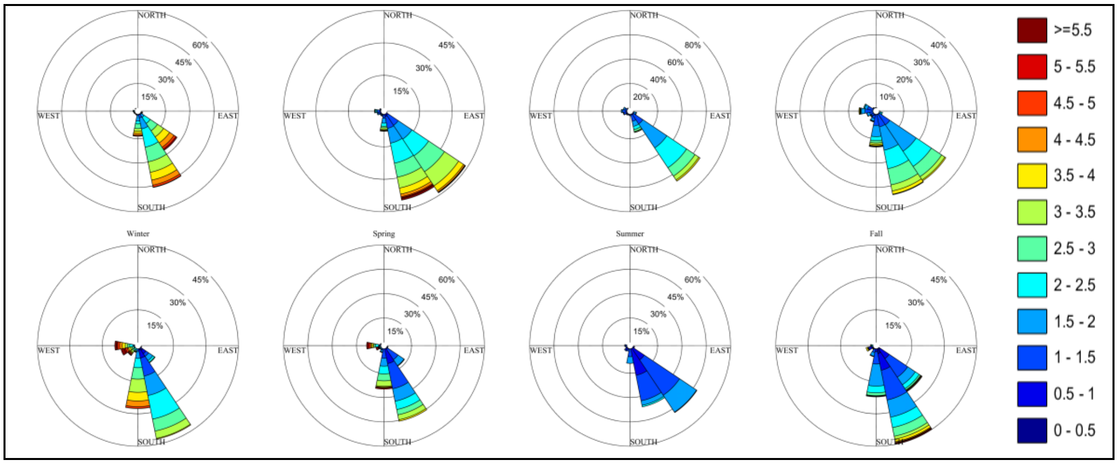

Figure 74. Same as Figure 72, but for station 46042.

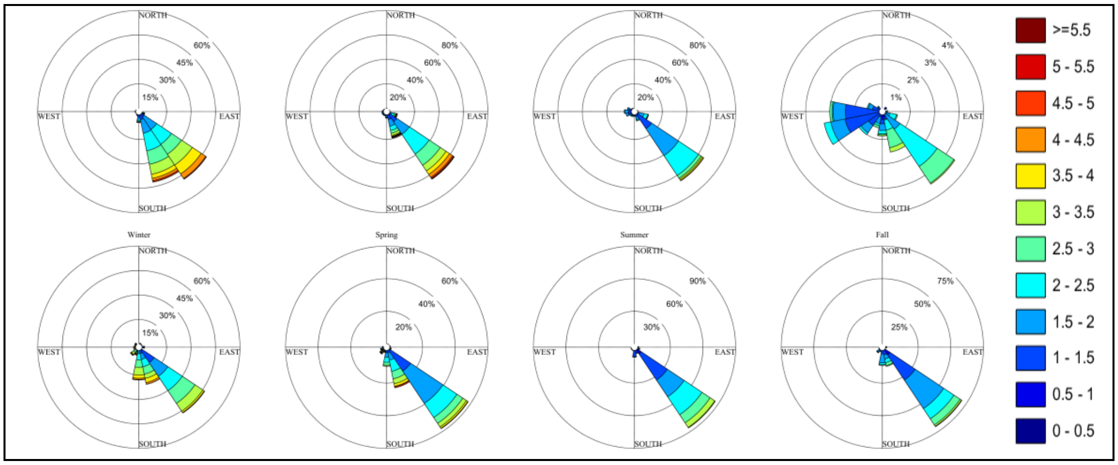

Figure 75. Same as Figure 72, but for station 46047.

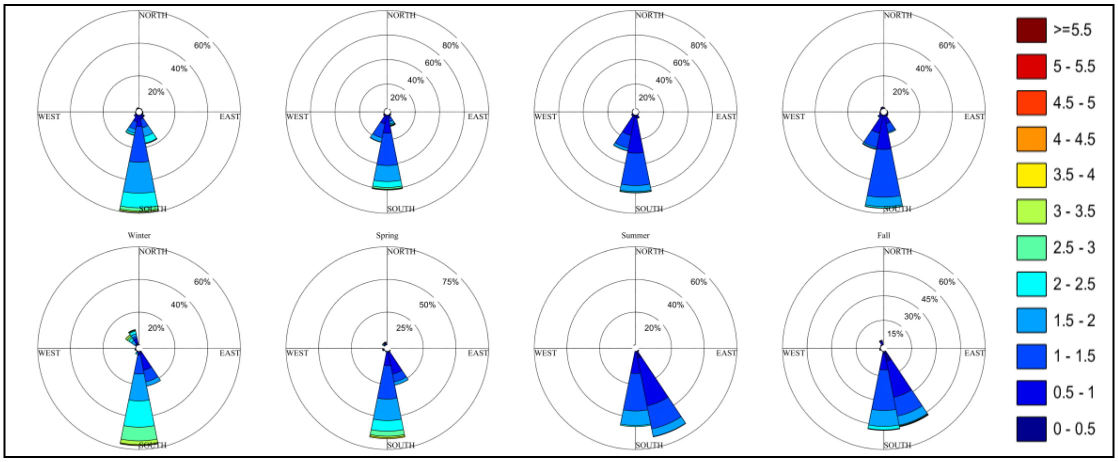

Figure 76. Same as Figure 72, but for station 46053.

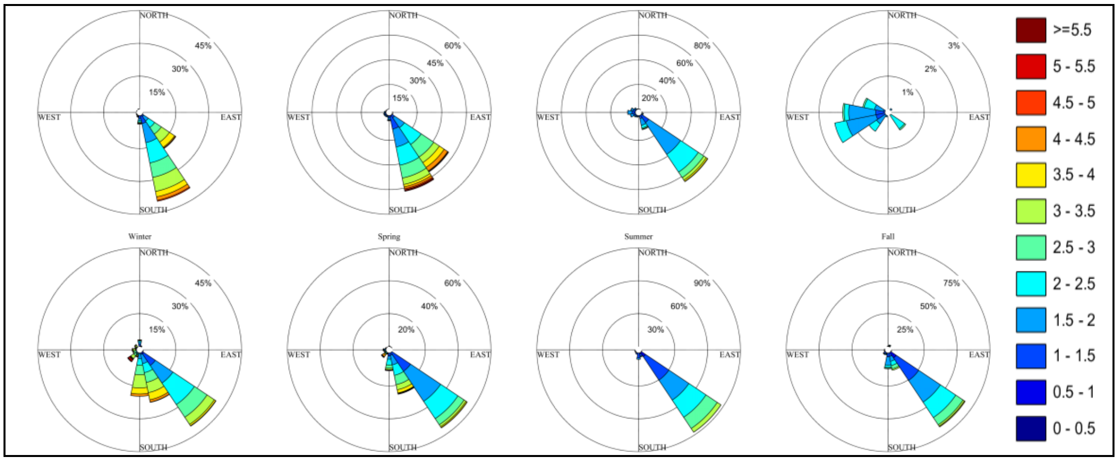

Figure 77. Same as Figure 72, but for station 46069.

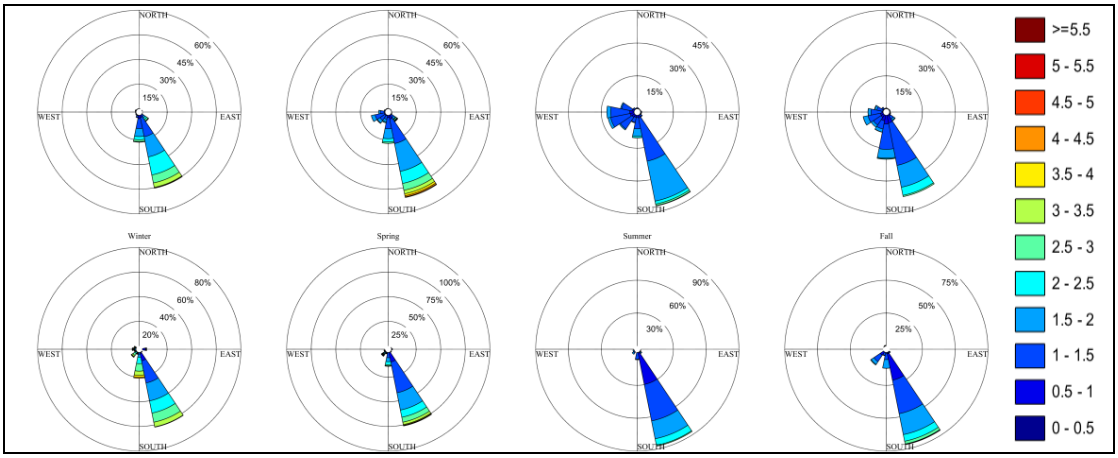

Figure 78. Same as Figure 72, but for station 46086.

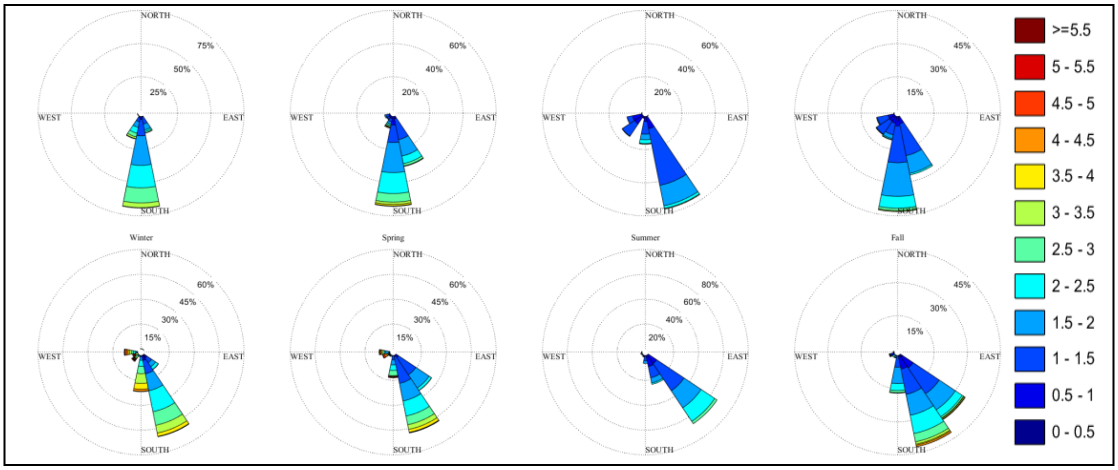

Figure 79. Same as Figure 72, but for station 46215.

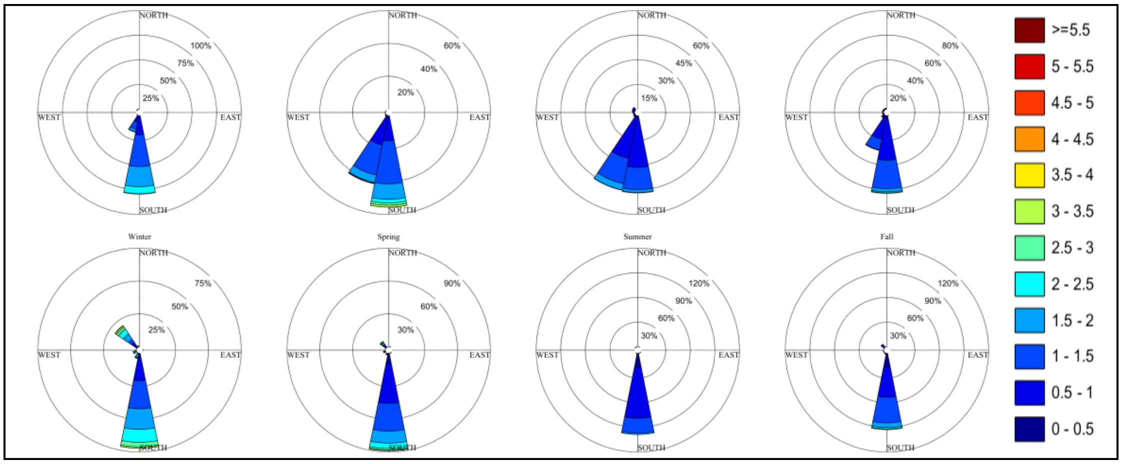

Figure 80. Same as Figure 72, but for station 46216.

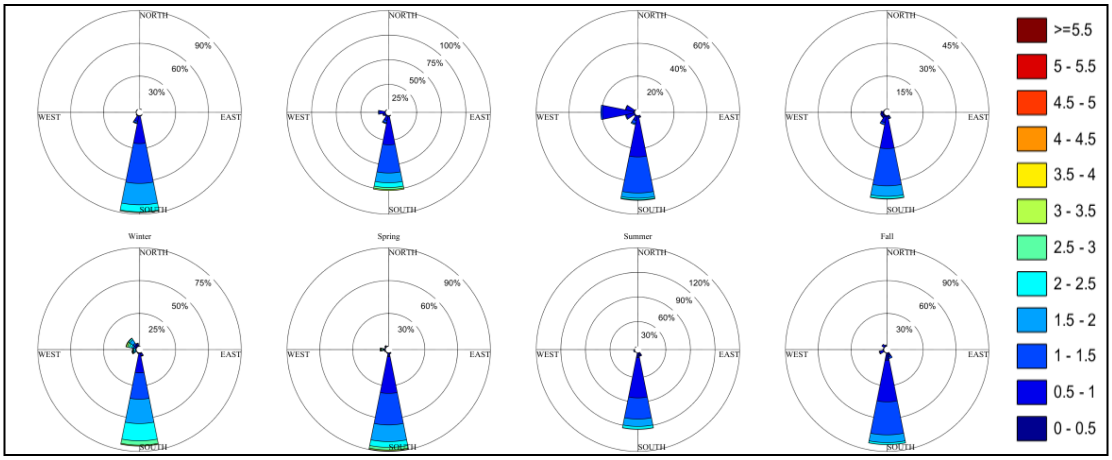

Figure 81. Same as Figure 72, but for station 46217.

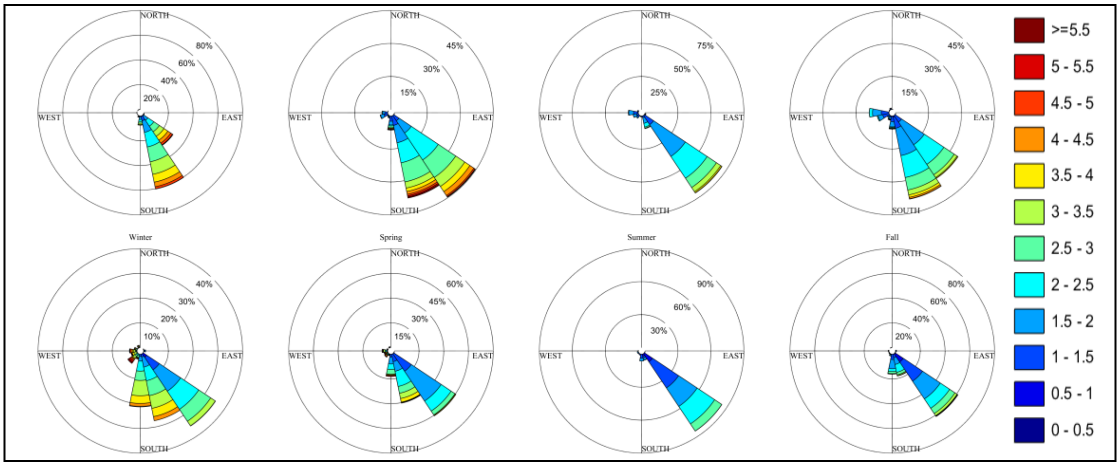

Figure 82. Same as Figure 72, but for station 46218.

7. Summary

The WRF, ROMS, and SWAN models are applied to provide three new hindcasts of 10-m winds, precipitation, cloud cover, water temperature, currents, salinity, tides, and waves for the period of 2004–2013. The model domain extends from the SCB to north of Point Conception including Morro Bay. In this study, the hindcast data are validated against observations.

In comparison with CCMP and buoy (GPCP) observations, we evaluate the WRF simulated U.S. West Coast 10-m winds (precipitation). The WRF simulation generally captures the spatial pattern of the 10-m winds, wind speed, and wind curl in all four seasons. The WRF simulation particularly reproduces the nearshore wind features well. In addition, the precipitation is reproduced reasonably well by the simulation.

The ROMS simulated tides, SSH, sea water temperature, salinity, and currents are evaluated against various observational data, including the satellite remote sensing, moored buoys, HF radar, and ship-borne measurements. Overall, the ROMS well captures the primary characteristics of the tides, SSH, water temperature, salinity, and currents.

The SWAN simulated SWH and MWD are evaluated against ERA-Interim, altimeter, and buoy observations. The SWAN simulation generally captures the spatial pattern of the wave height and wave direction in all four seasons. The simulation also shows the effect of the islands on the wave, demonstrating the ability of SWAN in simulating the reflection and diffraction of waves in the SCB region.

The validations of the three new hindcasts show the capability of the models in simulating 10-m winds, precipitation, cloud cover, water temperature, currents, salinity, tides, and waves for the period of 2004–2013. This indicates that these hindcasts can be used for further analyses such as conducting oil spill risk analysis in southern California.

References

Aarnes, O. J., S. Abdalla, J. R. Bidlot, and Ø. Breivik, 2015: Marine wind and wave height trends at different ERA-Interim forecast ranges. J. Climate, 28(2), 819-837.

Adler, R. F., G. J. Huffman, A. Chang, R. Ferraro, P. Xie, J. Janowiak, B. Rudolf, U. Schneider, S. Curtis, D. Bolvin, A. Gruber, J. Susskind, P. Arkin, and E. Nelkin, 2003: The Version 2 Global Precipitation Climatology Project (GPCP) Monthly Precipitation Analysis (1979-Present). J. Hydrometeor., 4, 1147-1167.

Atlas, R., R. N. Hoffman, S. C. Bloom, J. C. Jusem, and J. Ardizzone, 1996: A multiyear global surface wind velocity data set using SSM/I wind observations. Bull. Amer. Meteor. Soc., 77, 869-882.

Auad, G. C., M. C. Hendershott, and C. D. Winant, 1998: Wind-induced currents and bottom-trapped waves in the Santa Barbara Channel. J. Phys. Oceanogr., 28: 85-102.

Auad, G., D. Roemmich, and J. Gilson, 2011: The California Current System in relation to the Northeast Pacific Ocean circulation. Prog. Oceanogr., 91(4), 576-592.

Battjes, J. A., and J. P. F. M. Janssen, 1978: Energy loss and set-up due to breaking random waves. Asce, 1(16): 569-587.

Bromirski, P. D., A. J. Miller, R. E. Flick, and G. Auad, 2011: Dynamical suppression of sea level rise along the Pacific coast of North America: Indications for imminent acceleration. J. Geophys. Res.: Oceans, 116(C7).

Chou, M.-D., and M. J. Suarez, 1999: A solar radiation parameterization for atmospheric studies. NASA Tech. Rep. 104606, 51 pp. [Available online at http://ntrs.nasa.gov/search.jsp?R519990060930.]

Counillon, F., and L. Bertino, 2009: Ensemble Optimal Interpolation: multivariate properties in the Gulf of Mexico. Tellus Series A-dynamic Meteorology & Oceanography, 61, 296-308.

Cracknell, A. P. 1997: Advanced very high resolution radiometer AVHRR. CRC Press.

Di Lorenzo, E., 2003: Seasonal dynamics of the surface circulation in the Southern California Current System. Deep Sea Research Part II Topical Studies in Oceanography, 50, 2371-2388.

Dong, C. M., E. Y. Idica, and J. C. Mcwilliams, 2009: Circulation and multiple-scale variability in the Southern California Bight. Prog. Oceanogr., 82, 168-190.

Dong, C. M., F. Nencioli, Y. Liu, and J. C. McWilliams, 2011: An automated approach to detect oceanic eddies from satellite remotely sensed sea surface temperature data. Ieee Geosci

Remote S, 8, 1055-1059.

Donlon, C. J., K. S. Casey, I. S. Robinson, C. L. Gentemann, R. W. Reynolds, I. Barton, O. Arino, J. Stark, et al., 2009: The GODAE high-resolution sea surface temperature pilot project, Oceanography, 22, 34-45.

Dudhia, J., 1989: Numerical study of convection observed during the winter monsoon experiment using a mesoscale two-dimensional model. J. Atmos. Sci., 46(20), 3077-3107.

European Centre for Medium-Range Weather Forecasts (ECMWF) website. [cited 2017 June 1]. Available from: http://www.ecmwf.int/

Flather, R. A., 1976: A tidal model of the northwest European continental shelf. Memo. Soc. Roy. Sci. Liege, 6, 10. 141-164.

Hickey, B. M., 1979: The California Current system—hypotheses and facts. Prog. Oceanogr., 8(4), 191-279.

Hill, A. E., B. M. Hickey, F. A. Shillington, P. T. Strub, K. H. Brink, E. D. Barton, and A. C. Thomas (1998), Eastern ocean boundaries coastal segment (E), in The Sea, vol. 11, The Global Coastal Ocean: Regional Studies and Syntheses, edited by A. R. Robinson and K. H. Brink, pp 29-67, John Wiley, New York.

Holthuijsen, L. H., 2007: Waves in oceanic and coastal waters. Cambridge University Press, pp70, Cambridge, New York.

Hong, S. Y., J. O. J. Lim, 2006: The WRF single-moment 6-class microphysics scheme (WSM6). J. Korean Meteorol. Soc., 42(2), 129-151.

Institut français de recherche pour l'exploitation de la mer (IFREMER) website. [cited 2017 June 1]. Available from: ftp://ftp.ifremer.fr/ifremer/cersat/products/gridded/altimeters/waves/

Janssen, P. A. E. M., 1991: Quasi-linear theory of wind-wave generation applied to wave forecasting. J. Phys. Oceanogr., 21, 1631-1642.

Janssen, P. A. E. M., 1989: Wave-induced stress and the drag of air flow over sea waves. J. Phys.Oceanogr. 19, 745-754.

Kain, J. S., and J. M. Fritsch, 1990: A one-dimensional entraining/detraining plume model and its application in convective parameterization. J. Atmos. Sci., 47(23), 2784-2802.

Large, W. G., J. C. McWilliams, and S.C. Doney, 1994. Oceanic vertical mixing: A review and a model with a nonlocal boundary layer parameterization. Rev. Geophys. 32, 363-403.

Large, W. G., 2006. Surface fluxes for practitioners of global ocean data assimilation, in: Chassignet, E.P.,Verron, J. (Eds.), Ocean Weather Forecasting. Springer Netherlands, pp 229-270.

Marchesiello, P., J. C. McWilliams, and A. Shchepetkin, 2003: Equilibrium Structure and Dynamics of the California Current System. J. Phys. Oceanogr., 33, 753-783.

Mlawer, E. J., S. J. Taubman, P. D. Brown, M. J. Iacono, and S. A. Clough, 1997: Radiative transfer for inhomogeneous atmospheres: RRTM, a validated correlated-k model for the longwave. J. Geophys. Res., 102(D14), 16 663-16 682.

Nakanishi, M., and H. Niino, 2006: An improved Mellor-Yamada Level-3 model: Its numerical stability and application to a regional prediction of advection fog. Bound.-Layer Meteor., 119, 397-407, doi:10.1007/s10546-005-9030-8.

National Buoy Data Center (NDBC) website. [cited 2017 June 1]. Available from: http://www.ndbc.noaa.gov

Ohlmann, J. Carter, and S. Mitarai. 2010: Lagrangian assessment of simulated surface current dispersion in the coastal ocean. Geophys. Res. Lett., 37(17), 204-216.

Oke, P. R., A. Schiller, D. A. Griffin, and G. B. Brassington, 2005: Ensemble data assimilation for an eddy-resolving ocean model of the Australian region. Q. J. Roy. Meteor. Soc., 131, 3301-3311.

Oke, P. R., G. B. Brassington, D. A. Griffin, and A. Schiller, 2010: Ocean Data Assimilation: a case for ensemble optimal interpolation. Australian Meteorological & Oceanographic Journal, 59, 67-76.

Orlanski, I., 1976: A simple boundary condition for unbounded hyperbolic flows. J. Comput. Phys., 21(3), 251-269.

Pawlowicz, R., B. Beardsley, and S. Lentz, 2002: Classical tidal harmonic analysis including error estimates in MATLAB using T_TIDE. Computers & Geosciences, 28(8), 929-937.

Renault, L., A. Hall, and J. C. McWilliams, 2016: Orographic shaping of U.S. West Coast wind profiles during the upwelling season. Climate Dyn., 46, 273-289.

Shchepetkin, A. F., and J. C. McWilliams, 2005: The Regional Oceanic Modeling System (ROMS): a split-explicit, free-surface, topography-following-coordinate oceanic model. Ocean Modelling, 9, 347-404. doi:10.1016/j.ocemod.2004.08.002.

Skamarock, W, J. Klemp, J. Dudhia, D. Gill, and D. Barker, 2008: A description of the Advanced Research WRF version 3. Tech. rep., NCAR/TN-4751STR.

Springel, V., J. Wang, M. Vogelsberger, et al., 2008: The Aquarius Project: the subhaloes of galactic haloes. Monthly Notices of the Royal Astronomical Society, 391(4), 1685-1711.

Strub, P. T., and C. James, 2000: Altimeter-derived variability of surface velocities in the

California Current System: 2. Seasonal circulation and eddy statistics. Deep-sea Res. PT II, 47, 831-870.

Zijlema, M., G. P. V. Vledder, and L. H. Holthuijsen, 2012: Bottom friction and wind drag for wave models. Coast Eng., 65(7), 19-26.

Department of the Interior (DOI)

The Department of the Interior protects and manages the Nation's natural resources and cultural heritage; provides scientific and other information about those resources; and honors the Nation’s trust responsibilities or special commitments to American Indians, Alaska Natives, and affiliated island communities.

Bureau of Ocean Energy Management (BOEM)

The mission of the Bureau of Ocean Energy Management is to manage development of U.S. Outer Continental Shelf energy and mineral resources in an environmentally and economically responsible way.

BOEM Environmental Studies Program

The mission of the Environmental Studies Program is to provide the information needed to predict, assess, and manage impacts from offshore energy and marine mineral exploration, development, and production activities on human, marine, and coastal environments. The proposal, selection, research, review, collaboration, production, and dissemination of each of BOEM’s Environmental Studies follows the DOI Code of Scientific and Scholarly Conduct, in support of a culture of scientific and professional integrity, as set out in the DOI Departmental Manual (305 DM 3).